Thesis submitted in partial fulfillment of the requirements

for the degree of

Philosophiæ Doctor in Space Science

Evolution of chromospheric structures observed with USET and implications for the Sun seen as a star

VANDEN BROECK
Grégory

Supervisors :

Prof. RAUW Grégor (Université de Liège)

Dr. BECHET Sabrina (Observatoire Royal de Belgique)

Thesis jury members :

Prof. DUPRET Marc-Antoine (Université de Liège, President)

Prof. NAZE Yaël (Université de Liège, Secretary)

Dr. CLETTE Frédéric (Université Libre de Bruxelles)

Prof. ERMOLLI Ilaria (INAF Osservatorio Astronomico di Roma)

Dr. CHATZISTERGOS Theodosios (Max Planck Institute for Solar System Research)

For travelers, the stars are their guides. For some sleepers, they are their shelter. For artists, they are their inspiration. For chefs, they are their rewards. All mothers hope their children are born under a lucky star, and we all want to believe in ours. When I was a child, my eyes were full of stars, and when night fell, I imagined I could count them, touch them, or catch them. As I grew up and learned that astronomy and astrophysics enriched this imagination, I realized which star I needed to follow.

Grégory Vanden Broeck

Among the stars that light up the sky, one shines brighter for me.

—— In memory of my beloved grandmother ——

Pour les voyageurs, les étoiles sont leurs guides. Pour certains dormeurs, elles sont leur toit. Pour les artistes, elles sont leur objectif. Pour les restaurateurs, elles sont leurs récompenses. Toutes les mamans voudraient que leurs enfants naissent sous une bonne étoile et nous voulons tous croire en la nôtre. Quand j'étais petit, j'avais des étoiles plein les yeux et lorsque la nuit déployait les siennes, j'imaginais pouvoir les compter, les toucher ou les attraper. Après avoir grandi et appris que l'astronomie et l'astrophysique étaient venues enrichir cet imaginaire, j'ai compris quelle étoile je devais suivre.

Grégory Vanden Broeck

Parmi les étoiles qui illuminent le ciel, une brille plus intensément pour moi.

—— En mémoire de ma grand-mère bien-aimée ——

Acknowledgements

Astronomy and astrophysics have fascinated me since I was very young. Studying this field and making it my profession is something I am deeply passionate about, and it represents the fulfillment of a long-held dream. I will be infinitely grateful to all the people who contributed to making this dream a reality.

I would like to begin by expressing my deep gratitude to my supervisors, Dr. Sabrina Bechet and Prof. Grégor Rauw. The invaluable help and constant dedication of Dr. Bechet throughout my project have greatly contributed to the success of my work. I am sincerely grateful to Prof. Rauw for the quality of his supervision and his constant availability. Whenever I faced challenges, Prof. Rauw was always just an email away.

I wish to extend my thanks to Dr. Frédéric Clette for sharing his vast knowledge, for his invaluable advice, and his inspiring idea for the project.

I owe a great deal of appreciation to Dr. Shreya Bhattacharya for her help and advice during our exchanges, as well as for our enjoyable discussions during lunches.

And to all my other colleagues from the Solar Physics Department at the Royal Observatory of Belgium, I sincerely thank them for making my work environment a friendly and joyful place.

Last but not least, I cannot end without warmly thanking my family and loved ones, especially my wonderful parents, my amazing brother, and my lovely partner. I am immensely grateful to them for believing in me throughout all these years of study, for their unwavering support and motivation in both successes and failures. A large part of my success has been made possible thanks to them.

THANK YOU !

Remerciements

L'astronomie et l'astrophysique me fascinent depuis mon plus jeune âge. Étudier ce domaine et en faire ma profession est quelque chose qui me passionne profondément et représente l'accomplissement d'un rêve de longue date. Je serai infiniment reconnaissant envers toutes les personnes qui ont contribué à rendre ce rêve possible.

Je voudrais commencer par exprimer ma profonde gratitude à mes promoteurs, Dr. Sabrina Bechet et Prof. Grégor Rauw. L'aide précieuse et le dévouement constant de Dr. Bechet tout au long de mon projet ont grandement contribué au succès de mon travail. Je suis sincèrement reconnaissant envers Prof. Rauw pour la qualité de sa supervision et sa disponibilité constante. À chaque difficulté rencontrée, Prof. Rauw était toujours à un email près.

Je tiens également à adresser mes remerciements à Dr. Frédéric Clette pour m'avoir partagé son vaste savoir, pour ses conseils précieux et son idée inspirante pour le projet.

Je dois une grande reconnaissance à Dr. Shreya Bhattacharya pour son aide et ses conseils lors de nos échanges, ainsi que pour nos discussions agréables pendant les dîners.

Et à tous mes autres collègues du département de Physique Solaire à l'Observatoire Royal de Belgique, je les remercie sincèrement d'avoir rendu mon environnement de travail amical et joyeux.

Enfin, je ne saurais conclure sans remercier chaleureusement ma famille et mes proches, en particulier mes merveilleux parents, mon incroyable frère et ma charmante partenaire. Je leur suis immensément reconnaissant d'avoir cru en moi tout au long de ces années d'études, pour leur soutien indéfectible et leur motivation tant dans les succès que dans les échecs. Une grande partie de mon succès a été rendue possible grâce à eux.

MERCI !

Contents

List of Figures

Abbreviations

AN	Active Network
$\mathbf{A}_P$	Area fraction of plages
$\mathbf{A}_{PEN}$	Area fraction of plages and enhanced network
CLV	Center-to-Limb Variation
CMEs	Coronal Mass Ejections
CN	Chromospheric Network
EN	Enhanced Network
EUV	Extreme Ultraviolet
FWHM	Full Width at Half Maximum
HMI	Helioseismic Magnetic Imager
HR	Hertzsprung-Russell
ISN	International Sunspot Number
L1	Level-1
$M_\odot$	Solar mass
MS	Main-sequence
MWO	Mount Wilson Observatory
NOAA	National Oceanic and Atmospheric Administration
P	Plages
PEN	Plages and Enhanced Network
PSPT	Precision Solar Photometric Telescope
QN	Quiet Network
QS	Quiet Sun
ROB	Royal Observatory of Belgium
SDO	Solar Dynamics Observatory
SIDC	Solar Influences Data Analysis Center
SILSO	Sunspot Index and Long-Term Solar Observations
SN	Sunspot Number
SWPC	Space Weather Prediction Center
TIGRE	Telescopio Internacional de Guanajuato Robotico Espectroscopico
USET	Uccle Solar Equatorial Table
WL	White Light

Abstract

The physical mechanisms governing the magnetic activity of stars, as well as the variations in their activity cycles, are crucial research topics with direct implications on the understanding of stellar evolution and interactions with their surroundings. Although these mechanisms remain largely unknown, they are currently at the focus of intensive research in astrophysics. Due to their considerable distance, most stars appear only as unresolved points in the sky, even with the most advanced telescopes. Fortunately, our star, the Sun, is at a much closer distance, allowing us to study more closely the phenomena of magnetic activity and the spatial distribution of active regions on its surface. Other stars differ from our Sun depending on their size, age, temperature, luminosity, mass, gravity, or chemical composition. However, the Sun is probably a good example of a low-mass star. Studying the Sun allows us to learn more about this star that sustains our existence but also to explore similar mechanisms acting in other stars.

The Sun is a sphere of plasma with an atmosphere. This atmosphere is divided into several layers, and magnetic phenomena are visible in each of them, but in different ways. For our study, we have analysed the magnetic structures present in the intermediate part of the solar atmosphere, namely the chromosphere. At the Royal Observatory of Belgium, located in Uccle, Brussels, a telescope is specifically dedicated to observing this layer of the atmosphere and is operational since July 2012. Images are acquired every day by scientists, when the weather permits. A filter is placed on the telescope to capture the sunlight in a specific part of the electromagnetic spectrum: around the Ca II K line, located at a wavelength of 3933.67 Å.

The most prominent magnetic structures in images of the chromosphere in the Ca II K line are the ”plages”, which are bright and extended regions. These structures correspond to areas of strong magnetic field concentrations and contain hotter material compared to the rest of the chromosphere. The plages are the main contributors to the chromospheric emission and, in this case, the primary modulators of the chromospheric activity. The main goal of our work is to study the long-term evolution of these magnetic structures, i.e. over several years. To achieve this, we developed an algorithm to segment the brightest structures in the chromosphere. We extracted their area and obtained a time series of area fraction characterizing the chromospheric activity of the Sun. This time series is the basis of all the results of our study.

First of all, we compared this time series with the S-index, the most commonly used index in astrophysics for analysing the chromospheric activity of stars. We used data from TIGRE, a

telescope based in Guanajuato, Mexico, which observes spectra of the Sun and other stars. Its particularity is that it observes the Sun during the night, thanks to the light reflected by the Moon. Our study showed that both indices are strongly linearly correlated. Then, to map the distribution of magnetic structures at the solar surface, we took advantage of the solar rotation to reconstruct synoptic maps of the active regions over a range of 360° in solar longitude. These maps allowed us to reproduce synthetic images of the Sun seen under different angles of view. Since stars are randomly oriented relative to the Earth, the inclination of the rotation axis of the star is an important parameter to consider when analysing the observable magnetic activity. Thus, based on the reproduced synthetic images of the Sun seen under different viewing angles, we estimated the impact of the inclination on the chromospheric activity of the Sun, using the area fraction of the plages as a parameter. Another important part of our work concerned the detection of periodic modulations based on the area fraction time series, namely the solar rotation of ~ 27.27 days, as well as the activity cycle of ~ 11 years. For this, we used a Fourier power spectrum method, which is a data analysis technique used to identify dominant frequencies in a time series. We performed this analysis on the initial area fraction time series (based on the raw solar images) as well as on the area fraction time series of the synthetic images for different viewing angles. With the first time series, i.e. solar images in the equatorial view, we have detected the modulation due to the solar rotation and shown that this detection is due to an asymmetry in the longitudinal distribution of active regions. Using the time series of synthetic images, i.e. solar views under different inclinations, our study revealed a significant impact of the inclination angle on the detection of rotational modulation, while the solar cycle modulation remains detectable even with a near Pole-on view. However, the sampling of observations plays a crucial role, as sparser samplings can lead to the disappearance of periodic modulation detection.

Résumé

Les mécanismes physiques qui régissent l'activité magnétique des étoiles ainsi que les variations de leurs cycles d'activité sont des sujets d'étude cruciaux pour comprendre l'évolution de ces étoiles et les interactions avec leur environnement. Bien que ces mécanismes restent encore en grande partie méconnus, ils font actuellement l'objet de recherches intensives dans le domaine de l'astrophysique. En raison de leur distance considérable, la majorité des étoiles apparaissent comme des sources de lumière ponctuelles, même avec les télescopes les plus performants. En revanche, notre étoile, le Soleil, est à une distance bien plus proche et nous permet d'étudier de plus près les phénomènes d'activité magnétique ainsi que la répartition spatiale des régions actives sur sa surface. Les autres étoiles diffèrent du Soleil en raison de leur taille, de leur âge, de leur température, de leur luminosité, de leur masse, de leur gravité, ou encore de leur composition chimique. Toutefois, le Soleil est probablement un bon exemple d'étoile de faible masse. Etudier le Soleil permet d'en apprendre davantage sur cette étoile qui nous permet de vivre mais également d'explorer les mécanismes similaires présents dans d'autres étoiles.

Le Soleil est une sphère de plasma dotée d'une atmosphère. Celle-ci est divisée en plusieurs couches et les phénomènes magnétiques sont visibles dans chacune d'entre elles mais sous de multiples aspects. Pour notre étude, nous avons analysé les structures magnétiques présentes dans la partie intermédiaire de l'atmosphère solaire, à savoir la chromosphère. À l'Observatoire Royal de Belgique, situé à Uccle, Bruxelles, un télescope est spécialement dédié à l'observation de cette couche de l'atmosphère et est en activité depuis juillet 2012. Les images sont acquises tous les jours par des scientifiques, lorsque les conditions météorologiques le permettent. Un filtre est placé sur le télescope permettant de capturer la lumière du Soleil dans une partie spécifique du spectre électromagnétique: autour de la raie du Ca II K, localisée à une longueur d'onde de 3933.67 Å.

Les structures magnétiques les plus flagrantes sur les images de la chromosphère dans la raie du Ca II K sont les "plages". Il s'agit de régions brillantes et étendues. Ces structures correspondent à des zones de fortes concentrations de champ magnétique et des zones plus chaudes que le reste de la chromosphère. Les plages sont les principaux contributeurs de l'émission chromosphérique, et en l'occurence les principaux modulateurs de l'activité chromosphérique. L'objectif principal de notre travail est d'étudier l'évolution sur le long terme de ces structures magnétiques, c'est-à-dire sur plusieurs années. Pour cela, nous avons élaboré un algorithme permettant de segmenter les structures les plus brillantes de la chromosphère. Nous en avons extrait leur aire et

obtenu une série temporelle de fraction d'aire caractérisant l'activité chromosphérique du Soleil. Cette série temporelle est à la base de tous les résultats de notre étude.

Dans un premier temps, nous avons comparé cette série temporelle avec le S-index, l'indice le plus utilisé en astrophysique pour l'analyse de l'activité chromosphérique des étoiles. Nous avons utilisé les données de TIGRE, un télescope basé à Guanajuato au Mexique, qui observe des spectres des étoiles ainsi que du Soleil. Sa particularité est qu'il observe le Soleil durant la nuit, grâce à la lumière réfléchie par la Lune. Notre étude a montré que les deux indices sont fortement corrélés de manière linéaire. Ensuite, afin de cartographier les structures magnétiques à la surface du Soleil, nous avons utilisé la rotation solaire afin de construire des cartes synoptiques des régions actives sur un intervalle de longitudes solaires de 360°. Ces cartes nous ont permis de reproduire des images synthétiques du Soleil vu sous différents angles de vue. Etant donné que les étoiles sont orientées de manière aléatoire par rapport à la Terre, l'inclinaison de l'axe de rotation de l'étoile est un paramètre important à prendre en considération lorsque nous analysons l'activité magnétique observée. Dès lors, sur base des images synthétiques du Soleil reproduites sous différents angles de vue, nous avons pu estimer l'impact de l'inclinaison sur l'activité chromosphérique observable du Soleil, en employant la fraction d'aire des plages comme paramètre. Une autre partie importante de notre travail concernait la détection des modulations périodiques sur base des séries temporelles de fraction d'aire, à savoir la rotation solaire de ~ 27.27 jours, ainsi que le cycle d'activité de ~ 11 ans. Pour cela, nous avons utilisé une méthode du spectre de puissance de Fourier, qui est une technique d'analyse de données pour identifier les fréquences dominantes dans une série temporelle. Nous avons effectué cette analyse sur la série temporelle de fraction d'aire initiale (c'est-à-dire sur base des images solaires brutes) ainsi que sur les séries temporelles de fraction d'aire des images synthétiques sous différents angles de vue. Avec la première série temporelle, c'est-à-dire les images solaires en vue équatoriale, nous avons détecté la modulation due à la rotation solaire et montré que cette détection est due à une asymétrie dans la distribution longitudinale des régions actives. En utilisant les séries temporelles d'images synthétiques, c'est-à-dire des vues solaires sous différentes inclinaisons, notre étude a révélé un impact significatif de l'angle d'inclinaison sur la détection de la modulation rotationnelle, tandis que la modulation du cycle solaire reste détectable même avec une vue proche des Pôles. Cependant, l'échantillonnage des observations joue un rôle crucial, car un échantillonnage plus fragmenté peut conduire à la disparition de la détection de la modulation périodique.

Chapter 1

Introduction

Have you ever found yourself standing in the middle of the night, looking up at the sky and wondering how many stars fill the Universe? Across history, young and old were fascinated by this question, sparking curiosity about the scale of the Universe. Scientists tried to answer it, but it's not as simple as it seems. Counting them one by one, even with the most advanced satellite, is an impossible task. Therefore, scientists must make a rough estimate. In the Universe, stars are grouped into vast cosmic structures known as galaxies. If we can estimate the number of stars in one galaxy and the number of galaxies in the Universe, a simple multiplication can give an estimate of the number of stars in the Universe. Everyone knows at least one star: the Sun, our star. The Sun belongs to a galaxy, called the Milky Way. From observations of our own Galaxy, astronomers have estimated the total number of stars to be about 10^{11} in the Milky Way alone (number from NASA[1]). The number of galaxies in the Universe is even more approximate. Based on observations with the Hubble Space Telescope, astronomers found that the Universe contains about 10^{12} galaxies (number from NASA[2]). Therefore, with a simple calculation, you get the astronomical number of $\sim 10^{23}$ stars in the Universe. While the precise number remains elusive, this approach highlights the immensity and richness of the Universe.

Among all the stars that populate our Universe, only one is situated at a distance from Earth that has made our existence on Earth possible. It is our star, the Sun. Indeed, this distance, about 150 millions km, is ideal for allowing life on Earth to develop and thrive. Moreover, thanks to this "short" distance, our precious star is the one and only star revealing an abundance of details that are inaccessible for all other stars. In fact, because of their huge distance from Earth, all other stars appear as small bright points in the sky, even with the best modern telescopes. Stellar observations consist in capturing the total radiation emitted by all parts of the surface of the star, thus mixing information about the different parts of this surface. Therefore, owing to its close distance from us, everything we can learn and understand from the Sun can be used as a Rosetta Stone to decipher

[1] https://imagine.gsfc.nasa.gov/science/objects/milkyway1.html

[2] https://science.nasa.gov/missions/hubble/hubble-reveals-observable-universe-contains-10-times-more-galaxies-than-previously-thought/

the similar mechanisms acting in other stars.

1.1 The Sun and its activity

In this section, we start with a general description of the internal structure of the Sun, its atmosphere and its magnetic activity. For a more detailed description, we refer to Clette (2022).

1.1.1 General description of the Sun

1.1.1.1 Solar interior

The energy of the Sun is generated by nuclear reactions taking place in the solar core. This energy is transported by two main mechanisms: radiation and convection, and it passes through 3 different layers before reaching the surface. The core, the radiative zone, and the convective zone differ by their temperatures, densities, thicknesses and pressures (see Figure 1.1).

The Sun's core, which extends over the innermost 25% of the solar radius, generates energy through thermonuclear reactions, which result in extreme temperatures up to 15.7×10^6 K. At these extreme temperatures and densities, the so-called proton-proton chain nuclear reaction transforms four hydrogen nuclei into one helium nucleus. Since the mass of four hydrogen atoms exceeds the mass of one helium atom, the excess mass is converted into energy. In the core this energy takes mostly the form of gamma-ray photons. However, as these photons move outwards, they shift to lower energies and finally leave the surface of the Sun mostly as optical photons. This nuclear reaction also releases other particles like positrons and neutrinos. Neutrinos have barely no interaction with solar matter and travel at the speed of light to escape directly from the core and reach the surface in less than 2 seconds, while photons undergo many interactions with matter and take therefore a much longer time to reach the surface.

Once emitted, the photons reach the radiative zone, which extends between 25% and 70% of the solar radius, with a temperature decreasing outward from 7×10^6 to 2×10^6 K. In the core and radiative zone, the density and temperature are such that energy transfer occurs through direct interaction between particles and photons. Photons are absorbed and re-emitted randomly, requiring up to 170 000 years for energy to reach the top of the radiative zone (Mitalas & Sills 1992). Therefore, the energy generated in the core is transported by the photons through this radiative zone. Before reaching the surface of the Sun, photons spend most of their time in the random walk through the radiative zone.

The tachocline is a interface thin layer of less than 5% of the solar radius (Charbonneau et al. 1999; Elliott & Gough 1999; Basu & Antia 2001), located between the radiative zone and the convective zone. Results obtained over the last decades lead us to think that the Sun's magnetic field is generated by a magnetic dynamo in this layer because of a transition of the internal rotation profile of the Sun (Eff-Darwich et al. 2002; Guerrero et al. 2016; Strugarek et al. 2023). The

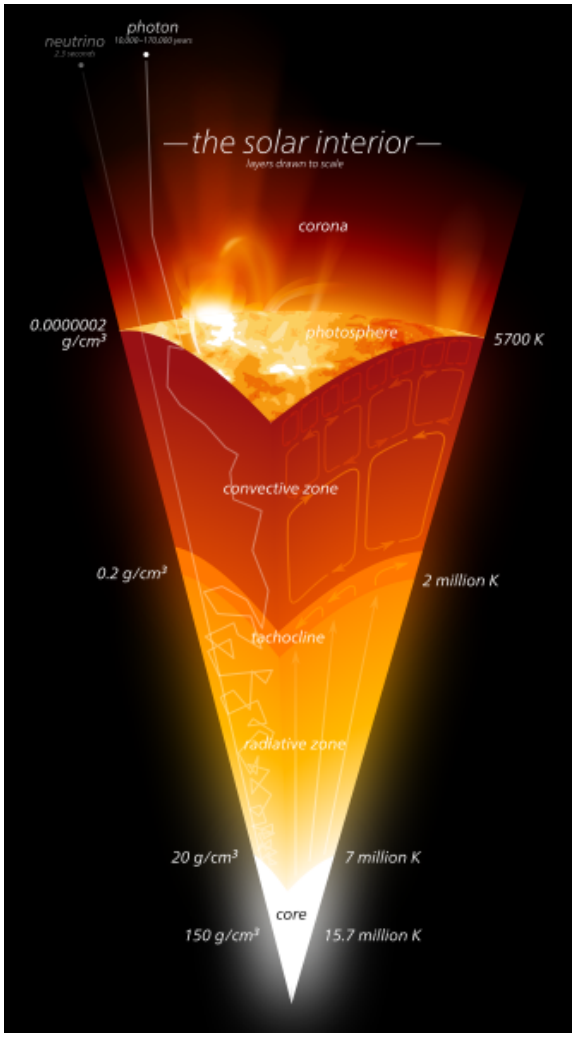

Fig. 1.1. Representation of the structures of the solar interior. The core: innermost 25% where nuclear reactions happen due to the extreme temperatures. The radiative zone: biggest part of the Sun where energy is transported by the absorption and random re-emission of photons. The tachocline: thin layer connecting the radiative zone and the convective zone. The convective zone: outermost layer of the Sun where energy is transported by turbulent plasma motions. Source : Wikimedia - The solar interior[3].

transition from a uniform rotation (in the radiative zone) to a differential rotation (in the convective zone) happens in this interface layer. Variations in fluid flow velocities within the layer (known as shear flows) can stretch magnetic field lines, thereby enhancing their strength. Such a strong large-scale shear transforms efficiently poloidal fields into toroidal fields. The tachocline plays a key role in solar and stellar dynamos models (Guerrero et al. 2016).

Before reaching the surface, the photons have to go through the convective zone, the outermost layer of the Sun's interior with a temperature decreasing from 2×10^6 K to $\sim$ 6 000 K at the

[3] https://commons.wikimedia.org/wiki/File:The_solar_interior.svg

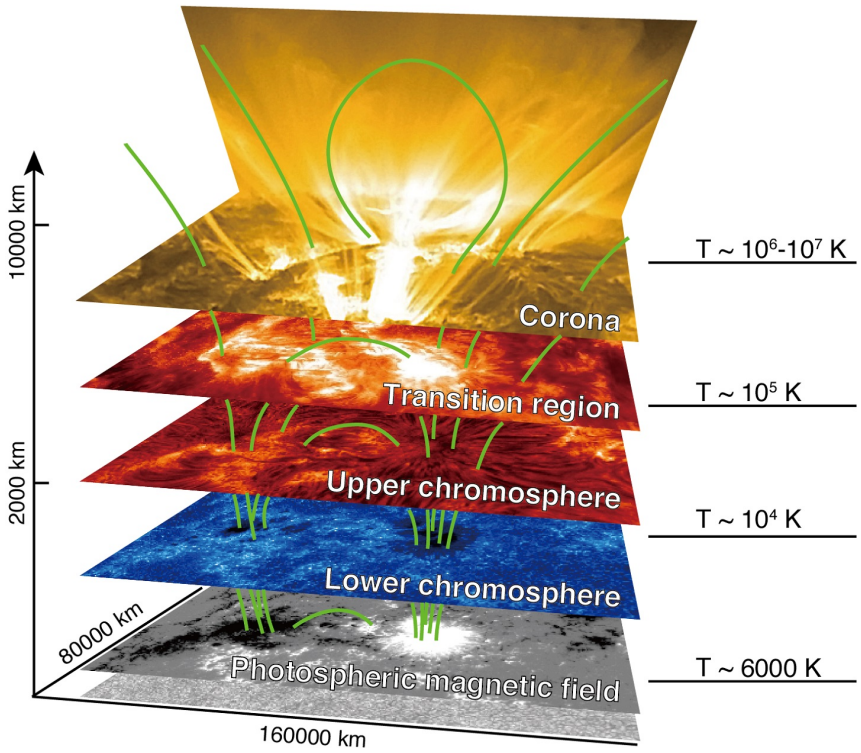

Fig. 1.2. Representation of the different layers of the solar atmosphere. Each of them is connected by the magnetic field lines. The solar surface with a temperature of ~ 6 000 K, seen in the visible light, is the photosphere. The chromosphere, up to about 2 000 km, reaches a temperature of about 10 000 K. The transition region is a thin layer making the transition between the chromosphere and the corona, which is the hot upper atmosphere (~ 10^6 K). Credit: NAOJ/JAXA, NASA.

surface (Clette 2022; Choudhuri 2015; Foukal 2004). This temperature gradient becomes greater than the adiabatic gradient and this makes the gas unstable leading to the energy being transported by turbulent convection (Stix 2004). In this layer, energy is carried by these convective motions much faster than in the radiation zone and takes approximately 35 days to travel from the bottom to the top of the convective zone (Eggleton 2006). This occurs at the layer known as the solar surface, which defines the base of the solar atmosphere.

1.1.1.2 Solar atmosphere

The solar atmosphere is the outermost part of the Sun and consists of several layers, extending from the photosphere to the corona, passing through the chromosphere and the transition region (Figure 1.2). Multiple dynamical processes occuring in the solar atmosphere are influencing the entire solar system.

The photosphere is the lowest layer of the atmosphere, corresponding to the visible surface of the Sun with a temperature of about 6 000 K. More precisely, as we can see in Figure 1.3, the Sun emits most of its radiation in the visible range (380 nm - 780 nm), equivalent to a 5770 K

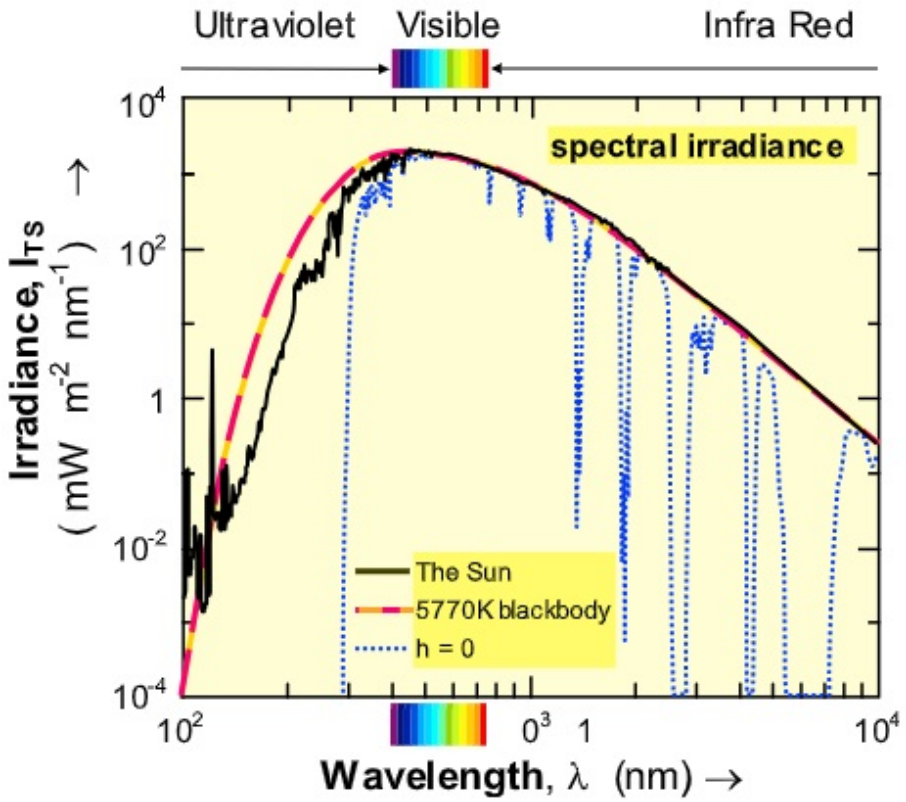

Fig. 1.3. Comparison between the spectrum of the solar irradiance (black line) and a 5770 K blackbody (red dashed line). The blue dotted line shows the spectrum of radiation reaching the surface of the Earth. Adapted from Gray et al. (2010).

black body which would produce the same total energy output as the Sun (Chatzistergos 2017). This thin layer of about 500 km depth (Clette 2022) is the place where the visible light is emitted that dominates the Sun's spectral energy distribution. The photosphere is the region where the sunspots are observable. Those structures, darker than the rest of the surface, are regions of intense magnetic field concentrations and manifestation of the solar activity. In these regions, the strong magnetic fields inhibit the internal convective motions, thereby blocking the transport of energy from lower layers and leading to a lower temperature compared to the surroundings photosphere.

The main characteristic that differentiates the photosphere from the next layer, the chromosphere, is the inversion of the vertical temperature gradient in the latter. In the chromosphere, because of magnetic reconnection and acoustic waves being sources of heating (Morita et al. 2010; Liu 1974), the temperature is increasing with altitude. This layer extends for about 2 000 km and reaches a temperature of 10 000 K (Jenkins 2009). Various structures can be observed in the chromosphere: sunspots, plages, the chromospheric network, spicules, prominences and flares. Unlike the photosphere, which is a relatively "flat" and homogeneous layer, the chromosphere is a significantly more inhomogeneous layer with more vertical structures, such as spicules and prominences, which are dense and absorbing structures. This layer provides crucial information on the Sun's

magnetic activity, driven by the solar dynamo.

The transition region, marking the top of the chromosphere (and base of the corona), is a narrow layer (thickness less than 100 km) where heat flows down from the corona into the chromosphere. This layer is characterized by a very high temperature gradient that rises dramatically from $\sim 10^4$ K to $\sim 10^6$ K in the corona. The latter is a region of extreme temperatures and low density where the coronal mass ejections (CMEs) and solar wind originate which have a strong impact on our planet. As the solar wind expands outward, it fills a region of our Solar System known as the heliosphere which extends well beyond the planets of our Solar System.

1.1.2 The magnetism of the Sun

1.1.2.1 Solar dynamo

The magnetism is the key to understand the Sun's activity. The Sun's magnetic field is widely thought to be produced by a magnetic dynamo operating within the Sun. However a general question remains: where does the solar dynamo originate?

Let's have a look at what is happening inside the Sun. The matter of the Sun is in an extremely hot gaseous state. These extreme temperatures of several million degrees are sufficient to remove electrons from atoms, creating positively charged particles called ions. This hot mixture of electrons and ions forms a distinct state of matter, called "plasma". Because of the negative charges of the electrons and the positive charges of the ions, electric currents can flow through it. Those currents are the source of the magnetic field consisting in loops of lines of force. But the specificity of the Sun is that the plasma located at the surface is rotating at different speeds, depending on the latitude. This is called the differential rotation. Moreover, the plasma is also rotating differently with depth inside the Sun. In the solar interior, the tachocline marks the transition from a uniform rotation in the radiative zone to a differential rotation in the convective zone (Hughes et al. 2007; Strugarek et al. 2023). This is expected to generate a large scale magnetic field through the dynamo effect. This large-scale magnetic field is subsequently distorted by differential rotation at the solar surface. Indeed, as seen in Figure 1.4, the matter at the Equator rotates faster (rotation period = 25 days) than the one present at the Poles (rotation period = 35 days). The value of 27.27 days, corresponding to the mean rotation period of sunspots, is usually taken as the solar rotation period, called the Carrington rotation period and named after the English amateur astronomer Richard Christopher Carrington (1826 – 1875) whose sunspot observations revealed the differential rotation of the Sun (Bhattacharya et al. 2021). This rotation period forms the foundation of the solar coordinate system and Carrington solar rotation numbering, a system widely used for tracking and mapping solar features over time.

The differential rotation plays a crucial role in the magnetic activity because it leads to the twisting of the Sun's magnetic field by converting the poloidal field to a toroidal field. As seen in Figure 1.5, a poloidal field is the configuration where the magnetic field lines are in the direction

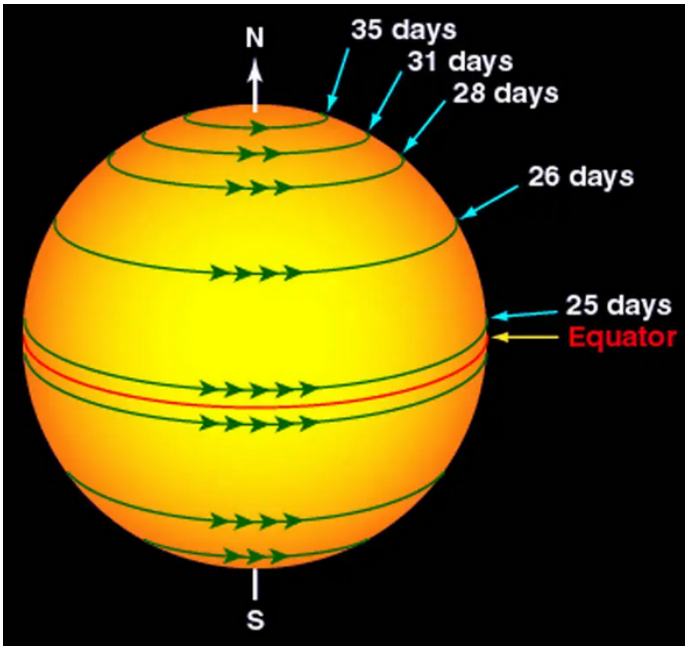

Fig. 1.4. Differential rotation at the solar surface. The image shows the days needed to complete a full solar rotation depending on the position from the Equator to the Poles. Credit: NASA.

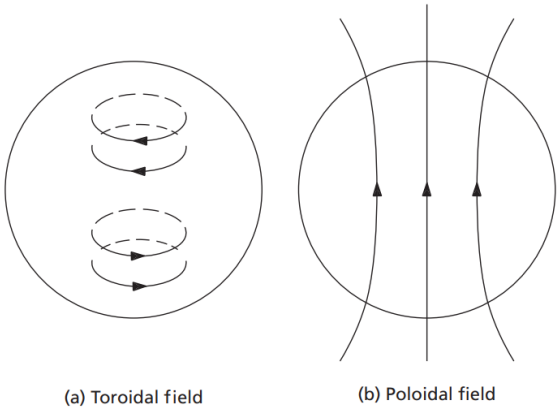

Fig. 1.5. Illustration of (a) toroidal magnetic field lines and (b) poloidal magnetic field lines. Image taken from Choudhuri (2015).

towards the Poles, while the toroidal field has magnetic field lines perpendicular to the rotation axis. This conversion of the poloidal field into a toroidal field is called the Ω-effect, after the Greek letter used to represent the rotation (Kitchatinov 2014; Cameron et al. 2017; Noraz et al. 2022). To close the cycle, it is necessary to come back to the initial state, the poloidal magnetic field.

Figure 1.6 shows the key stages of the cyclical process of the solar dynamo. The successive steps of the process are explained here after, following the letters of the schematic representation in the figure.

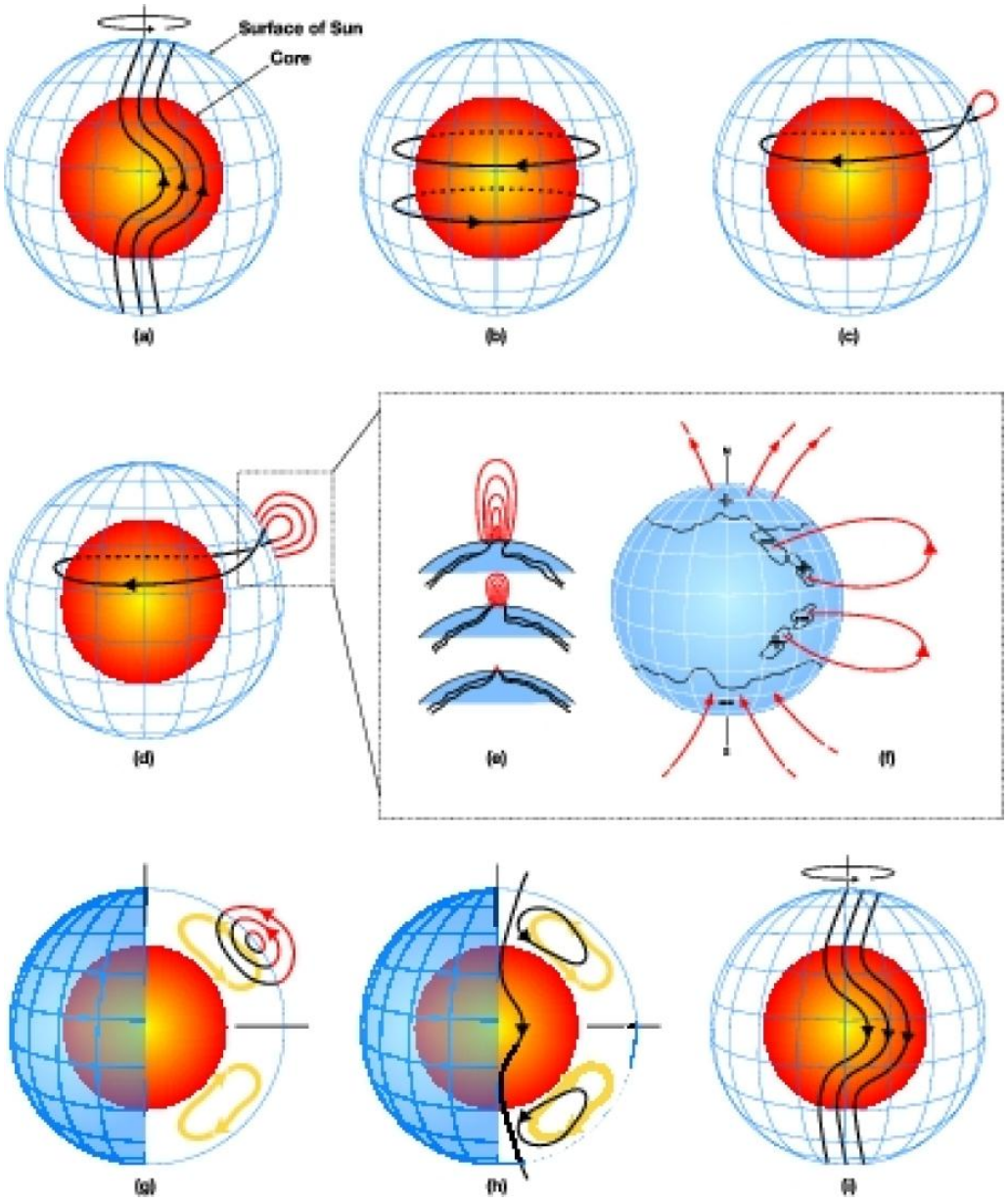

Fig. 1.6. Illustration of the processes in the solar dynamo. Red inner sphere represents the lower boundary of the convective layer and the blue grid the solar surface. The different steps, from (a) to (i) are explained in the text. Credit: High Altitude Observatory[4]

(a) Initially, at the beginning of the solar cycle, the magnetic field is a poloidal field that connects the two Poles, parallel to the rotation axis. Due to differential rotation, the magnetic field lines are stretched and wound all around the Sun.

(b) This winding causes the conversion of the poloidal field into a toroidal field.

(c) When toroidal field is strong enough, the magnetic field lines rise to the surface, like a bubble, due to the magnetic pressure that is building up in the toroidal flux rope.

[4] https://www2.hao.ucar.edu/hao-science/science-topic/sun-as-a-dynamo

(d) Under the effect of solar rotation, this loop undergoes a twist and emerges slightly inclined in the North-South direction.

(e) The exit and entry points of the magnetic loop produce sunspots. If these points are well separated from each other, two or more sunspots will be produced. But the loop can exit and re-enter at the same point: it is the case if one polarity is concentrated enough to yield a sunspot, while the other polarity is dispersed.

(f) Sunspots have magnetic fields with a polarity opposite to the polarity of sunspots groups of the previous solar cycle.

(g) In the convective zone, the meridional flows (yellow lines) between the Equator and the Poles carry the trailing polarity to the Poles and the leading polarity towards the Equator, where it cancels out with the inverse polarity from the other hemisphere. This transported residual flux initiates a polarity reversal.

(h) Gradually, the magnetic polarity of the Poles is cancelled and then reversed.

(i) A poloidal magnetic field is re-established, identical to the initial situation, but with the opposite magnetic polarity. The cycle is complete and can start over again.

In the case of the Sun, the whole cycle, going from a state with a poloidal field to the reversal of the polarity and the onset of a new cycle, takes about 11 years and is called the solar cycle. The return to the same magnetic configuration thus takes two solar cycles, i.e. about 22 years, the so-called Hale cycle.

1.1.2.2 Solar cycle

Sunspots were discovered with the invention of the telescope in the early 17th century by astronomers like Thomas Harriot, Johann Fabricius, Christoph Scheiner and Galileo Galilei. Sunspots drawings were made, providing us with a precise record of these structures for several centuries. In the mid-19th century, the German amateur astronomer, Heinrich Schwabe, discovered a variation of the number of sunspots, from his own observations. It is only a few years later that the swiss astronomer Johann Rudolf Wolf collected past historical data to study the evolution of the number of sunspots and determined the mean cycle period of 11 years, called the solar cycle.

Figure 1.7 represents the International Sunspot Number (ISN), which is still produced as the continuation of the series at the World Data Center SILSO[5] (Sunspot Index and Long-term Solar Observations), located in Brussels at the Royal Observatory of Belgium (ROB), from which a network of 80 stations is coordinated and continues the uninterrupted monitoring of solar activity. The 11-year variation illustrates that the Sun goes through periods completely calm, without any structures on its surface, called solar minimum, to periods of intense activity, known as solar maximum, during which the number of sunspots can reach up to 300 (Clette 2022). We can observe that the amplitude of the cycles are not constant. The level of solar activity varies from one cycle to another and is probably caused by nonlinear and random effects (Cameron et al. 2014).

[5] https://www.sidc.be/SILSO/home

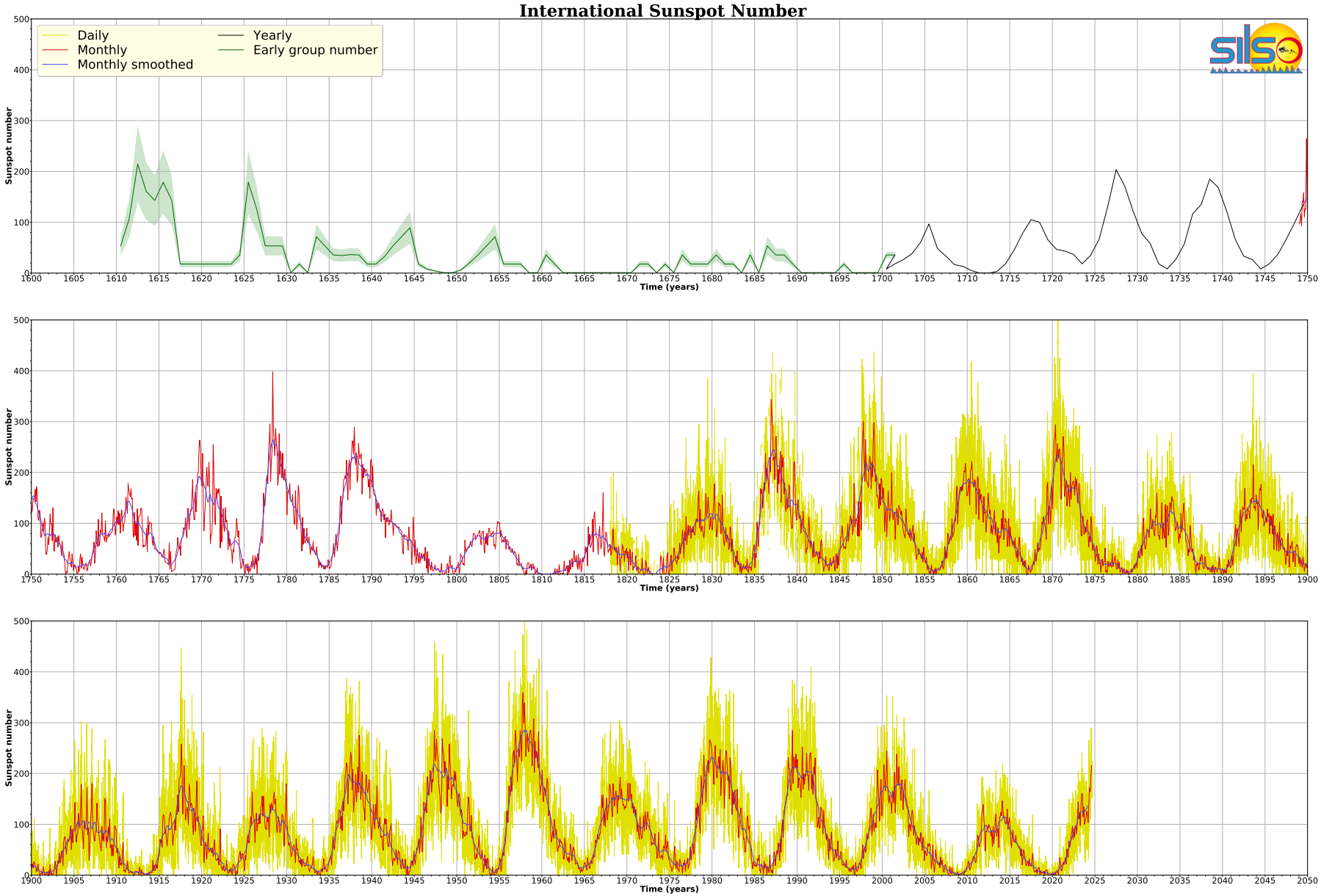

Fig. 1.7. International Sunspot Number since the first sunspots observations in the beginning of the 17th century up to the present. Four different curves are displayed: daily values (in yellow), monthly mean values (in red), monthly smoothed values (in blue) and yearly mean values (in black). Credit: World Data Center, SILSO, Royal Observatory of Belgium (https://www.sidc.be/SILSO/home). Software and plot design by Frédéric Clette.

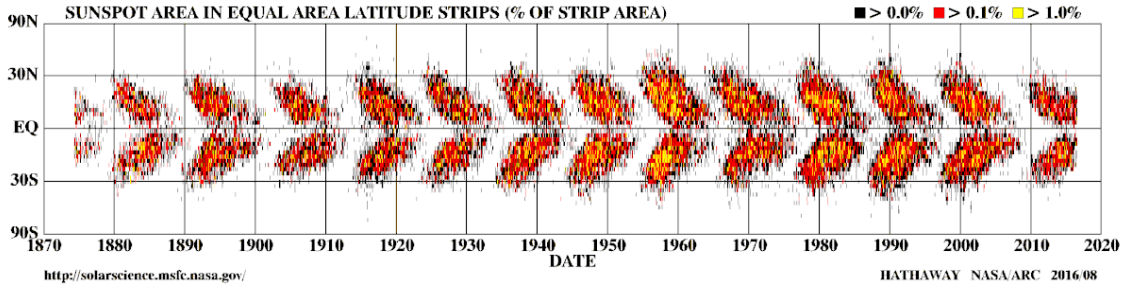

Fig. 1.8. Butterfly diagram highlighting the positions of sunspots during the solar cycles. Credit: http://solarscience.msfc.nasa.gov/images/bfly.gif

Despite the regularity of the cycle, there are specific periods where the solar activity was drastically low during several decades. The first epoch when such a phenomenon was observed was between 1645 and 1715, during which astronomers observed significantly less sunspots than usual, or even none at all. Known as the Maunder Minimum, this period coincides with the Little Ice Age, a phase of cooler global temperatures on Earth, leading to a theoritical suggestion of a connection between solar activity and climate change. The other period of minimum activity happened between 1790 and 1830, called the Dalton Minimum, and strangely this moment coincides also with a period of below-average global temperatures. Those phases of low level of solar activity remain a key to understand the solar cycles and their effects on Earth's climate (for e.g. Lean & Rind 1998; Lockwood et al. 2010; Solanki et al. 2013; Owens et al. 2017.

The number of sunspots is not the only systematic variation that happens in the Sun. The position of the sunspots on the solar disk also varies with the solar cycle. It depends on the strength of the activity cycle, being higher in large cycles at maximum than in small cycles (Becker 1954; Waldmeier 1955). However, regardless of the amplitude, sunspots appear within a limited latitude band, at an average latitude of $\sim 25°$ at the beginning of the cycle (Hathaway 2010), and those active bands progressively shift towards the solar Equator. This migration occurs almost symmetrically in both hemispheres. Figure 1.8 shows the position of the sunspots in latitude over time, and this graph is known as the "Butterfly diagram".

Thanks to the first observations of the astronomers in the 17th century, the time series of measurements of the sunspot number is the longest data in Solar Physics. It is a key dataset as it represents the most important diagnostic of the magnetic activity of the Sun on timescales of up to several centuries.

1.1.2.3 Magnetic features

The effect of the solar magnetic field can be diagnosed by observing different structures across the different layers of the atmosphere. At the solar surface, in the photosphere, the most prominent magnetic features are the sunspots (see Figure 1.9). The size and shape of sunspots are very diverse: the smallest spots are simple black dots, while the more developed ones always

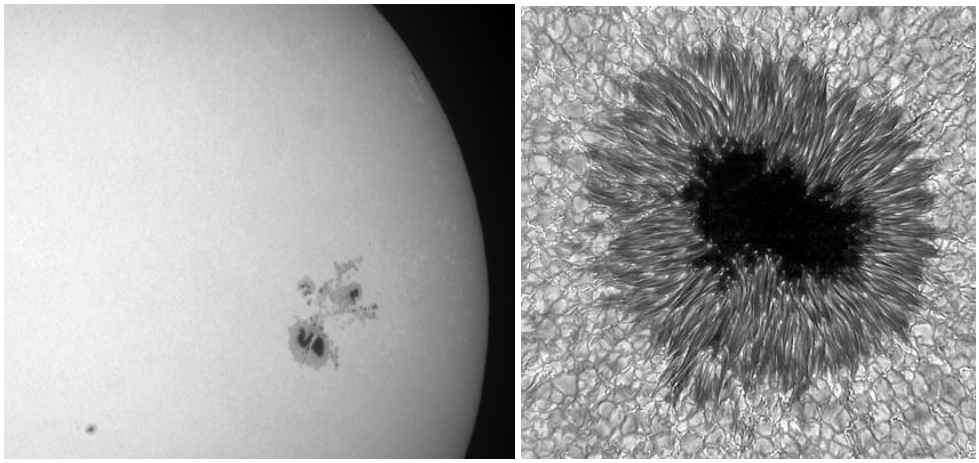

Fig. 1.9. Left image: Solar photosphere in white-light with two different groups of sunspots. The image was taken on October 26, 2014 with USET, the Uccle Solar Equatorial Table (Credit: Solar Influences Data Analysis Center (SIDC[6]), Royal Observatory of Belgium). Right image: A sunspot in high-resolution. The penumbra and the umbra of the sunspot are clearly visible (Credit: Friedrich Woeger, KIS, and Chris Berst and Mark Komsa, NSO/AURA/NSF).

consist of a penumbra surrounding a darker core, the umbra, as seen on the right picture of Figure 1.9. Those structures are dark and cold regions because the convective motions are blocked by the strength of the magnetic field escaping from the surface in a form of a flux tube (see Figure 1.10). Therefore, with a temperature of $\sim$ 4 000 K, sunspots appear darker than the rest of the surface. The magnetic field strength of a sunspot is varying from $\sim$ 700-1000 G in the penumbra up to 3700 G at the center of the sunspot, depending on the size of the spot. The magnetic field is stronger and the temperature is lower in the umbra of larger spots (Brants & Zwaan 1982; Kopp & Rabin 1992; Solanki 2003; Borrero & Ichimoto 2011; Rezaei et al. 2012; Kiess et al. 2014). They can form individually or in groups, where each spot forms a foot-point of a loop of magnetic field lines, and they live at least for a few hours.

The rest of the surface is covered with a grainy texture like the skin of an orange, known as solar granulation (see Figure 1.11). This texture is produced by the transport of hot gas from the convective zone and contains bright and dark areas. The bright areas, called granules, reflect the top of a rising column of hot plasma to the surface. Then, as the plasma cools off at the surface, it finally sinks back into the solar interior between the granules into intergranular lanes, represented by the dark areas (Jenkins 2009; Dalal et al. 2023). Those structures are very dynamic, each granule is replaced by a new one in about ten minutes. Due to their small size, with an average diameter between 500 and 1500 km, the granules are only observable with high-resolution telescopes (Jenkins 2009; Rieutord et al. 2010; Clette 2022). In addition to the granulation, large-scale cellular pattern have been observed in the solar photosphere, known as the supergranulation. Discovered by Hart (1954), the supergranulation cells are much larger structures, with a diameter

[6] https://sidc.be/

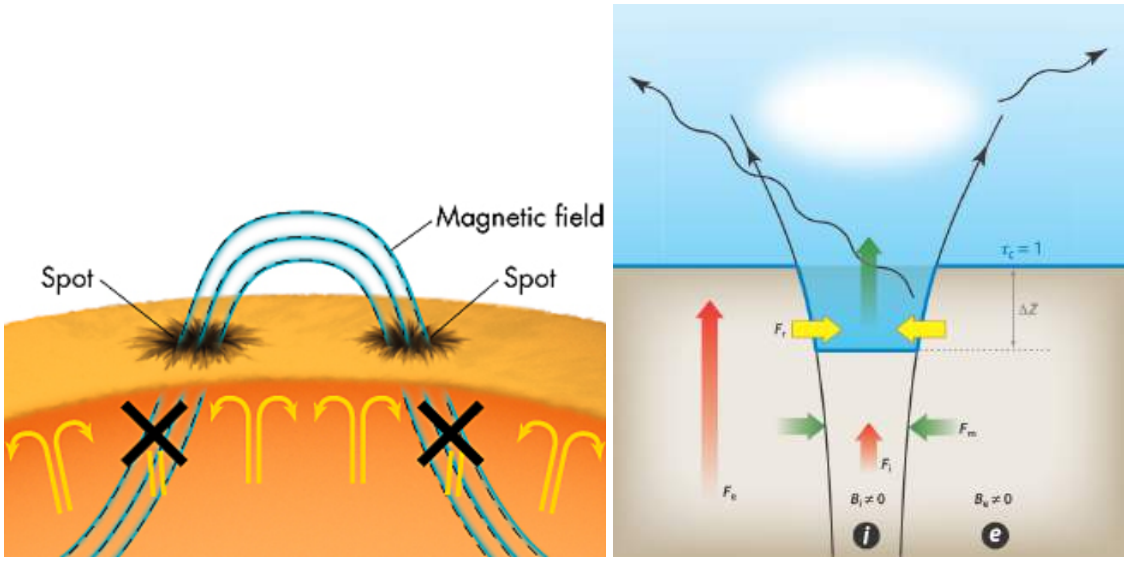

Fig. 1.10. Left image: Schematic view of magnetic field lines inside the convection zone rising through the surface in a form of flux tubes. Convection (represented as yellow arrows) is blocked where the magnetic fields lines break through the surface, cooling down the plasma and creating the dark features, called sunspots. Credit: New Jersey Institute of Technology - (Lecture 18)[7]. Right image: Schematic drawing of a magnetic flux tube. Arrows illustrate the forms of energy transfer. Red arrows: Vertical convective motions inside and outside the flux tube. Yellow arrows: Horizontal influx of radiation through the flux tube walls. Green arrows: Mechanical energy flux. The thick blue line represents the optical depth unity, τ_c. Image taken from Chatzistergos (2017) adapted from Zwaan (1978) and description from Solanki et al. (2013).

ranging from 12 Mm to 35 Mm (Simon & Leighton 1964; Hagenaar et al. 1997; De Rosa & Toomre 2004; Del Moro et al. 2004; Hirzberger et al. 2008; Chatterjee et al. 2017). Unlike the granules which display vertical plasma motions, supergranules are characterized by horizontal plasma flows (Simon & Leighton 1964; Hathaway et al. 2002; Rast 2003; Del Moro et al. 2004), associated with convective motions (Leighton et al. 1962).

Another feature is observable in the photosphere, but only near the limb of the solar disk: the faculae (Figure 1.12). When sunspots disappear, most of the initially generated magnetic field persists but concentrated in much smaller bundles than in sunspots and the magnetic field inside the faculae is not strong enough to produce a sunspot. Faculae are observed as bright streaks mainly around or near the sunspots. As illustrated in Figure 1.10, the convective motions are blocked by the magnetic field inside the flux tube, reducing the opacity and lowering the level of the optical depth $\tau_c = 1$ (thick blue line in the right panel of Figure 1.10). The walls of the flux tube maintain the same temperature as the outside of the tube, hence warmer than the interior. Since the magnetic field inside the flux tubes forming faculae is not strong enough to produce a sunspot,

[7] https://web.njit.edu/~cao/320.htm

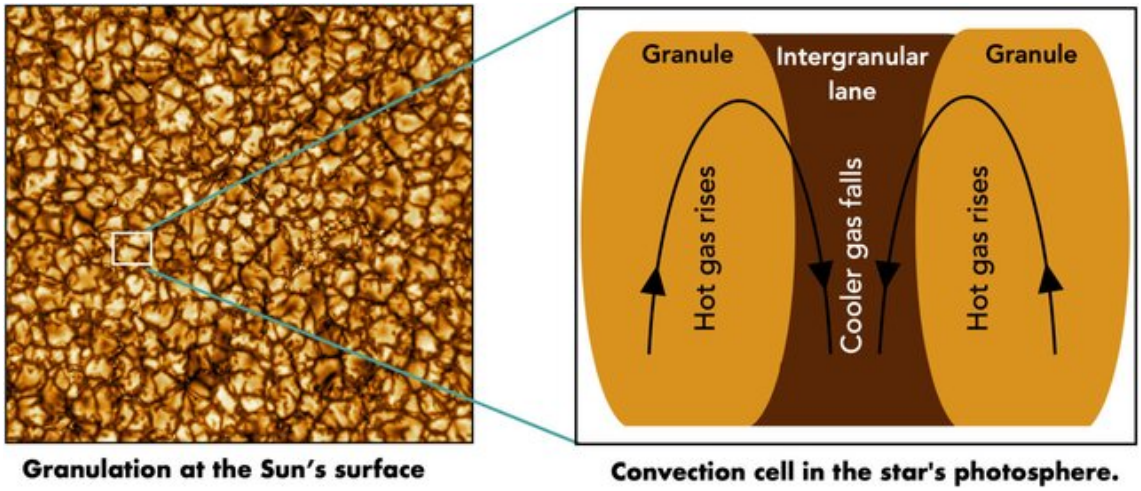

Fig. 1.11. Solar granulation. Left panel: High-resolution image of the solar granulation taken by the largest current solar telescope, DKIST (Daniel K. Inouye Solar Telescope). Right panel: Illustration of the convective motions in the granulation cells, where hot gas rises in the granules (orange region) and falls in the intergranular lane (dark brown region). Image taken from: Dalal et al. (2023).

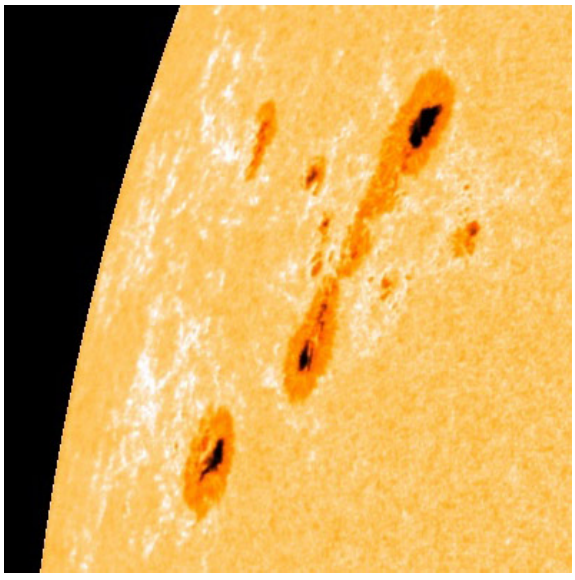

Fig. 1.12. Sunspots group surrounded by faculae in the photosphere. Credit: HMI, Solar Dynamics Observatory, NASA.

the tubes remain sufficiently narrow, allowing their walls to be observed, rendering them brighter, particularly near the limb, where they are viewed from the side. At the center of the disk, with a vertical view, faculae are invisible because the walls are not observable.

The flux tubes producing the sunspots expand into the chromosphere, where the low density of the plasma causes the magnetic field to dominate, constraining the plasma to concentrate and flow only along the magnetic fields. The chromospheric features are mainly observed using the

Ca II K and Hα lines. An example of observation in both lines is shown in Figure 1.13. Except for sunspots, observations in those lines display different structures than in the photosphere. In the Hα line, we can observe some dark and thread-like features, called filaments, which consist of dense and cool material suspended above the solar surface. The most notable structures observable in this chromosphere, more specifically in the Ca II K line, are the bright extended features surrounding the sunspots, called bright plages, with a temperature up to 11 000 - 12 000 K (Molnar et al. 2019; da Silva Santos et al. 2020). Those regions, which are the counterpart of the photospheric faculae, are associated with the concentrations of magnetic fields. They are hotter thus brighter than the rest of the Sun. This heating is thought to be the result of mechanisms like the magnetic reconnection, accoustic waves or wave dissipation (Osterbrock 1961; Liu 1974; Morita et al. 2010; Ni et al. 2018; Soler et al. 2019; Morosin et al. 2022; Priest 2023). Due to their important brightness, they are the main contributors to the chromospheric emission. The rest of the solar chromosphere is covered by the chromospheric network (CN) and the quiet Sun (QS). The CN is a bright web-like pattern formed by small magnetic flux concentrated at the boundaries of supergranulation cells. The darker cell interiors, where magnetic fields are weak or absent, form the QS. Worden et al. (1998) classified the CN into three structures differing mainly through their intensity : the enhanced network (EN), the active network (AN) and the quiet network (QN). But they also defined them by their size. While the EN is commonly believed to correspond to spatially coherent regions of decaying plages, the AN is related to smaller longitudinal dispersed remnants and the QN to the boundaries of the network (Worden et al. 1998; Singh et al. 2023). A plage is a wide extended structure and when it disperses and fragments, it is gradually replaced by an EN that keeps dispersing until it vanishes into the QN.

The magnetic features emerging in the form of loops extend up to the solar corona (see Figure 1.14) where the Sun can release a huge amount of energy due to magnetic instabilities that form in its atmosphere. These instabilities, which lead to phenomena such as solar flares and CMEs, can release solar particles towards the Earth and cause severe damage to our electromagnetic infrastructures both in space (satellites) and on the ground. As the solar wind particles reach the Earth, they interact with the geomagnetic field, which acts as a protective shield. The dipolar shape of the Earth's magnetic field allows some of the solar wind's charged particles to enter the Earth's magnetosphere. As these charged particles spiral around the magnetic field lines, they flow towards the polar regions and penetrate the upper atmosphere of the Earth in regions close to the North and South Poles. There they collide with the molecules and atoms of the atmosphere. In this way, they excite specific atomic transitions that lead to the auroral emission.

1.2 The stars and their activity

The universe is filled with stars, but what do we know about their magnetic activity? This Section gives an overview of the classification of stars and the place of the Sun among stars in

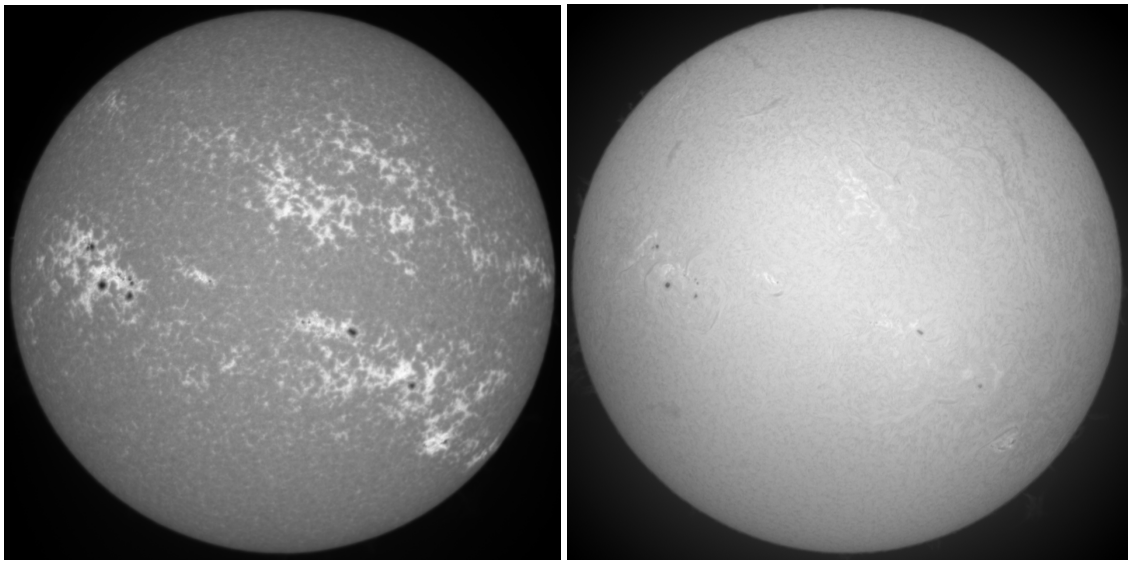

Fig. 1.13. Image of the solar chromosphere in the Ca II K line (left) and in the Hα line (right). The images were taken on May 19, 2024 with the Uccle Solar Equatorial Table (USET). Credit: Solar Influences Data Analysis Center (SIDC[8]), Royal Observatory of Belgium.

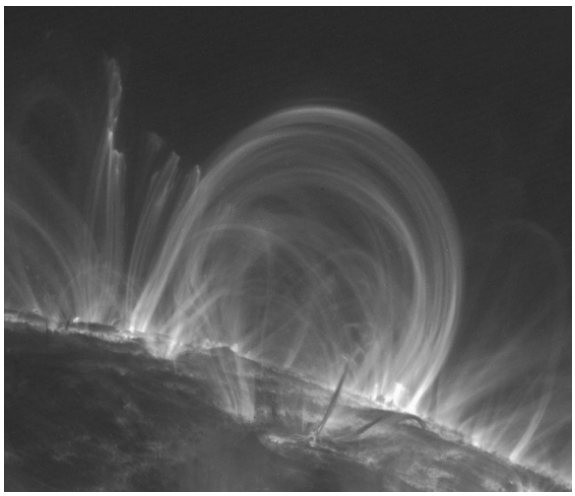

Fig. 1.14. Magnetic loops above the solar surface in the corona. The image was taken by the space mission Transition Region and Coronal Explorer (TRACE) on November 6, 1999. Credit: Stanford-Lockheed Institute for Space Research and NASA.

terms of magnetic activity.

1.2.1 Classification of stars

Stars differ by their age, their size, their temperature, their mass, their gravity, their luminosity, etc... and follow a different evolution depending on their properties. A crucial tool in stellar evolution theory is the Hertzsprung-Russell diagram (Figure 1.15) showing the relationship

[8] https://sidc.be/

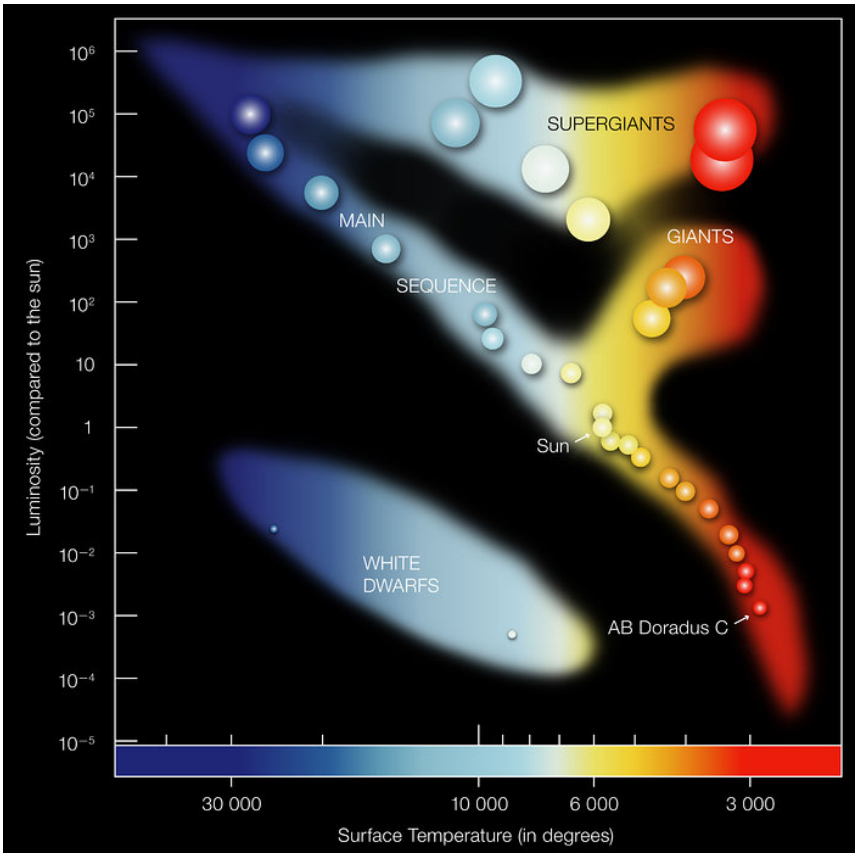

Fig. 1.15. In the Hertzsprung-Russell diagram, the luminosity of a star is plotted against its temperature. The position of a star in the diagram provides information about its present evolutionary stage and its mass. The first part of the life of stars is the diagonal branch, the so-called main sequence (MS). The Sun is still evolving in this branch. When a star leaves the MS, it becomes a red giant or a supergiant (top right corner), depending on its mass. Stars with the mass of the Sun or less, end their life as a white dwarf (bottom left corner). Credit: ESO

between the temperature of a star and its luminosity. In this diagram, the stars are not scattered randomly. The majority of the stars are distributed along a particular region called the main-sequence (MS), which is nowadays understood as the place where stars produce their energy via nuclear fusion of hydrogen in their core (Schrijver & Zwaan 2000; Foukal 2004; Clette 2022). Typically when stars are born, they spend most of their lifetime on the MS. Depending on their mass, they undergo a different evolution. For a low-mass or medium-mass star (with a mass $< 8M_{\odot}$ [9]), after its time on the MS, it becomes a red giant. Following core hydrogen exhaustion, the nuclear reactions change to hydrogen fusion in a shell surrounding the core. The star further evolves through core helium flashes and the fusion of helium leaves behind a core made of carbon and oxygen. In these stars, the temperature in the core cannot reach the value required to ignite the burning of carbon and the core then contracts whilst the outer layers are released creating a stunning cloud

[9] $M_{\odot}$ = Solar mass

known as a "planetary nebula". Meanwhile, the core of the dying star contracts into a white dwarf, an extremely hot, but very small object. For a high-mass star (with a mass > $8M_{\odot}$), the evolution proceeds differently. The temperature in the core of these stars reaches values that are sufficient to initiate the nuclear burning of carbon. Following the exhaustion of hydrogen in the core, they thus undergo a sequence of nuclear fusion reactions resulting in the production of heavier elements, successively C, Ne, O, Si and eventually Fe. Whereas the fusion of C, Ne, O and Si releases energy, the combustion of Fe requires an input of energy. As a result, the reactions come to an end and the core, which can no longer sustain the weight of the layers above, collapses into a neutron star or a black hole whilst the outer layers are ejected in a gigantic supernova explosion.

While each star exhibits unique characteristics, they can be categorized based on specific parameters. A system was created to classify stars of the MS according to their spectral characteristics by single letters of the alphabet. The spectral types indicate the temperature of the star and are listed based on temperature in decreasing order, from hottest to coldest (see Figure 1.16). The whole sequence of spectral types is O, B, A, F, G, K, M. The hottest stars are of spectral type O, followed by spectral types B and A. The coolest stars are of spectral type M. A second dimension of the spectral classification (not displayed in the figure) is provided by the luminosity class which is indicated by a roman number from I (supergiants) to III (giants) and V (dwarfs). For our work we focus on stars that are similar to the Sun. Those stars, called "Sun-like stars", "solar-type stars" or "solar twins", correspond to cool, main-sequence stars with convective envelopes and of spectral classes F, G and K. Moreover, they have the similar fundamental parameters like the effective temperature and metallicity as the Sun. But do they have the same magnetic activity?

1.2.2 The Sun among stars

Stellar activity, especially in stars similar to our Sun, remains a fascinating and critical area of research in astrophysics. Understanding how the Sun compares to Sun-like stars in terms of variability and magnetic activity cycles can provide profound insights into the mechanisms driving stellar magnetic activity. Over the past sixty years, significant progress has been made in the study of cool stellar chromospheres. In 1966, Olin Wilson launched the Mount Wilson Observatory HK Project (Wilson 1968; Vaughan et al. 1978; Baliunas et al. 1995) to investigate stellar magnetic activity and variability through the chromospheric emission in the Ca II K line. This project, which has observed over 2 000 stars, has significantly deepened our understanding of chromospheric physics, offering valuable insights for comparing the Sun with other stars. The Mount Wilson monitoring program revealed several significant insights. It demonstrated that the Sun is not unique in exhibiting periodic activity cycles (Baliunas et al. 1995): such behavior is common among solar-like stars. However, many solar-like stars do not have periodic activity cycles like the Sun, displaying other forms of variability. Baliunas et al. (1998) have found that 60% of the lower main-sequence stars exhibit periodic variations in their magnetic activity, 25% display fluctuations of activity that do not follow a clear periodic cycle, and the last 15% consists of

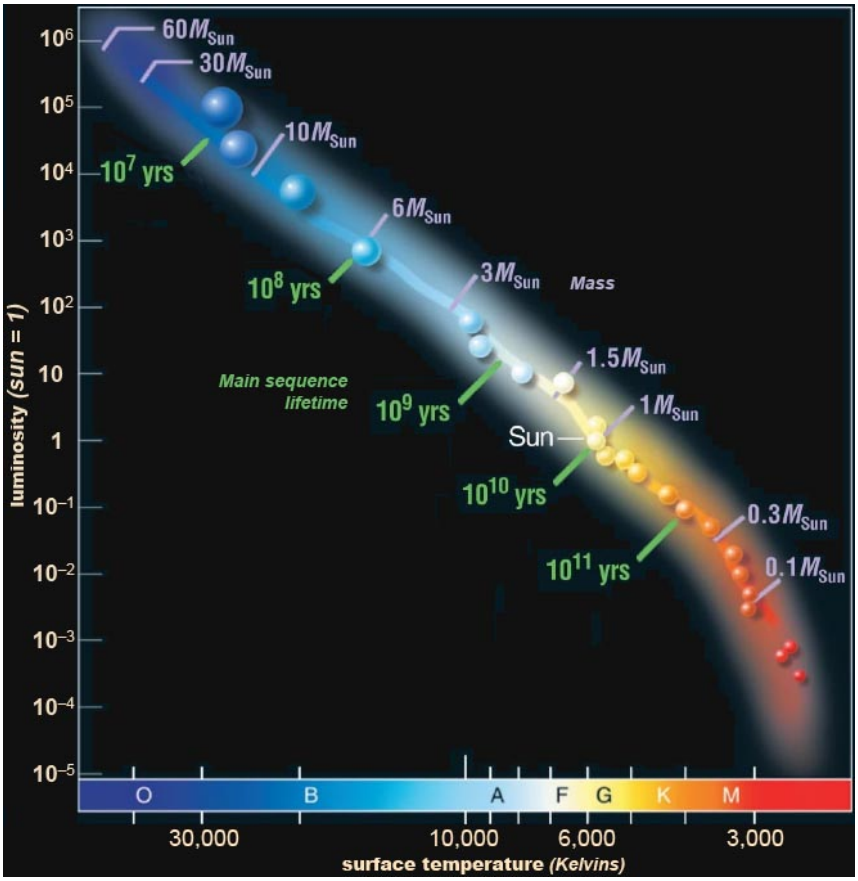

Fig. 1.16. Spectral classification of main-sequence stars. Source: https://www.handprint.com/ASTRO/specclass.html

stars with constant emission, the so-called "flat activity stars". Schröder et al. (2013) have shown that highly active stars often show chaotic variations, while flat activity stars have a very low chromospheric activity. In another paper, Schröder et al. (2012) validated a long-held hypothesis that these flat activity stars represent the "zero-point" of stellar activity, characterized by only a basal chromospheric flux. This behavior is akin to the entirely inactive Sun observed during the period of the solar minimum in 2008-2009. This prompts the investigation into the origin of these different types of activity and the creation of this basal chromospheric flux, the minimum level of chromospheric activity. A specific period of very low solar activity (number of sunspots significantly lower than today) was recorded between 1645 and 1715, known as the Maunder Minimum. During this period, the Sun was entirely quiet, and this universal phenomenon describes the "zero-point" of magnetic activity (Schröder & Schmitt 2013). However, this historical epoch of almost zero level of activity is not fully understood. Moreover, there is a strange coincidence between the Maunder minimum with the "Little Ice Age", a period of wide-spread cooling on Earth, leading to debates whether the solar activity acts as a climate driver.

Even though the periodicity of the magnetic activity cycle is common among Sun-like stars, studies have demonstrated that compared with the Sun, most solar-type stars exhibit different

photometric variability on the activity cycle timescale (Lockwood & Skiff 1990; Radick et al. 1998; Lockwood et al. 2007; Reinhold et al. 2020). It has been proposed by Schatten (1993) that this variability could be affected by the position of the observers. Indeed, as seen in the Butterfly diagram (Figure 1.8 in Section 1.1.2.2), the magnetic features are distributed within a limited latitude band and the position of the observer in the ecliptic plane relative to the rotation axis may affect their brightness. Many studies have successfully estimated the rotation periods of stars from a chromospheric activity index (Vaughan et al. 1981; Noyes et al. 1984a; Baliunas et al. 1985; Wright et al. 2004; Radick et al. 2018; Hempelmann et al. 2016), but they didn't account for the impact of inclination on the observed level of variability. While stars are observed at random and mostly unknown inclinations, it is essential to evaluate the influence of the viewing angle on the observed magnetic activity tracers to compare solar variability with that observed in other Sun-like stars.

In parallel, space-based missions have also revolutionized our ability to study stellar variability: e.g. Convection, Rotation and planetary Transits (CoRoT, Bordé et al. 2003; Baglin et al. 2006), Kepler (Borucki et al. 2010), and Transiting Exoplanet Survey Satellite (TESS, Ricker et al. 2014). The level of stellar magnetic activity is known to be related to the stellar rotation period (Skumanich 1972; Pallavicini et al. 1981; Noyes et al. 1984b), with young stars rotating more rapidly exhibiting irregular or shorter cycles, whereas old stars rotating more slowly showing clearer and more extended cycles. These high-precision observations have allowed scientists to explore the stellar variability more deeply on different timescales from hours to months (e.g. Basri et al. 2013; McQuillan et al. 2014). These observations confirm the link between stellar rotation and magnetic activity postulated in the dynamo scenario described above. This is further supported by observations in the X-ray domain which probe the coronal emission of solar-like stars in open clusters (e.g., Jeffries et al. 2006). The level of coronal X-ray emission is indeed well correlated with the overall chromospheric activity and active stars exhibit a cyclic modulation of their X-ray emission in phase with the activity cycles diagnosed from their Ca II K line emission (e.g., Robrade et al. 2012).

On the much longer timescales, i.e. the stellar age, the relationship between stellar activity and the age of stars has been extensively studied. Vaughan & Preston (1980) studied the chromospheric activity of Sun-like stars and they found a gap, called the Vaughan-Preston Gap, in the distribution of chromospheric activity levels between two distinct groups of stars: the active one, young stars with high levels of chromospheric activity, and the inactive one, old stars with much lower levels of chromospheric activity. This gap indicates that stars might shift quickly from a phase of high chromospheric activity to one of low activity. The reasons of this rapid transition and the underlying mechanisms are still subjects of ongoing research. More recently, Schröder et al. (2013) derived the position of Mount Wilson stars in the HR diagram to obtain their evolutionary status and mass distribution. They found that, during the MS part, stars are grouped according to their chromospheric Ca II K emission, showing a decrease in activity with age. The

most active stars are around the zero-age main sequence (ZAMS), moderately active stars are in the second quarter of the MS, almost inactive stars in the third quarter, and totally inactive stars in the final quarter. The Sun has a clearly defined cyclic activity and lies in the second quarter of the MS. Therefore, our star is approaching this transition phase to a weak magnetic activity state, as it was during the Maunder minimum period. In that sense, for Schröder et al. (2013), the historical solar Maunder minimum must be seen as a precursor of future conditions.

1.3 Motivations

Stellar magnetic activity, particularly in Sun-like stars, plays a crucial role in shaping our understanding of solar and stellar physics. The Sun's magnetic field influences solar variability, space weather, and indirectly, Earth's past climate. However, while solar magnetic activity has been studied extensively, many open questions remain about the physical processes that govern the Sun's magnetic activity and about how this activity compares to other Sun-like stars and stars at different stages of evolution. Due to the proximity of the Sun from Earth, its surface can be resolved to a great level of detail. This is not possible for the vast majority of other stars for which our studies have to rely on the integrated flux of light. The detailed observations of the Sun can thus help us to better understand the behavior of these objects. In addition, Sun-like stars are very important to understand the past and future of the Sun. Below, we provide a brief description of the motivations that inspired the thesis, explaining the reasons that have guided our research work.

1.3.1 Magnetic activity of Sun-like stars

Stellar parameters, like temperature, gravity, metallicity, mass, luminosity, age, etc... are very precise parameters but the magnetic activity of the stars is not well understood. Do solar twins have the same magnetic activity as the Sun? Is the dynamo process in Sun-like stars the same as that observed in the Sun? Many observations indicate that Sun-like stars exhibit other forms of variability in the periodicity of their activity cycle (see Section 1.2.2), with periodic, non-periodic and quasi-periodic cycles. Why is there such a disparity in the activity cycle? What is happening inside stars with a chaotic variation or with a constant emission? Understanding the physical processes occurring in other stars could improve our models of stellar evolution and magnetic dynamo processes.

1.3.2 Inclination of the stellar rotation axis

The rotation axis of a star can be inclined at any angle relative to our line of sight from Earth. In the case of the Sun, we observe it close to its equatorial plane, giving us a nearly direct view of its equatorial regions. However, the other stars are usually observed without information of their inclination. In that sense, as the solar magnetic structures are distributed between mid-latitudes and the Equator, the inclination of the rotation axis affects the observations of magnetic

features. The influence of the viewing angle on the Sun's magnetic activity has largely been investigated through synthetic images produced by simplified models and numerical simulations (Schatten 1993; Knaack et al. 2001; Shapiro et al. 2014; Borgniet et al. 2015; Meunier et al. 2019; Nèmec et al. 2020; Sowmya et al. 2021b). In this work, we use direct solar Ca II K observations to study it. To analyse the comparison between solar variability and that of other Sun-like stars, it is essential to quantitatively evaluate this dependence.

1.3.3 Implication for climate models

Nowadays, climate change is in the spotlight all around the world. Global warming is a fact, and humanity is trying to cope with this period by adapting its way of life, but there are natural factors on which we have no control, of which the Sun is definitely the main one. Indeed, many studies have demonstrated that the Sun had an influence on Earth's past climate (see e.g., contributions in Dudok de Wit 2016). The two periods of minimum of solar activity, the Maunder Minimum and the Dalton Minimum (shown in Section 1.1.2.2), are related with 99.99% probability to climatic cold periods (Schmutz 2021). We know that during those periods, the solar activity was very low (less sunspots than usual) but what did the Sun look like during the Maunder Minimum? Are these periods unique in the life of a star? Or will there be others? Even if the Sun has a minor role compared to anthropogenic factors, its impact on Earth's climate still needs to be better quantified for improving the accuracy of theoritical climate models and predictions of future events.

1.4 Organisation of the thesis

In Chapter 2, we present the data that we have used for our research. It consists of two different types of observations: the solar images in the Ca II K line from the USET station, located in Brussels, Belgium (Section 2.1) and the spectral measurements collected with the TIGRE telescope, located in Guanajuato, Mexico (Section 2.2). We explain the technical information on the telescopes as well as the data they produce.

Chapter 3 is dedicated to the data processing to extract the meaningful information from the USET Ca II K images. This includes data calibration, center-to-limb variation correction, structures segmentation method, synoptic map construction and reproduction of solar-disk views under different viewing angles. The processed data are then used for analysis and interpretation in the next Chapters.

Our first study (Vanden Broeck et al. 2024a), described in Chapter 4, confirmed the linear relationship between a disk-resolved index, from the USET solar images, and an integrated spectrum index, from the TIGRE flux measurements. We have also analysed the periodic modulations in the two datasets to detect the solar rotation and solar cycle periods.

The inclination of the rotation axis of a star is a significant parameter when studying the

chromospheric emission of stars. The effect of inclination on chromospheric activity is the focus of our second study (Vanden Broeck et al. 2024b), described in Chapter 5. By generating solar-disk views under different viewing angles based on the images at our disposal, we were able to analyse this dependence.

The final Chapter of the thesis, Chapter 6, summarizes the main conclusions of our research and discusses the future scope of this work.

Chapter 2

Solar observations

In this Chapter, we present the data that we used for our research, namely two types of observations: the solar images from the USET station, located in Brussels, Belgium and the spectral measurements collected with the TIGRE telescope, located in Guanajuato, Mexico. Our work is primarily focused on the USET data, which is produced everyday at the ROB. The TIGRE data were provided to us through our collaboration with researchers from the University of Hamburg and the University of Guanajuato, who are in charge of the telescope.

2.1 Full-disk solar images

2.1.1 USET telescope

The "Uccle Solar Equatorial Table" (USET) is a ground-based station (see Figure 2.1), located at the ROB in Uccle, Brussels in Belgium. The table was installed at the top of a tower of 10 meters height to avoid as much as possible the atmospheric turbulence. The table holds four distinct telescopes. One of them is a 160mm visual refractor dedicated to the sunspots drawings. Starting from the years 1940's, those drawings are still made nowadays with the same instrument to maintain a long-term database of solar activity. USET is part of the SILSO[1] network, which comprises over 80 observation stations in the world. Since 1981, it has been based at the Royal Observatory of Belgium, where sunspots drawings from the SILSO network are compiled to produce the ISN. The ISN represents the longest homogeneous record of solar activity, spanning approximately four centuries, and provides valuable data for solar physics research. A second telescope captures images of the solar photosphere in white-light (WL) with a 150mm aperture. A third one, with a 80mm aperture, observes the solar chromosphere in the Hα line. Both telescopes have been systematically capturing CCD observations since 2002. Finally, a fourth telescope, with an aperture of 132mm, was installed in 2012, dedicated to observing the chromosphere in the Ca II K line. USET allows for the daily monitoring of the solar activity. Ground-based observations,

[1] https://www.sidc.be/SILSO/home

Fig. 2.1. USET station at the Royal Observatory of Belgium, located in Uccle, Brussels. Left picture: The dome. Middle picture: The equatorial table. Right picture: The 4 optical instruments (WL telescope, visual refractor, Hα telescope, Ca II K telescope (from the left to the right)).

which have been performed for decades, provide the opportunity to study solar activity over the long-term. When the weather permits, USET acquires solar images 7 days a week during the whole year. On average, 260 days of observations are recorded per year. The gaps are essentially due to bad weather conditions.

In this study, we use the full-disk images of the solar chromosphere in the Ca II K line, starting in July 2012. The optical set-up consists of a refractor of 925 mm focal length and 132 mm aperture size. The images are captured with an interference filter calibrated for a temperature of 23°C with a low sensitivity to temperature and centered on the wavelength λ = 3933.67 Å, with a bandwidth of 2.7 ± 0.5Å. The type of the filter was chosen to be similar to the one adopted for many years by the Rome/PSPT instruments (more details in the next section), in order to ensure a maximum compatibility with this reference program, which operates since 1996. This filter offers a good transmission (>50%) but has a low temperature coefficient, which means a variation in the central wavelength of up to 0.6 Å between 0 and 30°C, which is 20% of the FWHM. However, it is stabilized by an electronic temperature regulator (in practice, within 0.2°C) to restrict these variations to less than 1% of the FWHM (Full width at half maximum). The images are acquired with a 2048 × 2048 CCD with a dynamic range of 12 bits and are captured at low cadence (every 15 minutes) or at very high cadence (up to 4 frames per second) in case of visible active phenomena (flares, eruptions). Since 2012, the instrumental set-up remained unchanged except for the installation of an additional neutral-density filter on July 10, 2013. The purpose of this filter is to set the normal exposure time in the range 1 to 10 ms. Such optimal exposures are long enough to ensure a sufficient signal/noise ratio while being short enough to minimize the loss of resolution due to the seeing.

2.1.2 Ca II K line

The Sun is observed in many different wavelengths, depending on which part of the atmosphere we want to study. The Ca II K line, located at 3933.67 Å in the electromagnetic spectrum, produced by singly ionized calcium, is one of the deepest and broadest absorption lines (Ermolli et al. 2018), making it one of the most important spectral lines used in the study of the solar chromosphere. Whilst most lines in the solar spectrum reach an optical depth of one only inside the photosphere, the huge opacity of the Ca II K line implies that an optical depth of one can already be reached in the chromosphere, provided there is enough material available in the chromosphere. This line is thus a powerful diagnostic of the presence of chromospheric material and has a high sensitivity to the presence of magnetic fields. It is characterized by three main components: K1, K2, and K3 (see Figure 2.2), each corresponding to different layers of the solar atmosphere. K1 and K2 are divided in two components, K1v, K2v, K1r and K2r, respectively towards the violet and red part of the spectrum relative to the line core. The figure shows two different line profiles, one for the plages and one for the quiet Sun. The Ca II K emission from the plages regions is considerably stronger than that for the quiet Sun because the magnetic field in plages regions is higher and the strength of the emission core depends linearly on the magnetic field intensity, up to $\sim$ 500 G (Skumanich et al. 1975). From the wings to the core, the lines samples the solar atmosphere with increasing height (see Figure 2.3). The figure starts at height zero, which corresponds to the solar surface, the photosphere. While the wings of the line are formed in the photosphere, the emission originates from the lower part of the chromosphere (Skumanich et al. 1984). The K1 components, formed around 500 km above the surface where temperature starts to rise, identify the minima between the emission peaks and the wings. Then, higher in the chromosphere, the two emission peaks K2 are formed. They appear as stronger emission features, indicating that the chromosphere is hotter in this region and more ionized calcium is present. Finally, the K3 component, corresponding to the central part of the Ca II K line, is formed in the upper chromosphere, at $\sim$ 2 000 km above the surface, where the temperature reaches a local maximum before the transition to the corona. Variations between those components allow astrophysicists to have information on temperature, density and motions in the solar chromosphere.

Ca II K observations are crucial to understand solar activity, including sunspots, plages, and faculae. A typical image of the chromosphere in the Ca II K line is shown in Figure 1.13. We can observe four important features: (1) the sunspots, which are the black spots, (2) the plages, corresponding to very bright and extended structures surrounding most of the time the sunspots, and the rest of the Sun consists of a structure like an orange skin with (3) the quiet Sun surrounded by (4) the chromospheric network, a slightly bright web-like pattern. An example of each structure is illustrated in Figure 2.4.

Systematic chromospheric observations started in the early 20th century, with observatories like Mount Wilson (Lefebvre et al. 2005), Kodaikanal (Hasan et al. 2010; Priyal et al. 2014; Chatterjee et al. 2016), Meudon (Malherbe & Dalmasse 2019; Malherbe 2023), and Coimbra

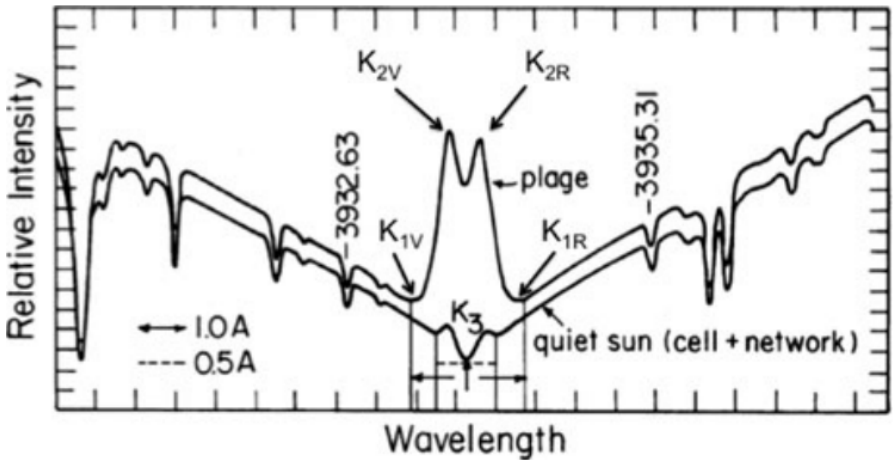

Fig. 2.2. Ca II K line profile for quiet Sun (lower curve) and plages regions (upper curve). Image taken from Ermolli et al. (2018).

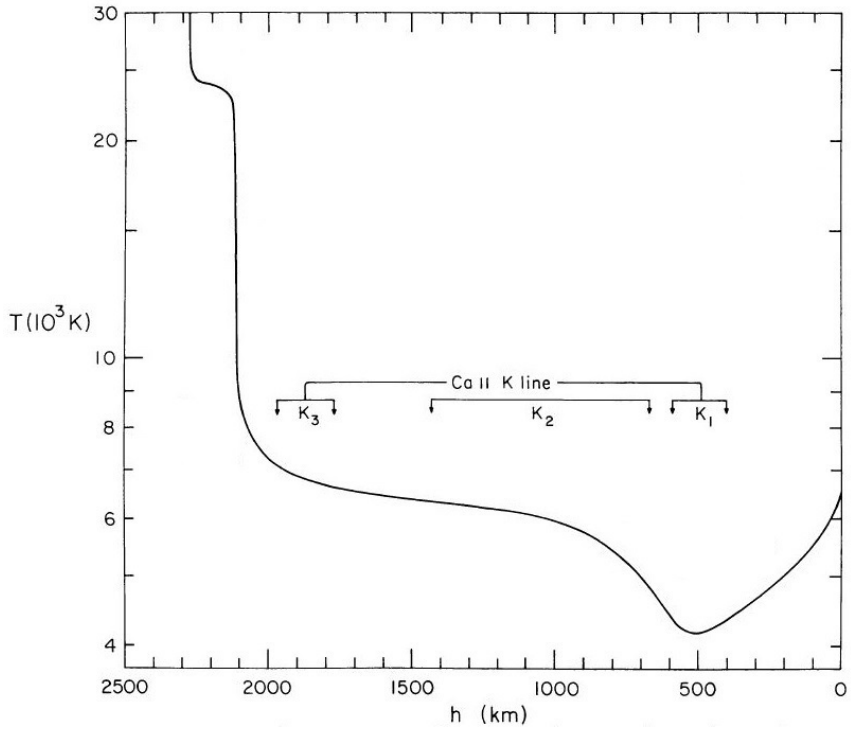

Fig. 2.3. Approximate formation heights for the components of the Ca II K line in the solar atmosphere from the surface. The solid line is the temperature profile. Adapted from Vernazza et al. (1981).

(Garcia et al. 2011; Lourenço et al. 2019), who provide a continuous record of solar observations over more than a century (Tlatova et al. 2019; Chatzistergos et al. 2020). As the solar cycle spans approximately 11 years, those historical datasets are valuable for studying the long-term solar variability.

To ensure precise data continuity, modern Ca II K projects play a crucial role. A prominent

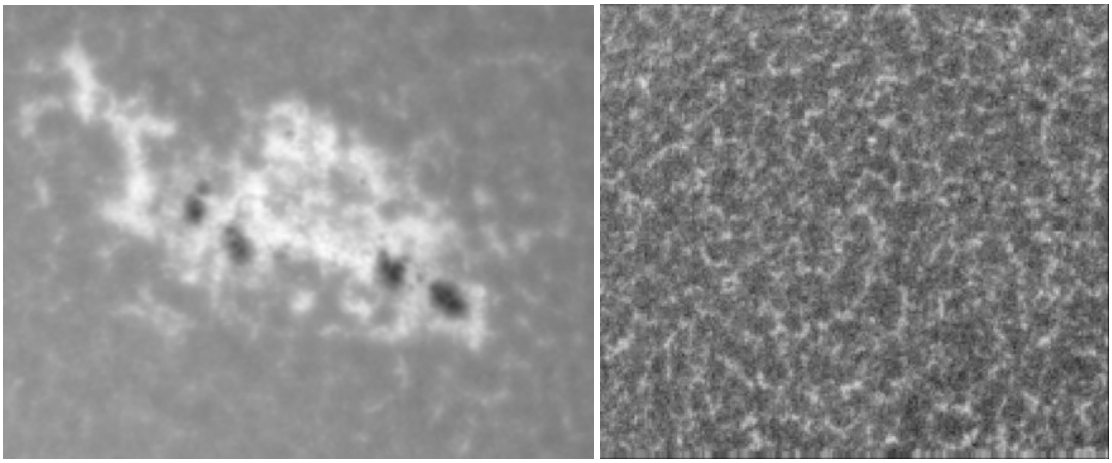

Fig. 2.4. Example of the important features of the chromosphere in the Ca II K line. Left picture: The bright plages surrounding the dark sunspots (Credit: SIDC, Royal Observatory of Belgium). Right picture: The quiet Sun (grey part) surrounded by the web-like bright pattern, the chromospheric network (Image taken from Judge & Peter 1998).

example is the RISE/PSPT project. RISE (Radiative Inputs of the Sun to Earth) is a scientific program aimed at understanding the physical mechanisms behind solar variability, its origin and its effects on Earth's climate (Kuhn & Foukal 1993). The PSPT (Precision Solar Photometric Telescope) is a 15 cm refracting ground-based telescope designed for synoptic solar observations, located at Monte Porzio Catone in Italy, and is operated by the INAF Osservatorio Astronomico di Roma (Ermolli et al. 1998, 2007). Since May 1996, the Rome/PSPT has been producing daily full-disk images with a 2048×2048 CCD camera. The images are taken with a 2.5Å bandwidth filter centered at the Ca II K line (λ = 3933.67Å), achieving approximately 0.1% photometric precision per pixel. These characteristics are almost identical to those of the USET Ca II K instrument, ensuring that the matching of the PSPT observations with those of the USET is optimal.

Moreover, the Ca II K line is also widely used to monitor stellar activity (Vaughan et al. 1981; Baliunas et al. 1985; Mittag et al. 2013, 2016; Hempelmann et al. 2016; Boro Saikia et al. 2018; Sowmya et al. 2023). The so-called S-Index is derived from the strength of emission in the cores of the Ca II K and H lines. More information are given about this index in Section 2.2.2. As solar and stellar activities are both monitored using Ca II K observations, we can then compare the solar activity with other sun-like stars activity and decipher the similar mechanisms acting in other magnetically active stars.

Solar Ca II K observations are very crucial in solar physics research. They provide critical insights into the solar magnetic activity and its variability. Continuing to study the solar activity can deepen our understanding of the solar dynamics and its impacts on Earth.

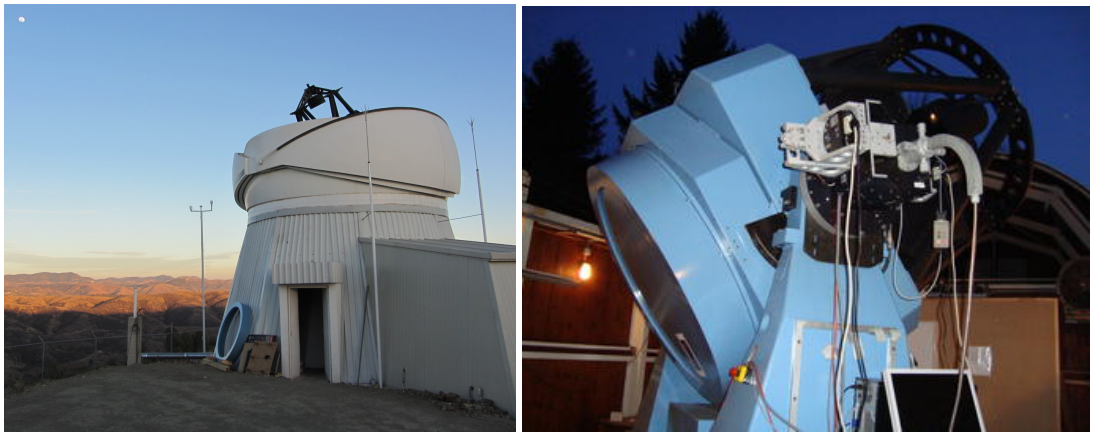

Fig. 2.5. TIGRE at La Luz Observatory, Guanajuato, Mexico. Credit: Hamburg Observatory[2]

2.2 Integrated spectral measurements

2.2.1 TIGRE telescope

TIGRE, Telescopio Internacional de Guanajuato Robotico Espectroscopico, is a fully robotic spectroscopy telescope, located since March 2013 at the La Luz Observatory of the University of Guanajuato, at an altitude of 2400 m above the sea level (see Figure 2.5). The TIGRE project, is run by a collaboration of scientists from three different institutions: the Hamburg Observatory (Germany), the University of Guanajuato (Mexico) and the University of Liège (Belgium). The telescope has a primary mirror with an aperture of 1.2 meters which allows high-resolution spectroscopy (up to R = 20 000) covering a wide spectral range, between 3800 Å and 8800 Å (Schmitt et al. 2014).

One of the main objectives of the TIGRE project is the long-term monitoring of stellar activity. TIGRE is observing a sample of cool stars to investigate their magnetic activity, providing insights into how these cycles are compared to the solar cycle. Although TIGRE is operating during the night, it is also observing the Sun. Indeed, thanks to the light reflected by the Moon, TIGRE can measure the integrated spectrum of the Sun. However, because of the lunar phases, TIGRE observations of the Moon are interrupted for a few days around the New Moon. TIGRE observations are made by measuring the emission in the Ca II K and H lines. The HEROS spectrograph attached to TIGRE offers the possibility to measure the fluxes in the H and K lines as well as in nearby "continuum" windows. The ratio of the fluxes integrated over the lines divided by the fluxes integrated over the continuum windows yields a quantitative measurement of the strength of the lines. This measurement is called the S-Index.

[2] https://hsweb.hs.uni-hamburg.de/projects/TIGRE/DE/hrt_general_info.html

2.2.2 S-index

The S-index is widely used in astrophysics to measure the chromospheric activity of stars, including the Sun. In the 1960s, researchers introduced this index in the context of the HK Project (see Section 1.2.2) at the Mount Wilson Observatory (MWO) and they created the Mount Wilson S-index, further denoted as S_{MWO}. This index is calculated as followed:

$$S_{MWO} = \alpha \left(\frac{N_H + N_K}{N_R + N_V} \right) \tag{2.1}$$

where N_K and N_H quantify the chromospheric emission in the core of the Ca II K and H lines, N_R and N_V correspond to the flux of two bandpasses in nearby continua redwards and bluewards, and α represents a multiplicative factor to calibrate different instruments on the same S-index scale (Vaughan et al. 1978; Duncan et al. 1991). The emission in the core of the Ca II K and H lines are measured with a triangular bandpass of 1 Å and a bandpass of 20 Å for the flux in the nearby continua. As we can see in Figure 2.6, the triangular bandpass around the core of the Ca II K line includes the three main components, K1, K2 and K3. With the legend of 1Å scale, we can visualize approximately how the 2.7Å bandpass of USET looks like and both bandpasses are roughly similar except that the 2.7Å bandpass will include a small additional contribution of the wings coming from the photosphere. The S-index from TIGRE, denoted as S_{TIGRE} is measured identically as S_{MWO} but instead of using a triangular bandpass, it measures the emission with a rectangular bandpass (Figure 2.7). In order to ensure a consistency between measurements of different instruments, calibration is crucial. For instance, S_{TIGRE} is converted to the Mt. Wilson system using a sample of 50 stars with very well known S_{MWO} values (Mittag et al. 2016). The conversion is a well-defined linear transformation:

$$S_{MWO} = (0.0360 \pm 0.0029) + (20.02 \pm 0.42) S_{TIGRE} \tag{2.2}$$

One important issue with TIGRE solar observations is the dependence on the lunar phases. When the Moon approaches its New Moon phase, observations are interrupted for a few days, which has important consequences when we wish to measure modulations by solar rotation as the Carrington period is very close to the duration of the lunar cycle. However, TIGRE has measured the solar S-index continuously since August 2013 and its temporal variation is shown in Figure 2.8, with the S_{TIGRE} values on the left axis and its conversion in the Mt. Wilson scale (S_{MWO}) using Equation (2.2). TIGRE has encountered some issues which led to some gaps in the temporal coverage. Most of them are minor and have hindered the observations during a few hours or a few days but it happened that due to instrumental problems, observations were interrupted for several months. Those gaps are seen around 2016-2017 and 2021. Despite those problems, TIGRE has a total of approximately 1200 days of observations of the solar spectrum reflected by the Moon.

Over the last decades, the S-index has been very useful to identify activity cycles in other stars. Scientists have discovered that the Sun is not unique in exhibiting cyclic variations using

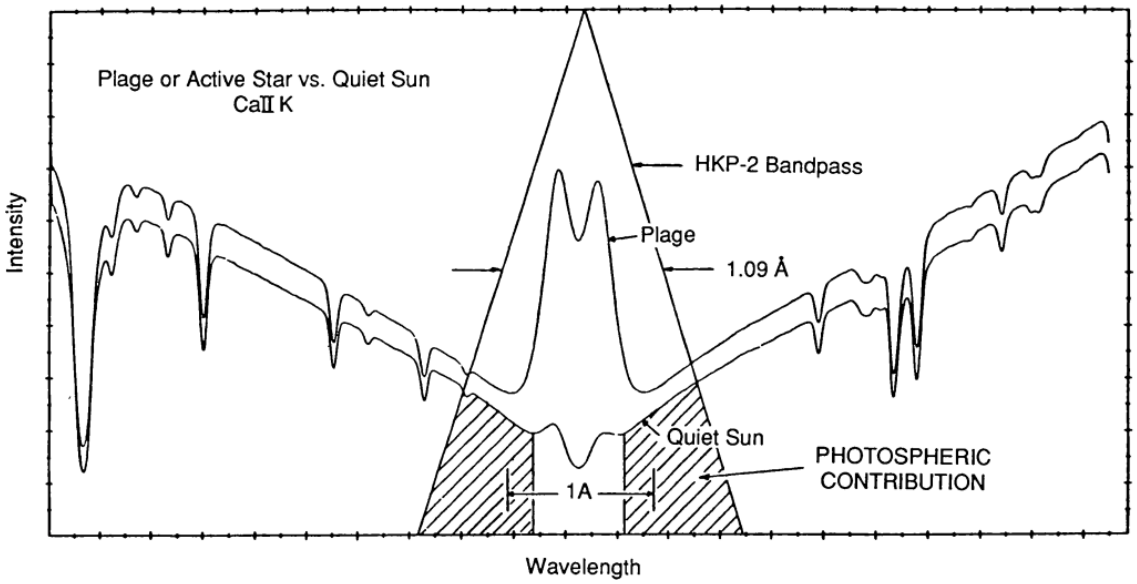

Fig. 2.6. Schematic spectrum around the core of the Ca II K line centered at 3933.67 Å, with plages and quiet Sun emission profiles. The triangular shape indicates the 1 Å bandpass used for the S-index. Image taken from Duncan et al. (1991).

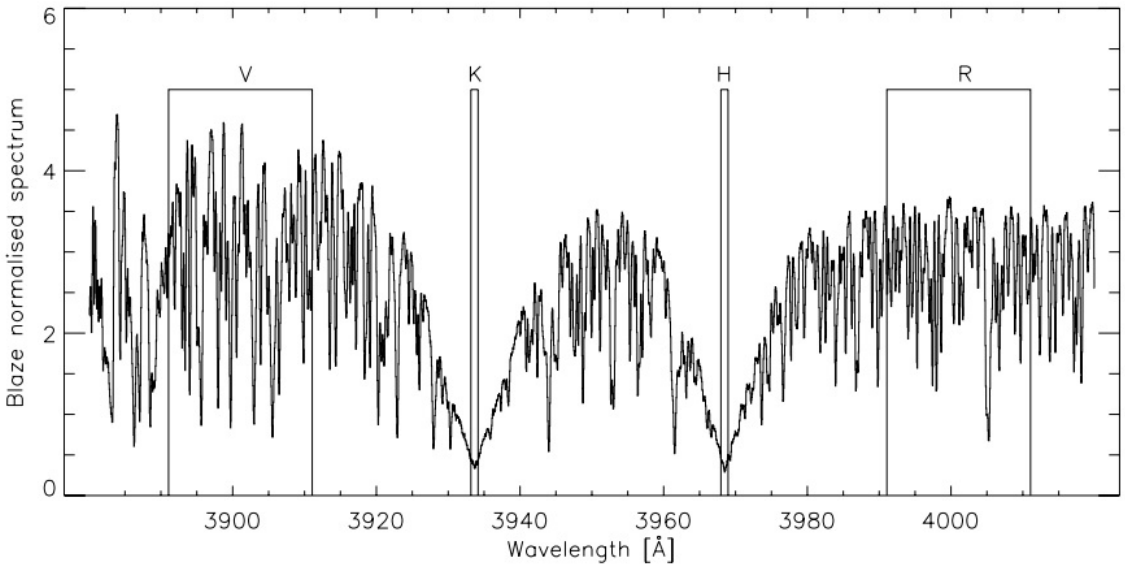

Fig. 2.7. Solar Ca II H & K spectrum as inferred from lunar spectra along with the TIGRE bandpasses used for the S-index calculation (Mittag et al. 2016). The bandwidth is 1 Å in the core of the lines and about 20 Å in the two nearby continua. Bandpasses in the core of the lines are rectangular.

S-index measurements. However, many stars analogous to the Sun display another form of variability, e.g. multi-periodic activity, non-periodic activity, flat activity. Thanks to those studies, we now understand that stellar magnetic activity is dependent on factors such as stellar age, rotation

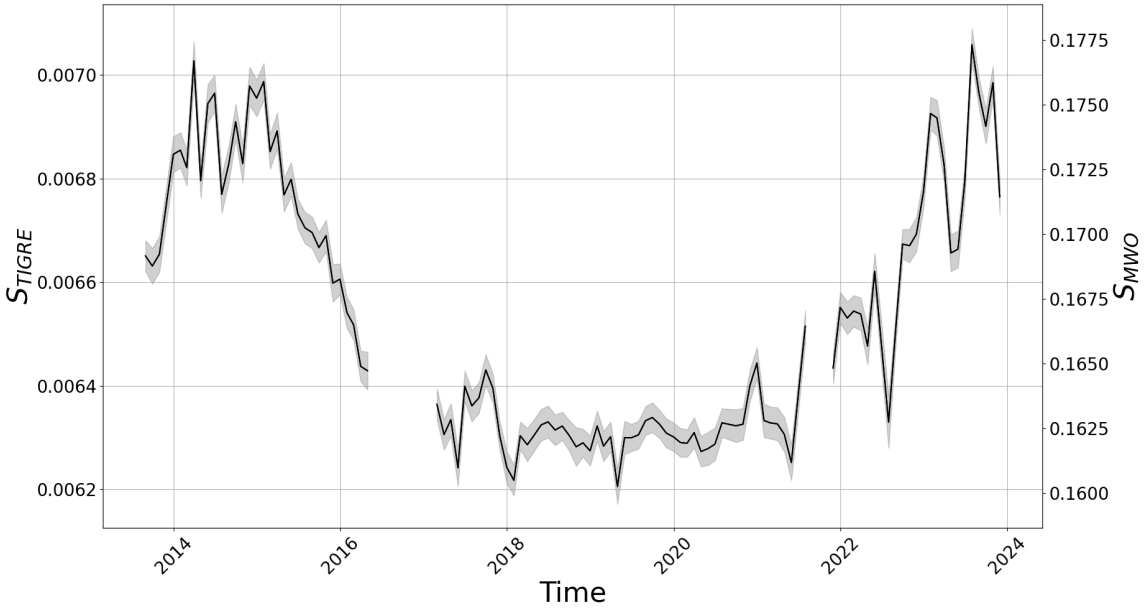

Fig. 2.8. Temporal variation of the solar S-index (monthly averaged values) from TIGRE covering almost a complete solar cycle (from August 2013 to December 2023). Left axis displays the S_{TIGRE} values while the right axis shows them in the Mt. Wilson scale (S_{MWO}) using Equation (2.2). Uncertainties on the data are displayed with grey areas.

rate and spectral type. The S-index plays a significant role in advancing our knowledge of solar and stellar chromospheric activity, enabling the study of stellar activity cycles and the relationship between activity and stellar parameters.

Chapter 3

Data processing

In this Chapter, we will first describe in detail all the different steps performed to extract the meaningful information from the images taken by the USET telescope. Section 3.1 illustrates the data calibration which consists in acquiring the images, centering the solar disk, selecting the highest quality images and correcting the center-to-limb variation. After the images have been properly calibrated, Section 3.2 describes the technical details of the segmentation method of the bright chromospheric structures. And finally, in Section 3.3, we explain how we create synoptic maps of the Sun to reconstruct synthetic images of the Sun as seen under different viewing angles.

3.1 Data calibration

3.1.1 Images acquisition and re-centering

The raw images are saved in FITS files with an in-house image acquisition software. This software allows to adjust the exposure time, the focus of the telescope and to select the best image among a series of 25 buffers acquired in fast cadence. This selection mode helps to choose the image least affected by the atmospheric turbulence. A comment in the header indicates the quality of the observing condition on a numerical scale between 1 and 5. Then the images are automatically processed by a data reduction pipeline. First, the solar limb is detected using an original algorithm combining a Canny edge detection and a threshold associated to morphological operations (Gonzalez et al. 2009). The limb detection works well even in presence of clouds. Then an algorithm estimates the solar disk center, based on an iterative search to find the center of the limb points expressed in polar coordinates. The method is robust even if part of the limb is not present such as on truncated images. Once the disk center is estimated, the image is shifted to have the center in the middle of the image. Finally, meta-data following the SOLARNET standard (Haugan & Fredvik 2020) are added in the header of the FITS file, delivering our level-1 (L1) image series (Bechet & Clette 2002).

3.1.2 Images selection

Ground-based observations suffer a lot from the atmospheric conditions and even more at low altitude. In Brussels, the most important factor that hinders high quality observations stems from the weather conditions. Figure 3.1 shows the total number of days of USET Ca II K observations for each year, with an average of 260 per year. The gaps are essentially due to bad weather. Among the images acquired by USET, not all are scientifically exploitable. There are images whose quality is reduced for a variety of reasons (see examples in Figure 3.2). For each day, we select the one with the highest quality, i.e. the least affected by the criteria described below. This processing of data sorting reduces the final sample to 2725 images.

3.1.2.1 Presence of clouds

Depending on the thickness of the clouds, the chromospheric structures become less and less visible. When plotting the histogram of the intensity in individual pixels within the solar disk, the brightness distribution is a Gaussian, dominated by the inactive areas, the quiet Sun regions, and enhanced on either side due to spots and bright plages, as seen further in Figure 3.10. When clouds affect the image, the histogram is no longer centered in the QS regions and it displays more than one peak. An example of such a case is illustrated in Figure 3.3. Therefore all images with more than one peak in the histogram have been discarded.

3.1.2.2 Cropped images

Due to the Earth rotation, the Sun does not remain at the center of the image. USET automatically follows the trajectory of the Sun in the sky but not with a high precision. Sometimes, part of the Sun falls outside the image area and information about the structures is lost (Figure 3.2b). After the image recentering process, the value of the pixels corresponding to the hidden part of the Sun is set to 0. As a consequence, the detection of zero values within the solar disk is used to remove the cropped images.

3.1.2.3 Light diffusion

Because of meteorological conditions (veils of high altitude, water vapour, dust), the light coming from the Sun is diffused. The structures in the image are less distinct, and the segmentation of these structures becomes inaccurate. An example comparing two observations taken on the same day is illustrated in Figure 3.4. For each image, we computed the ratio of the mean intensity outside of the solar disk over the mean intensity within the solar disk. Then we calculated the standard deviation and removed the outliers, hence the images with a ratio higher than 3σ.

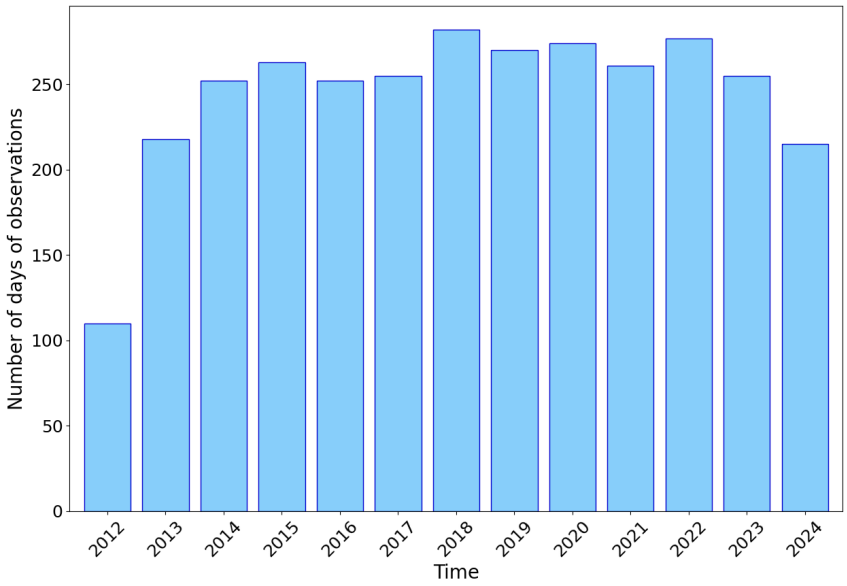

Fig. 3.1. Number of days of Ca II K images collected each year with the USET station.

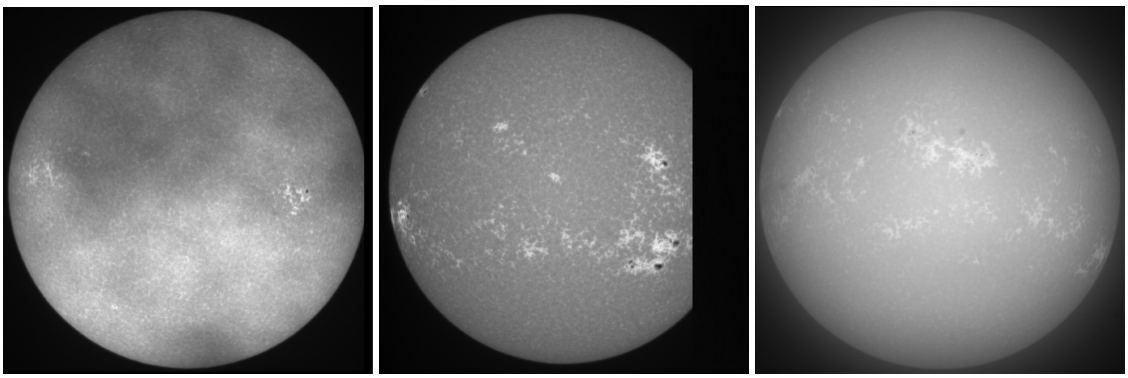

(a) Presence of clouds **(b)** Image cropped **(c)** Light diffusion

Fig. 3.2. Examples of bad quality images from the USET Ca II K observations.

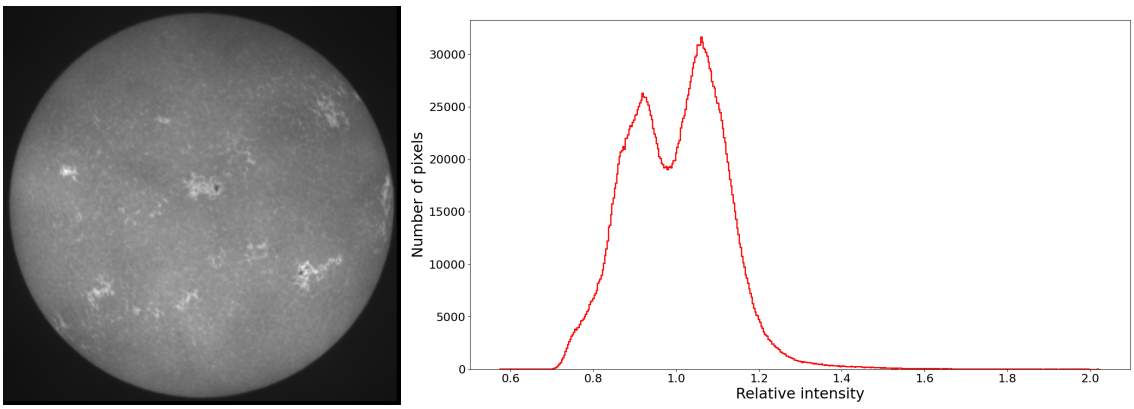

Fig. 3.3. Histogram (right panel) of the pixels intensity on the solar disk for an image affected by clouds (left panel).

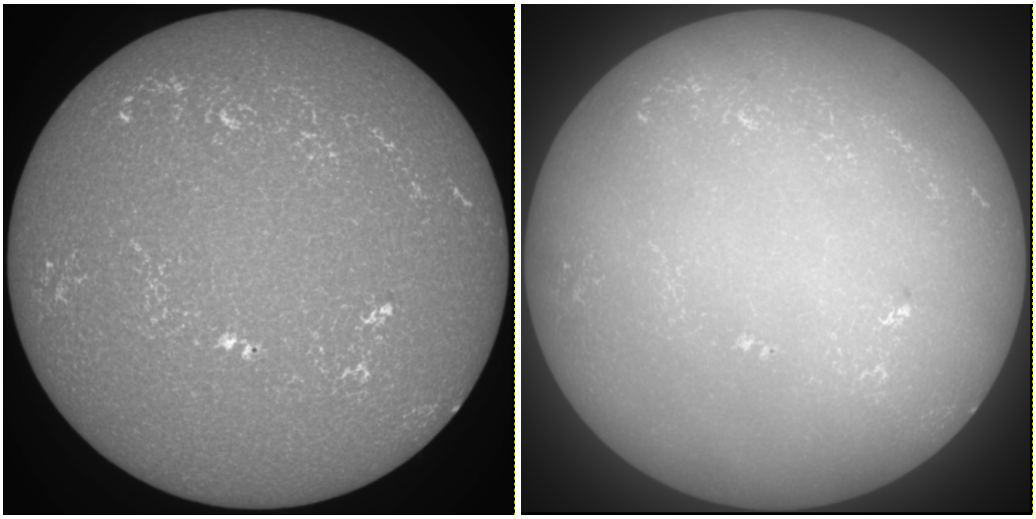

Fig. 3.4. Comparison between two images taken on the same day: one unaffected by the light diffusion (left image) and one affected by it (right image).

3.1.2.4 Atmospheric turbulence

Finally, due to turbulent convection in the Earth's atmosphere caused by the Sun's heating of the ground and buildings, the incoming light is randomly refracted and this has two impacts: spatial smearing and random point-to-point shifts. This perturbation reduces the resolution of the structures on the images, as seen in Figure 3.5.

3.1.3 Center-to-limb variation correction

The center-to-limb variation (CLV) is an optical effect that appears when we are observing the Sun. The light that we receive arises typically at an optical depth of 2/3. This value of the optical depth does not correspond to the same geometrical depth all over the solar disk. It is reached at deeper layers at the center of the disk than near the limb. Therefore, depending on the line of sight, we are looking at different geometrical depths of the solar atmosphere. As we can see in Figure 3.6, an observer looking at the center of the disk can see deeper into the atmosphere, where the gas is hotter, hence brighter. The closer the observer looks towards the limbs, the less he can see into the atmosphere, where the gas is cooler and less luminous. This is called limb darkening. In the solar chromosphere, the situation is different because of the inversion of the vertical temperature gradient (temperature increasing with altitude). However, this layer of the solar atmosphere is very inhomogeneous with temperature and density varying significantly. The contribution of the three components of the Ca II K line (K1, K2 and K3) vary with altitude. Nevertheless, we still observe a limb darkening in the solar chromosphere in the Ca II K line.

This results in a decrease of the intensity from the center to the limb (see Figures 3.7a and 3.7b): brighter at the center and darker close to the limbs. In order to segment the brightest chromospheric structures, it is essential to correct the images for this optical variation. The first step

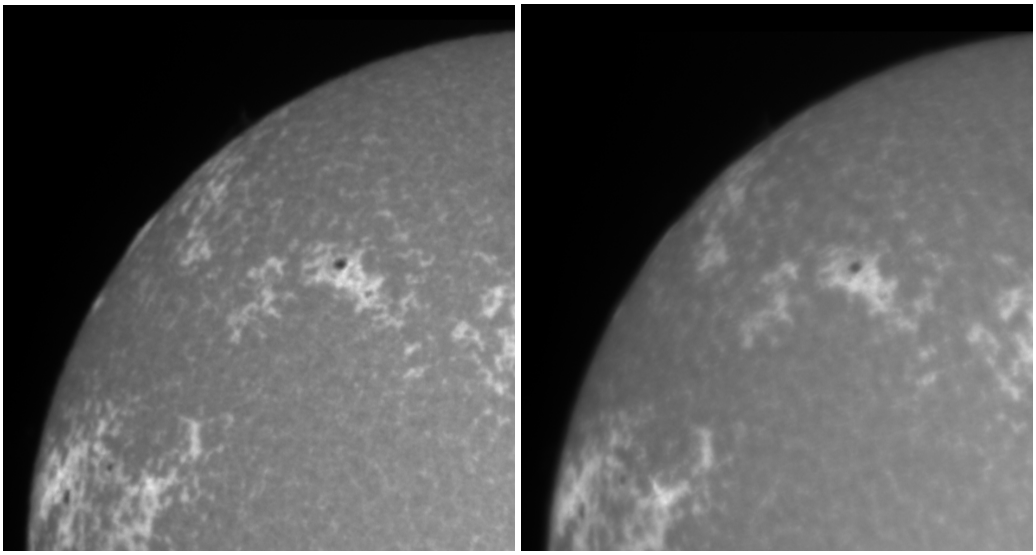

Fig. 3.5. Comparison between two images (zoom on the top left corner) taken on the same day: one slightly affected by the atmospheric turbulence (left image) and one strongly affected by it (right image).

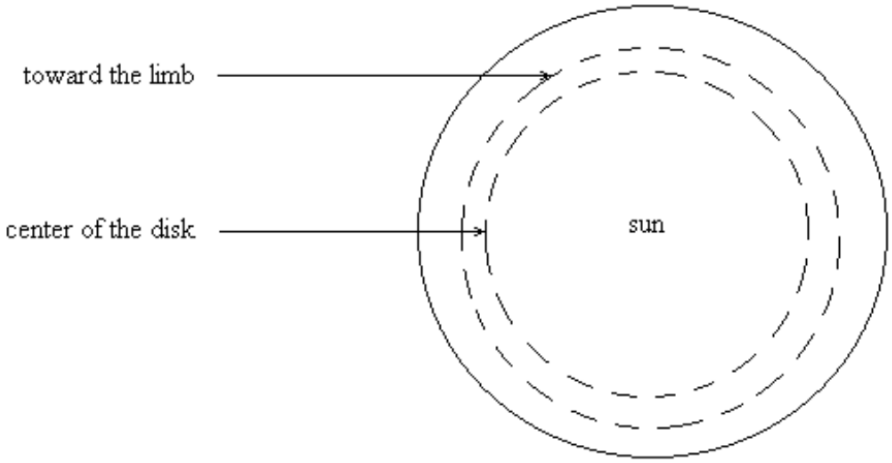

Fig. 3.6. Center-to-limb variation effect. Image taken from Sánchez-Bajo et al. (2002)

consists in using a fifth-order polynomial fitting technique on a series of position angles spanning from 0° to 360°, with a 1° increment. For each angle, the residuals between the intensity profile and the fit are computed. The presence of bright plages leads to an increase in residuals, requiring the identification of the fit with the least residuals to avoid the influence of those structures (Figure 3.7b). Then the fit with the least residuals is used to create a mask that gives an initial approximation of the quiet solar disk (Figure 3.7c). Once the mask is created, the initial matrix is divided by this mask and it gives a first visualization of the corrected image. Based on this first correction, the plages regions are removed using a segmentation method adapted from Chatzistergos et al. (2019) in order to not take them into account in the following steps (Figure 3.7d). When the bright plages

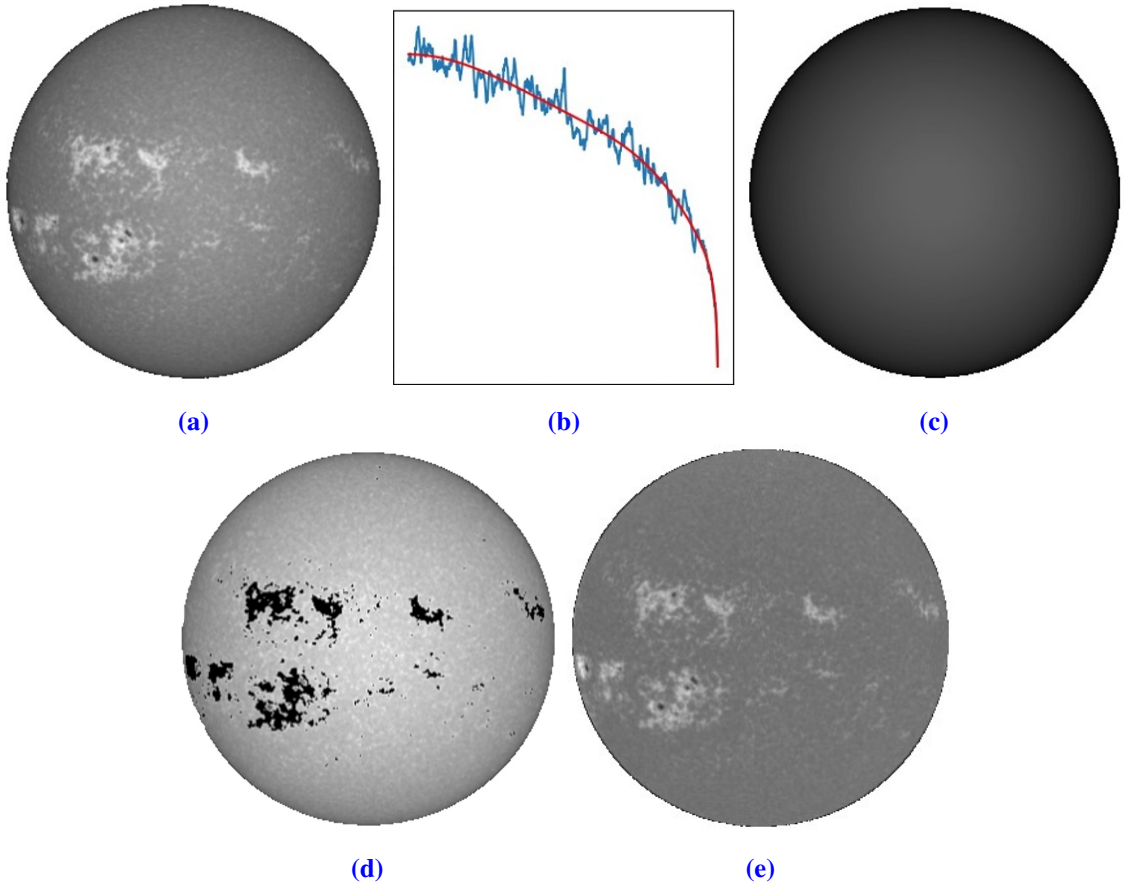

Fig. 3.7. Illustration of the method for correcting the L1 images from the center-to-limb variation. (a) L1 image. (b) Intensity profile from the center to the limb (blue) and fit with the least residuals (red). (c) Mask of the quiet solar disk creation. (d) Plages regions removal. (e) Final corrected image.

are removed, we repeat the step (b) again but instead of calculating the residuals between the fit and the intensity profile, we compute now the mean intensity for each radius of the whole image because the bright plages are no longer present and do not affect the intensity profile. After that, a second mask is created based on this mean intensity profile and finally we divide the initial image by this new mask. Figure 3.7e shows the final result of the corrected image.

3.1.4 Improvements

The calibration process can be improved to be more precise in the selection of the highest quality images. For instance, the algorithm removed the images with opaque clouds hiding some parts of the Sun but it does not detect the images with non-radial inhomogeneities due to the presence of high-altitude veils or transparent clouds. They are almost invisible on the images for us but they may have a significant effect for the CLV correction.

(a) 90th percentile **(b)** 95th percentile **(c)** 98th percentile

Fig. 3.8. Chromospheric structures segmentation using a fixed intensity threshold with an image taken on August 1, 2014. Panel (a) shows the segmented structures with the 90th percentile threshold, panel (b) with the 95th percentile threshold, and panel (c) with the 98th percentile threshold.

3.2 Bright chromospheric structures segmentation

3.2.1 Assessment of the fraction coverage

The main purpose of this work is to study the variation of the observed solar chromospheric activity. Therefore we must segment the brightest structures of the chromosphere: the plages and the enhanced network. As explained in Section 1.1.2.3, plages are bright and extended structures, well visible on the solar chromosphere and the enhanced network, more dispersed and fragmented but equally bright as plages, is believed to correspond to regions of decaying plages (Worden et al. 1998; Singh et al. 2023), dispersing into bright patches close to the extended structures.

3.2.1.1 First method

Our first approach is to use a fixed intensity threshold such as Steinegger et al. (1996); Singh et al. (2012); Priyal et al. (2014). For this, we are working on the "flattened" images, thus normalized relative intensities, after correcting the CLV, ensuring that the same distribution is valid for all pixels on the solar disk. We use the histogram of the intensity in individual pixels of the image representing the distribution of pixel intensities over the entire solar disk. The peak in the histogram corresponds to the most prominent structure in the chromosphere: the quiet Sun, while the tails of the distribution refer to sunspots (lower intensity) and plages (higher intensity). Segmenting the plages and enhanced network is therefore based on the use of an intensity threshold. Taking as a base the distribution of pixels, several intensity thresholds were tried to find the corresponding value: the 90th percentile of the distribution, the 95th percentile and the 98th percentile. An example of the segmented structures for each threshold is illustrated on Figure 3.8. With the 90th percentile, a lot of random isolated pixels all over the solar disk are present on the image segmented. With the 98th percentile, we can clearly see that this threshold is too high because

some part of the plages are not segmented. The 95th percentile seems to correspond better to the threshold for segmenting the plages and enhanced network.

However, this method reveals a weakness in segmenting images when there are few or no structures present on the surface (typically during low activity period). Indeed, the segmentation method shows a strong dependence on the solar activity and gives different results during high activity period than during low activity period (see Figure 3.9). During high activity regime, the segmentation proves reliable but during low activity regime, the method segments much more structures than the plages and enhanced network. Parts of the chromospheric network is included in the segmentation. This is explained by the fact that at low activity, plages are less frequent on the solar disk. Therefore, the distribution in the histogram of the data is less enhanced on the right side compared to that in a high activity regime (see bottom panel of Figure 3.9). In that sense, using a fixed threshold as the 95th percentile, which means keeping the pixels with a value belonging to the top 5% of the largest values in the distribution, is not appropriate for our work. We must then find another method that defines a threshold individually per image.

3.2.1.2 Second method

Our second method is based on the segmentation used by Chatzistergos et al. (2019), a variant of the method presented by Nesme-Ribes et al. (1996) and used by Ermolli et al. (2009). It relies on the determination of the background intensity, the quiet Sun. The identification criterion is then evaluated on objective results from the image analysis. Because plages and sunspots do not appear as distinct peaks in the distribution, it is not an easy task to identify them. First of all, to avoid uncertainties resulting from processing the marginal pixels, we exclusively consider pixels contained within 99% of the solar disk radius. The segmentation method is based on the assumption that the background brightness distribution is Gaussian, dominated by inactive areas, the quiet Sun. The contribution of the other structures, sunspots and plages, is considered to be non-Gaussian in the wings of the distribution (see Figure 3.10). However, the contribution of the sunspots at low values is very tiny due to their small spatial coverage, whilst the one of the bright plages at high values is more significant because of their large spatial extent in the chromosphere. The first calculation consists in determining the value of the quiet Sun brightness, I_{QS}. This structure being the most prevalent structure on the surface, must have an intensity close to the peak of the distribution. So we start by computing the mean intensity, $I_{mean,1}$, and the standard deviation, σ_1, of the distribution inside the solar disk, assuming the threshold for segmenting the plages and enhanced network depends on the intensity dispersion. Then we identify pixels that have an intensity within $I_{mean,1} \pm k\sigma_1$ with a coefficient k varying from 0.5 to 3.0 in steps of 0.1. For each value of k, we compute again the mean intensity of the background $I_{mean,2}$ and the dispersion σ_2 within the interval given by k. The idea is to find the value of k that gives the lowest mean intensity so that $I_{mean,2}$ will not be influenced by the plages and enhanced network. Indeed, those structures, being more present on the solar disk than the sunspots, tend to increase the value of

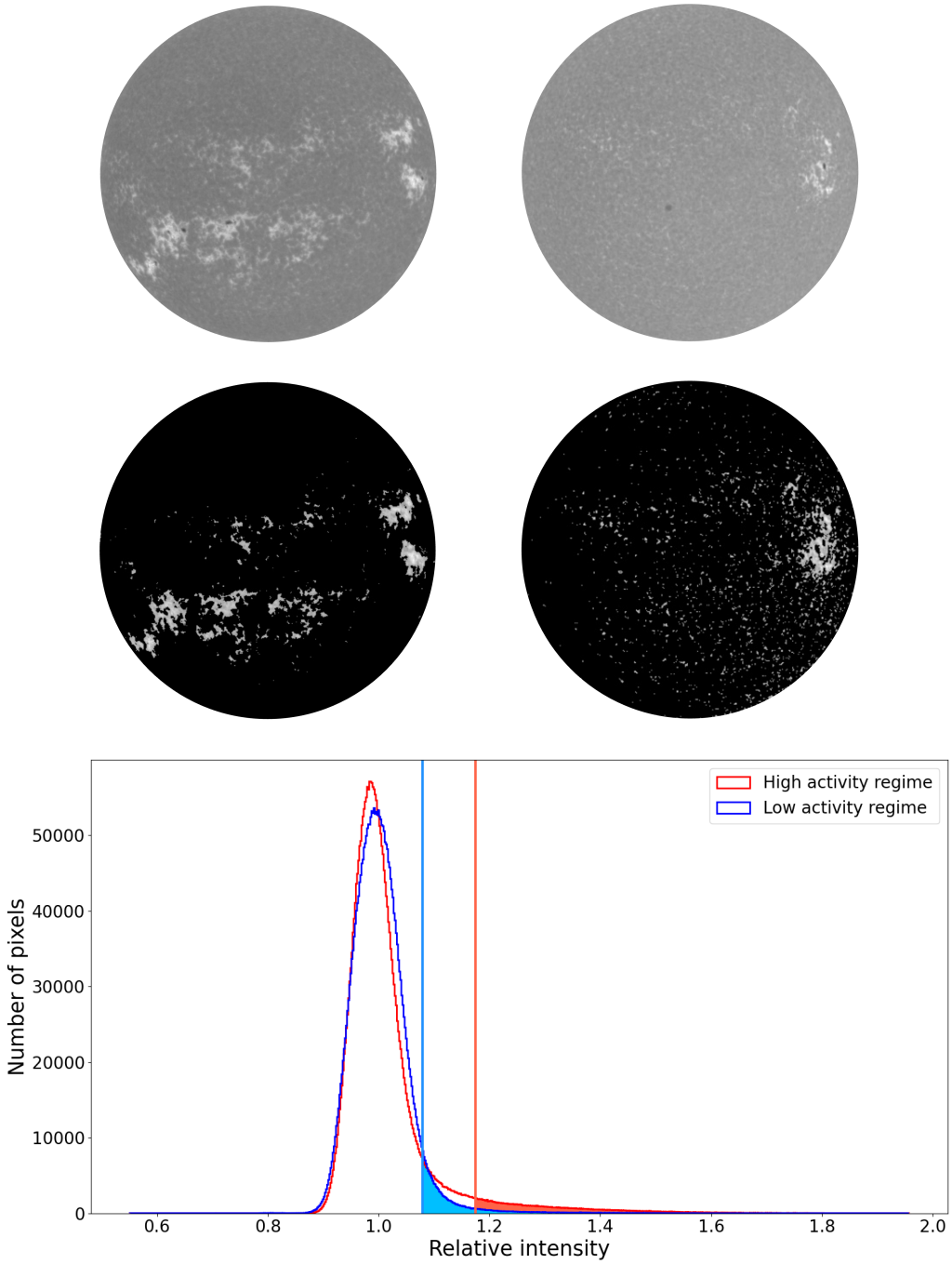

Fig. 3.9. Example of the segmentation during a high activity period on the 1st of August 2014 (left figures) and during a low activity period on the 11th of August 2017 (right figures). The top images display the images corrected for the CLV and the middle images show the segmented structures. The bottom panel illustrates the distribution of the pixels within the solar disk in each case (red for high activity and blue for low activity) with the 95th percentile threshold indicated by the vertical lines. The filled and colored parts of the graph represent the pixels corresponding to the segmented structures of the images right above.

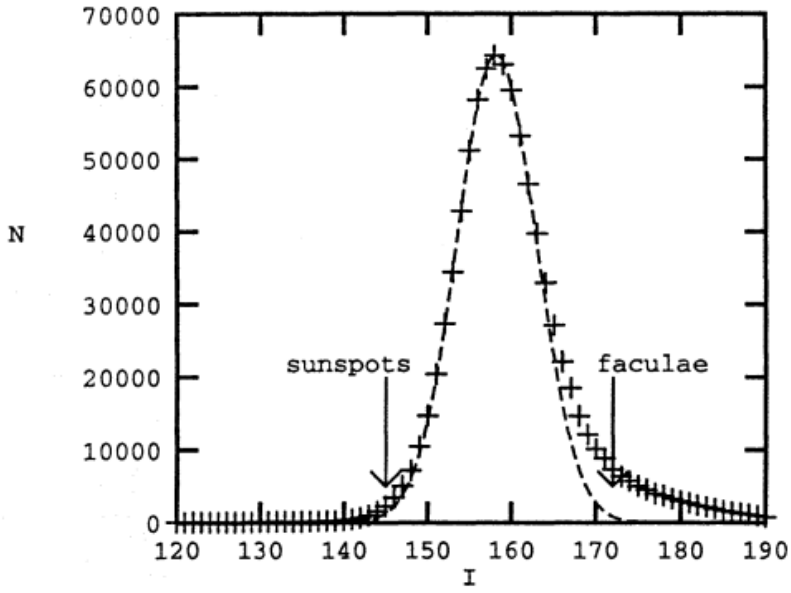

Fig. 3.10. Histogram of the brightness of a spectroheliogram[1]. A gaussian fit was applied to the left part of the distribution (dashed-line). The contribution of the sunspots and the faculae (counterparts of the plages) are illustrated by the arrows. Image taken from Nesme-Ribes et al. (1996).

$I_{mean,2}$. For small values of k, the mean intensity is too close to the initial mean intensity $I_{mean,1}$ and remains higher than the intensity of the background. As k increases, there are more and more pixels with an intensity lower than $I_{mean,1}$ included in the interval, making $I_{mean,2}$ decrease. At a certain point, the plages and enhanced network regions start to contribute more and more to $I_{mean,2}$. Therefore, there must be a value of k that gives a minimum value of the mean intensity, an example is illustrated in Figure 3.11. This value of the minimum intensity, I_{min}, is considered to be the best approximation of the quiet Sun intensity. Finally, to identify plages and enhanced network, we multiply the standard deviation σ_{min} (calculated within the interval defined by the value of k that gives I_{min}) by an empirical factor m_f, and the intensity threshold I_{PEN}, is given by the following equation:

$$I_{PEN} = I_{QS} + m_f.\sigma_{min} \tag{3.1}$$

where I_{PEN} represents the intensity of the plages and enhanced network regions, I_{QS} standing for I_{min}, the intensity of the quiet Sun regions, m_f an empirical multiplicative factor and σ_{min} the dispersion. The value of m_f is a single value applied to all images and was determined to match our results with the one obtained by Chatzistergos et al. 2020 (more explanations further in Section 3.2.1.4). A schematic illustration to determine the plages and enhanced network intensity is displayed in Figure 3.12.

[1] A spectroheliograph is an instrument used to take monochromatic images of the Sun, in a particular wavelength.

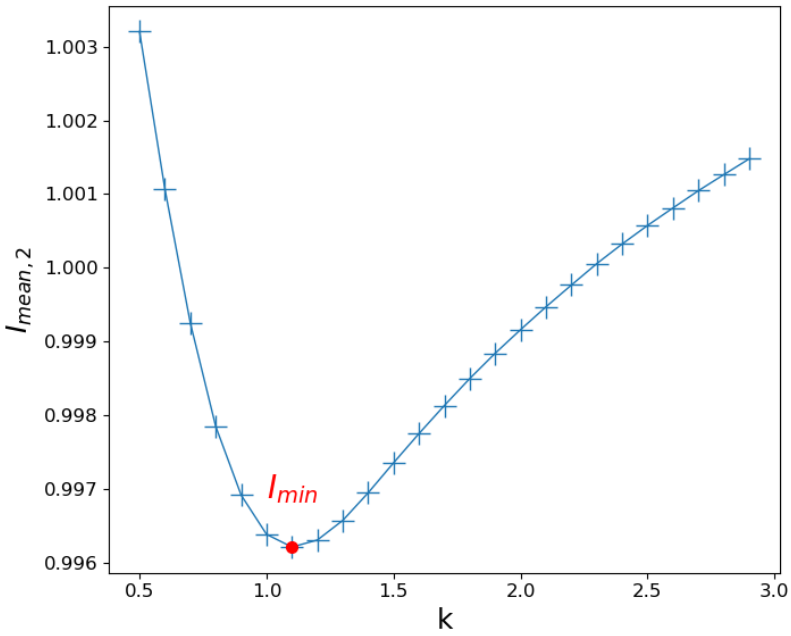

Fig. 3.11. Determination of the quiet Sun intensity. Mean background intensity $I_{mean,2}$ is represented on the y-axis, as a function of k, for an image taken on 15th of April 2015 with USET. The minimal value of the intensity I_{min}, is used to best represent the quiet Sun intensity.

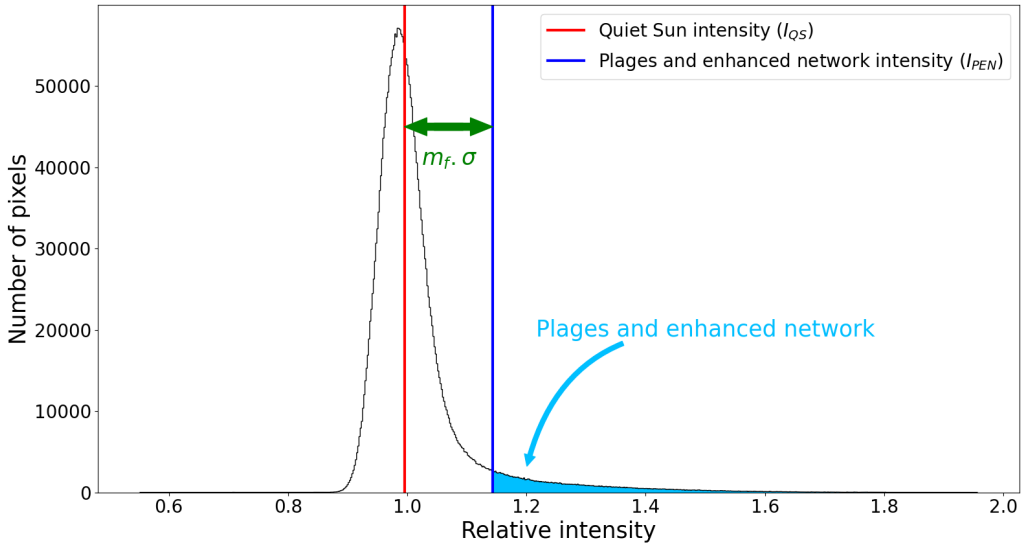

Fig. 3.12. Schematic illustration of the plages and enhanced network intensity determination, on the pixels distribution histogram. The red vertical line represent the intensity of the quiet Sun I_{QS}, found with I_{min}. The blue vertical line marks the intensity threshold for the plages and enhanced network I_{PEN}, determined by using Equation (3.1) that adds the standard deviation σ multiplied by a empirical factor m_f, to I_{QS}. This addition is illustrated by the horizontal green arrow. The light blue area indicates the pixels corresponding to the plages and enhanced network regions.

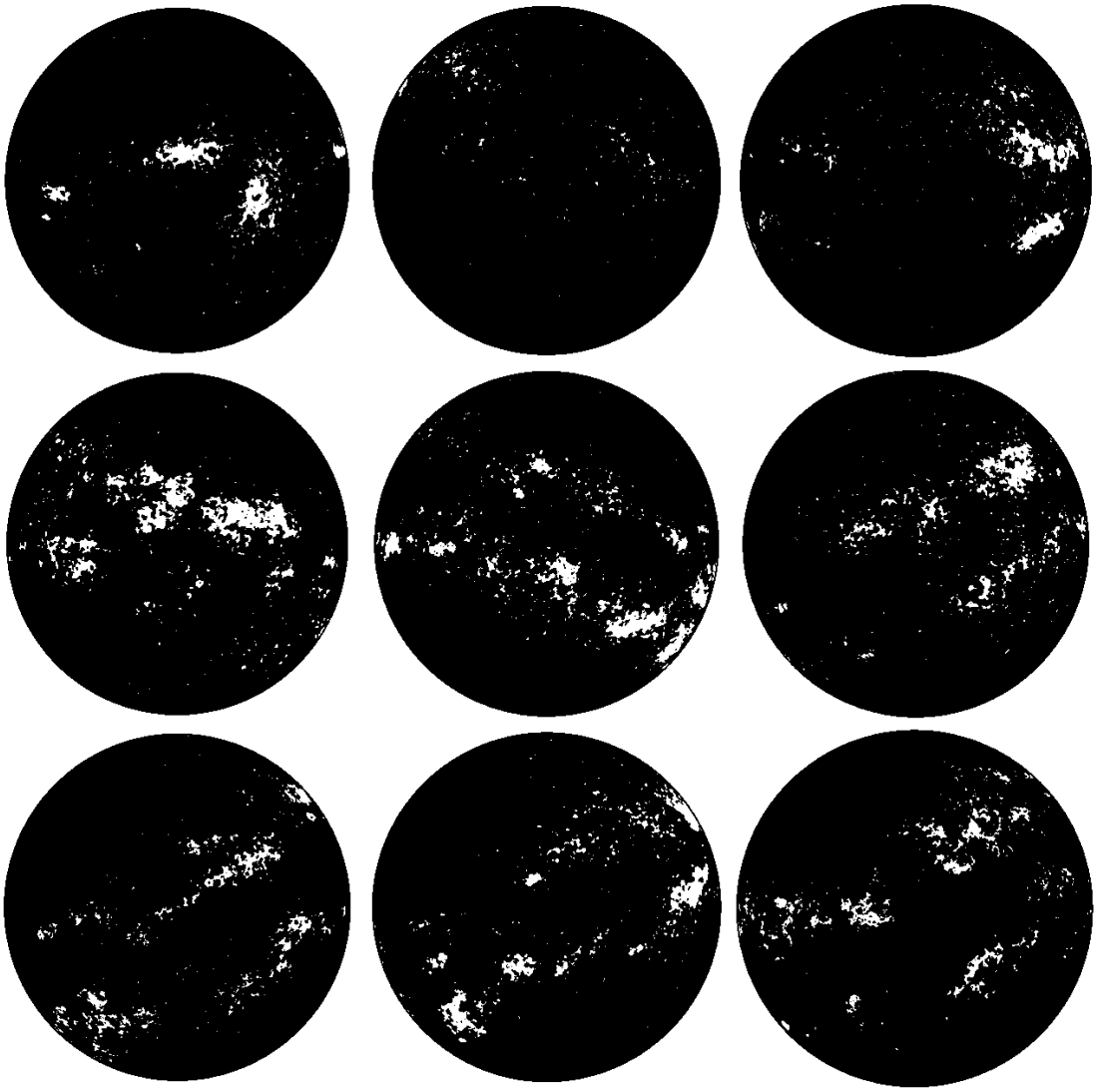

Fig. 3.13. Examples of plages and enhanced network segmentation with USET Ca II K images.

By fixing the pixels with a value below this threshold to zero and the one above the threshold to 1, we get a mask for each image separately. Figure 3.13 displays several examples of the produced masks using the segmentation method described above. These masks are used to compute the area of each identified plages and enhanced network regions on the solar disk.

3.2.1.3 Fraction coverage evaluation

Once the brightest structures are segmented, in order to obtain an index of the chromospheric activity, we compute the fraction of the solar disk covered by the plages and enhanced network, which is referred to as "area fraction" or "fraction coverage" for the rest of the manuscript and denoted as A_{PEN}. It corresponds to the ratio of the number of pixels identified as plages and enhanced network to that of the whole solar disk. Figure 3.14 shows the daily, monthly and monthly smoothed temporal variation of the plages and enhanced network area fraction, A_{PEN}.

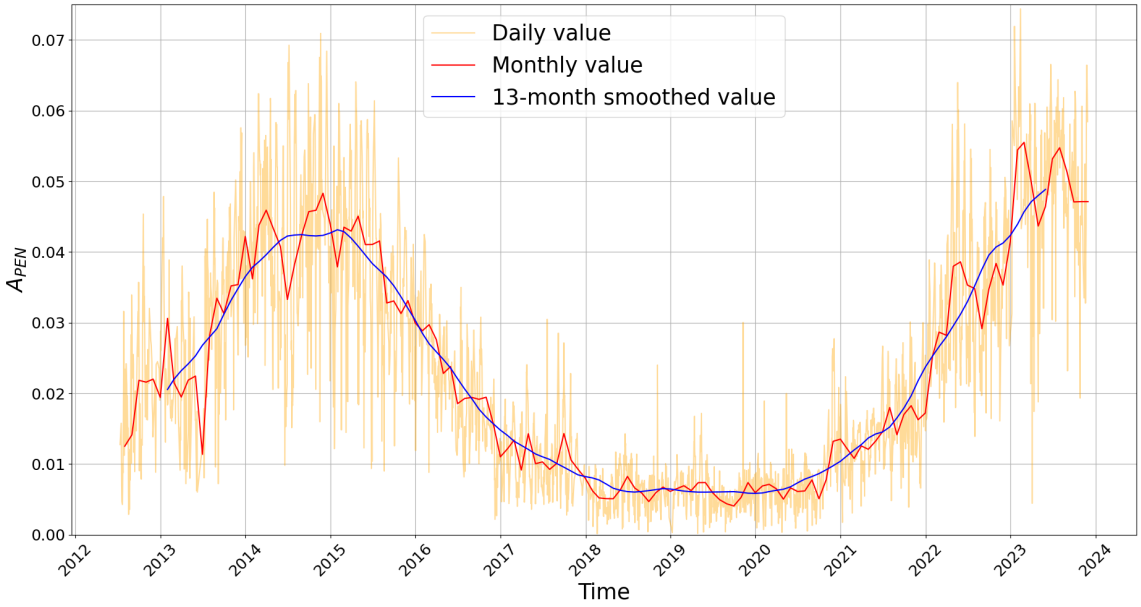

Fig. 3.14. Temporal variation of the fraction of the solar disk covered by plages and enhanced network, A_{PEN}. Daily values are displayed in orange, monthly values in red and 13-month smoothed values in blue.

The monthly smoothed values is derived by a running mean of monthly values over 13 months centered on the corresponding month. There are no smoothed values for the first 6 months and last 6 months of the data series.

First of all, as the plages and enhanced network are manifestions of the magnetic activity in the chromosphere, the variation due to the solar cycle is obvious.

Secondly, it may not be evident at first glance, but if we look closely at the monthly values around 2013, we may observe a change in the trend of the variation: the area fraction shows a sharp dip. We found that in July 2013, an additional neutral density filter was installed on the telescope (see Section 2.1.1) and this reduced the overall light intensity entering the telescope. Consequently, it increases the exposure time as we can see in Figure 3.15). From here on, we will not use the data before the date of the installation of the neutral filter.

3.2.1.4 Time series validation

To validate our segmentation method, we used two different ways: the first one is matching our time series with the one obtained by Chatzistergos et al. (2020) to determine the multiplicative factor of Equation (3.1). The second one is comparing it with other magnetic activity indices, such as the sunspot number, the sunspot area and the solar radio flux at 10.7 cm, which are indices measuring the magnetic activity of the Sun in other wavelengths.

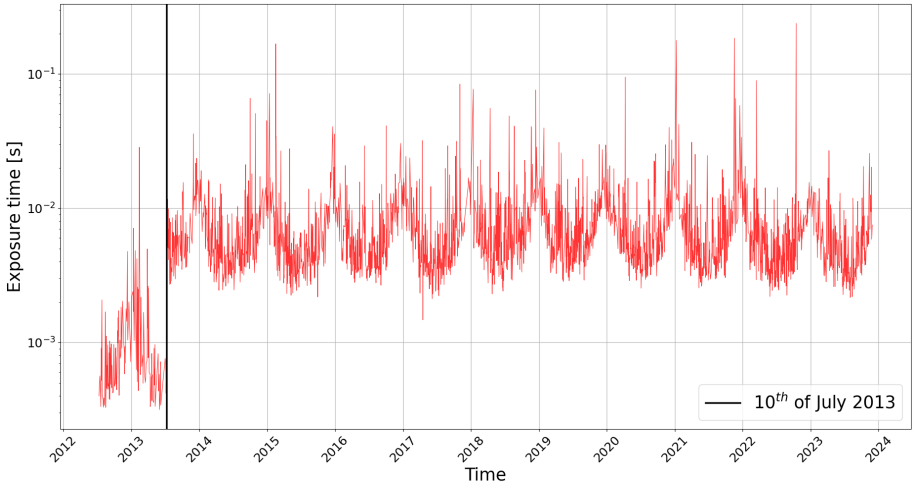

Fig. 3.15. Temporal variation of the exposure time. The data shown are daily values and the black vertical line represents the date when the additional filter was installed on the telescope.

Comparison with another Ca II K time series The method explained in Chatzistergos et al. (2019) was used to segment exclusively the plages regions. In our case, we have included the enhanced network in our segmentation. As the method used in this work is based on their method, the comparison of our results with theirs is useful to determine the empirical multiplicative factor m_f used in Equation (3.1) in order to define the intensity threshold for segmenting the plages and enhanced network. To compare our results with those obtained by Chatzistergos et al. (2020), we must remove the enhanced network from our time series. As explained in Section 1.1.2.3, the enhanced network is part of the chromospheric network, the web-like pattern seen on the right picture of Figure 2.4. This structure is the counterpart of the supergranulation (Simon & Leighton 1964; Stix 2004), visible at the solar surface as a cellular pattern and manifesting itself indirectly in the chromospheric network. Therefore, if we want to segment only the plages, we must get rid of all the structures that have an area below the area of the supergranulation. The size of the supergranulation is not easy to determine and depends strongly on the procedure used in the data processing. Over many decades, several studies have been conducted, and they found the diameter of the supergranulation varying between 12 Mm and 35 Mm (Simon & Leighton 1964; Brune & Woehl 1982; Hagenaar et al. 1997; De Rosa & Toomre 2004). More recent studies have increased the precision of the size and the diameter converges to a value of 27 Mm (Del Moro et al. 2004; Hirzberger et al. 2008; Chatterjee et al. 2017). Therefore, by converting the value of 27 Mm into pixels of our USET images and using the connected components method, we can remove the connected components with an area smaller than the size of the supergranulation. In this case, we are left with a segmentation of plages only. An example of the difference before and after the area threshold is seen on Figure 3.16.

Thanks to the kindness of Dr. Theodosios Chatzistergos, who provided us with his segmentation results using USET data, we can compare our results. He applied the segmentation

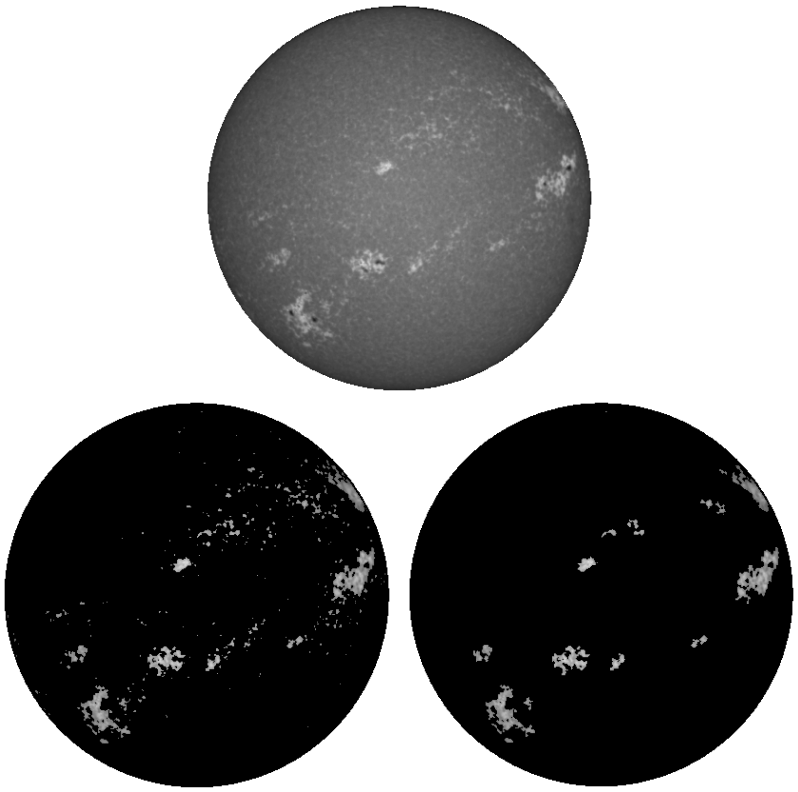

Fig. 3.16. Segmentation before and after the area threshold. Top image: Solar full-disk image from the 29th of October 2013. Bottom images: Results of the segmentation with and without the enhanced network. Left panel: Plages and enhanced network. Right panel: Plages only.

method presented in Chatzistergos et al. (2020) to the same dataset used in our work (USET Ca II K images) and over the same time interval. Their method was designed to ensure that, when applied to the Rome/PSPT data, the resulting plage values replicate those from the SRPM (Solar Radiation Physical Modeling, Fontenla et al. 2009) and a multiplicative factor of 8.5 was found (Chatzistergos et al. 2019). Figure 3.17 shows the comparison between the plages areas time series of Chatzistergos et al. (2020) and our time series for diverse values of the multiplicative factor m_f. An analysis of the residuals confirmed that the value of $m_f = 3.9$ provides the best correlation between the two time series.

Comparison with other magnetic activity indices The magnetic activity of the Sun is observable in other wavelengths analysing the activity from different layers in the solar atmosphere. The International Sunspot Number (ISN) is the most commonly used index to measure the solar activity. It is determined by counting the number of sunspots in the solar photosphere. Several studies have found a linear relationship between the Ca II K plages area and the ISN for yearly, monthly and daily values (Kuriyan et al. 1982; Foukal 1996; Bertello et al. 2016; Priyal et al. 2017; Singh et al. 2021). Moreover, some of them, in addition with other studies (Mandal et al. 2017; Chapman et al. 2011), have demonstrated that the sunspot area is also linearly correlated with the plages area.

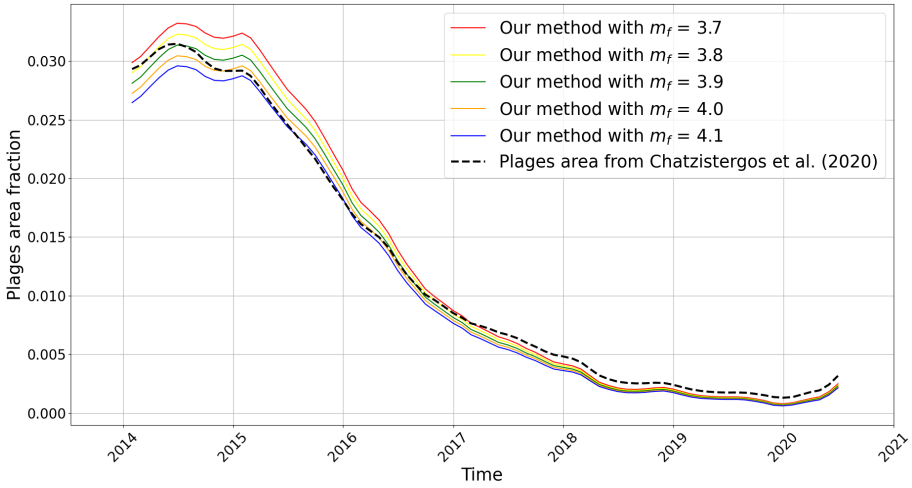

Fig. 3.17. Comparison between plages fraction coverage obtained with our segmentation method and another time series of plages fraction coverage for the same dataset. Black dashed line represents the plages fraction coverage from Chatzistergos et al. (2020) and the different colored lines stand for our plages fraction coverage with different values of the multiplicative factor m_f. Data plotted are 13-month smoothed value.

However Chapman et al. (1997); Tlatov et al. (2009); Chatzistergos et al. (2022) found different results and have shown that a quadratic or a power-law function best represents the relationship between plages area and sunspots area, except for annual values. But Chatzistergos et al. (2022) pointed the fact that the relationship depend on the bandwidth used and the strength of the solar cycle analysed.

The solar F10.7cm radio flux (Tapping & Morton 2013), called F10.7 index, is a widely used long-term index of solar activity. It measures the radio emissions in the decimetric range originating high in the chromosphere and low in the corona. For this comparison, we used the F10.7cm data series from the National Research Council Canada Dominion Radio Astrophysical Observatory in Penticton, British Columbia, available through NOAA[2], Space Weather Prediction Center (SWPC). Recently, Clette (2021) found a fully linear relationship between F10.7 index and the ISN. For monthly and yearly averaged values, the linearity is found for values of ISN above 30-50. Below that, the relation becomes non-linear and the best fit is given by a 4th degree polynomial.

By retrieving data of those indices, we have compared our results to study the correlation with the plages area fraction. As illustrated in Figure 3.18, we show the correlation between the plages area fraction and the ISN (left column), the sunspots area (middle column) and the F10.7 index (right column). Top panels display daily values, while middle and bottom panels show monthly and yearly values, respectively. For each panel, we overplotted two types of fit: a linear regression (red curve) and a 2nd degree polynomial (blue curve). We used an orthogonal distance

[2]https://www.ngdc.noaa.gov/stp/space-weather/solar-data/solar-features/solar-radio/noontime-flux/penticton/

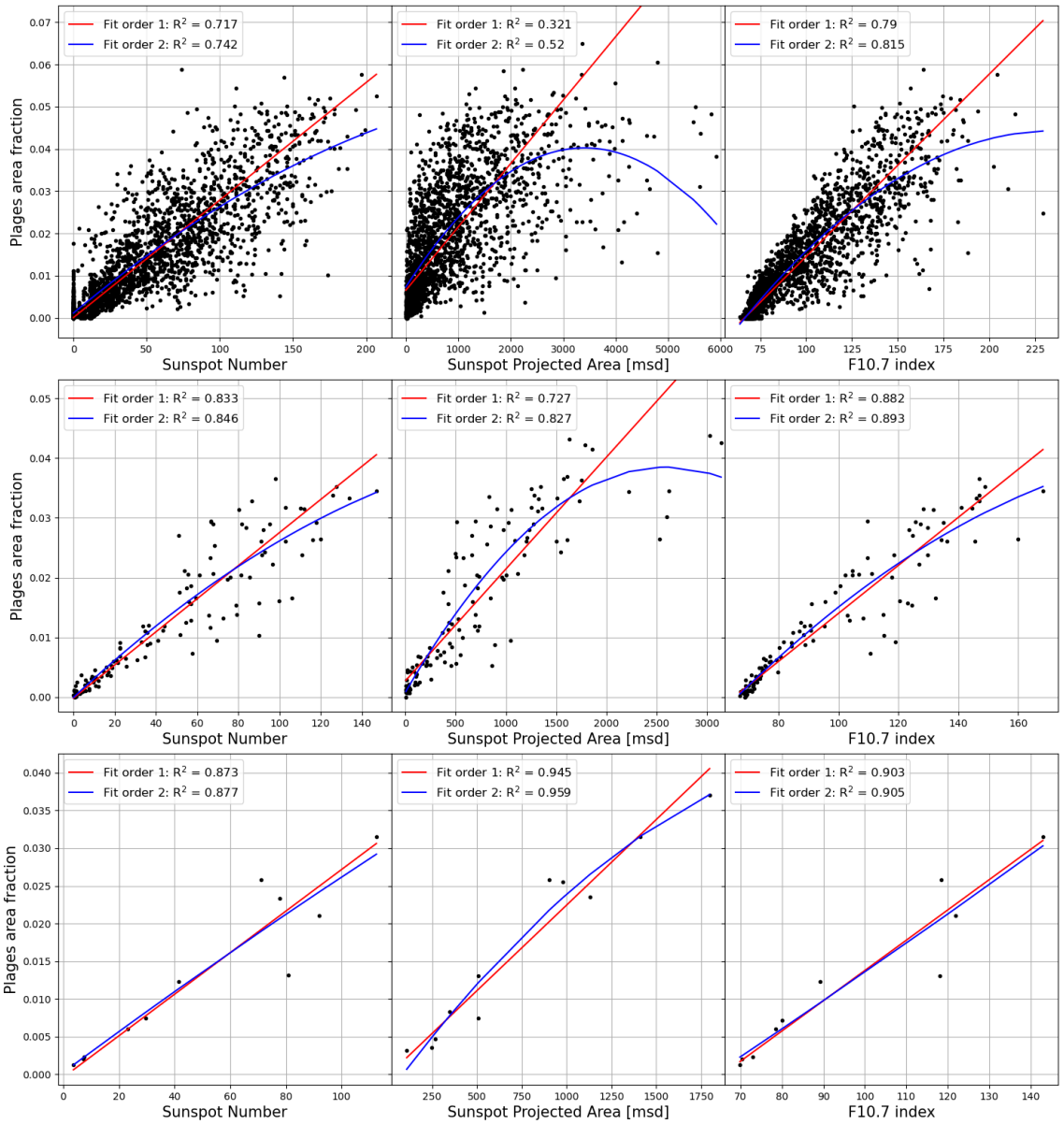

Fig. 3.18. Scatter plots between plages area fraction and the ISN (left column) from SILSO[3] (Clette & Lefèvre 2016), the sunspots area (middle column) obtained from the sunspots drawings database of USET[4], and the F10.7cm radio flux (right column) available through NOAA[5]. Top plots show daily values, while the middle and bottom plots show monthly and yearly values, respectively. Two different fits are overplotted, a linear (red) and a quadratic (blue). For each fit, the coefficient of determination was calculated and is indicated in the top left corner of the panels.

regression technique and calculated the coefficient of determination for each fit, R^2, which is indicated in the top left corner of the panels.

[3] https://www.sidc.be/SILSO/home

[4] https://www.sidc.be/uset/

[5] https://www.ngdc.noaa.gov/stp/space-weather/solar-data/solar-features/solar-radio/noontime-flux/penticton/

For the correlation with the International Sunspot Number (ISN), the daily, monthly and yearly data are well fitted by the linear regression. For each of them, R^2 is quite high and the 2nd degree polynomial fit doesn't give a significantly higher value than the linear fit. This is in close agreement with the results of the studies listed above. However, the fair correlation between those indices is only true for long time scales (> 2-3 months). As they are sensitive respectively to photospheric and chromospheric phenomena, there are rather large discrepancies over shorter time scales.

Regarding the correlation with sunspot area, daily values display a huge scatter. Neither the linear nor the second-order polynomial fits provide significant results. Their coefficient of determination is very low, indicating that they do not adequately represent the relationship between the variables. Similar to the ISN, sunspot areas are sensitive to photospheric phenomena, which leads to significant discrepancies on daily time scales. However, for the monthly data, the R^2 for the quadratic fit is higher than that of the linear regression, suggesting that the relationship between plages area fraction and sunspot area follows a polynomial of order 2 function for the monthly data. In contrast, the linear model fits well the yearly data. Since most studies do not converge towards confirming whether the relationship is linear or quadratic (see Table 1. of Chatzistergos et al. 2022), we cannot draw a conclusion about the nature of the relationship between plages area and sunspot area.

Finally, as Clette (2021) found a linear relationship between the ISN and the F10.7 index, and as the correlation between the plages area and the ISN is linear, we expect to find a linear correlation also between the plages area and the F10.7 index. Indeed, for daily, monthly and yearly values, the coefficient of determination for the linear fit is quite high and not so much different from the one for the 2nd-order polynomial fit. However, as point out by Clette (2021), in the monthly data, the low values are not well fitted by the linear regression and would be better modeled with a polynomial of order 2 or more.

In conclusion, after comparing our results with another Ca II K time series of plages area fraction (assessed using the same data sources), ensuring consistency and reliability of our time series, we cross-checked our results against three other magnetic activity indices to guarantee that they are consistent with well-established patterns in solar activity. This validation process confirms the robustness of our data and its reliability in representing solar magnetic activity.

3.2.2 Uncertainties on the data

The uncertainties on the time series of the area fraction of plages and enhanced network is determined based on the entire dataset from the USET Ca II K images available at the ROB. The entire dataset contains approximately 23 000 images since July 2012. We want to assess the uncertainties related to the segmentation process so we only removed the images that were affected by the presence of clouds, as well as the cropped images. The segmentation of these images would be skewed by these factors.

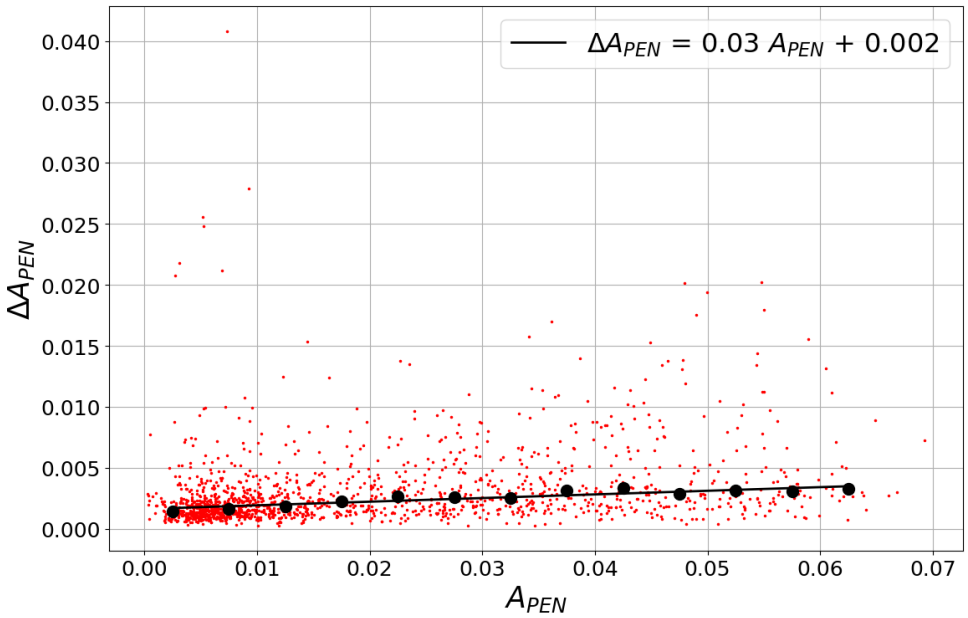

Fig. 3.19. Uncertainties ΔA_{PEN} on the area fraction of plages and enhanced network. The full dataset of area fraction is shown in red. The black dots represent the mean values of the area fraction per bins of 0.005 and the black line corresponds to the linear fit computed on these data, with the linear fit equation indicated in the upper right part of the panel.

The method of the uncertainties computation consists in first keeping the days that have at least 4 observations and running our segmentation method on all the remaining images. Then we calculate the mean value and the standard deviation of the plages and enhanced network area fraction per day. After that, an outliers removal method identifies and removes data that deviate significantly (3σ) from the rest of the data. Finally, the standard deviation for each day is recalculated and is taken as the error per day. We have plotted the errors ΔA_{PEN}, as a function of the area fraction A_{PEN}, for all the analysed data, in Figure 3.19. Data with a very high uncertainty might correspond to observations presenting non-radial inhomogeneities, not being removed by our calibration process and not being taken into account in the center-to-limb variation correction process. To perform a linear regression, we first have grouped the data into bins of 0.005 area fraction and plotted the mean values of ΔA_{PEN} as a function of A_{PEN} (black dots in Figure 3.19). Then we used an orthogonal distance regression technique to fit linearly the mean values and we found a coefficient of determination $R^2 = 0.83$. Therefore, we obtain a linear equation that defines an error depending linearly on the area fraction:

$$\Delta A_{PEN} = 0.030 A_{PEN} + 0.002 \tag{3.2}$$

3.3 The Sun viewed under different inclinations

During our work, we also aim at a better understanding of the magnetic activity of stars based on our dataset of solar observations. Since chromospheric observations in the Ca II lines are crucial to study the stellar magnetic activity, our results can be used as a Rosetta stone to decipher the similar mechanisms acting in other magnetically-active Sun-like stars. As the magnetic structures are distributed between mid-latitude and the Equator, and as the stars are observed under unknown inclinations, we suspect an effect of the inclination of the rotation axis on the observable chromospheric emission. It is therefore essential to assess the influence of the viewing angle on the magnetic activity to compare solar variability with that observed in other solar-type stars. For this, we exploit the archives of Ca II K images from USET since July 2012, and we reproduce solar masks from any inclination by constructing segmented synoptic maps that plot the entire solar surface during a full solar rotation. Hereafter are the steps to accomplish this work.

3.3.1 Solar images projection

To map the entire solar surface, we must project the spherical coordinates onto a two-dimensional plane, in Cartesian coordinates. Many options are available to do so depending on the purpose of the work. For our work, we have chosen the simplicity of the Plate Carrée (CAR) projection, which is an equidistant cylindrical projection. The CAR projection maps spherical coordinates (longitude, latitude) in Cartesian coordinates with the x-axis representing the longitudes and the y-axis the latitudes. The resulting map is a grid of perfect squares from East to West and from North to South with meridians and parallels equally spaced. However, this projection suffers from distortions, particularly far from the Equator. Close to the Poles, the areas of structures appear larger than they are in reality. However, as plages are distributed close to the Equator, this projection gives an accurate scale at those latitudes. The association of the heliographic positions of a magnetic structure to its position in pixels on the map is especially easy (Calabretta & Greisen 2002). An example of this projection is shown in Figure 3.20. The white part of the projected image (here in the top part) results from the tilt of the Sun's rotation axis relative to the ecliptic, ranging from $-7.25°$ to $7.25°$, and corresponds to the part of the solar hemisphere that is not visible from the Earth. Therefore, except when this angle is $0°$, there will always be a small region near the North or South Pole that remains hidden. These parts of the image are filled with zero values.

3.3.2 Synoptic map creation

The first method we implemented to map the entire solar surface during a full solar rotation, involves using the same width for each meridional slice extracted from the 2D-projected images, and then juxtaposing them without overlap to create the map. As the Sun is rotating $360°$ during ~ 27.27 days, an easy calculation gives the number of degrees performed by the Sun during one

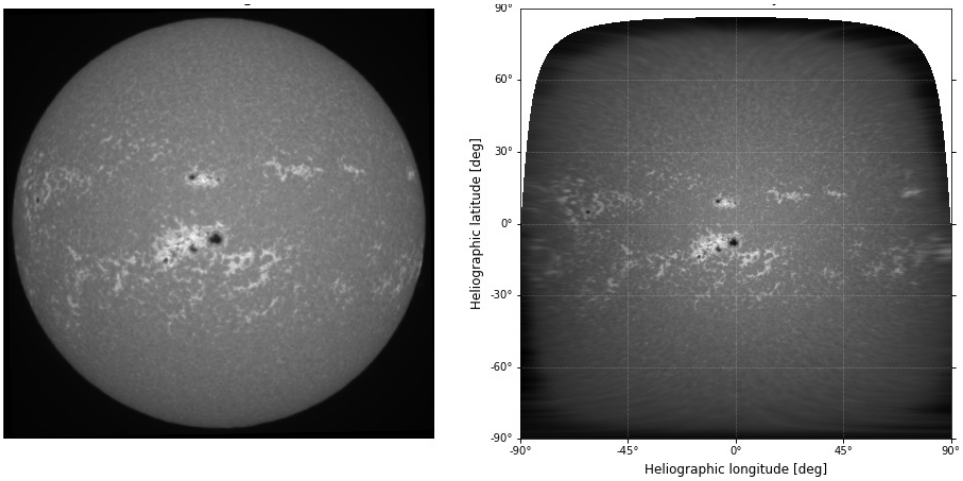

Fig. 3.20. Illustration of the projection of a solar image using the Plate Carrée projection. Left image: L1 solar image. Right image: Projected image (with CAR projection). Spherical coordinates are converted in pixels coordinates and the projection form a grid of squares with equal spaces between the meridians and parallels.

day. Then by converting the number of degrees in pixels (knowing that the image contains 2048 × 2048 pixels and represents a solar hemisphere, thus a range in longitude of 180° corresponding to half of the solar rotation), we can easily define a daily pixels width around the center of the image. However this method will be correct if the observations are taken at the exact same time each day and if we have 365 days of observations per year, which is not the case in our dataset.

To achieve this efficiently, we need a method that considers the number of observation days and the time when the observation was done. In that way, we can adapt the width of the meridional slice to the non-uniform time intervals between images, to ensure a complete filling of the map without gaps. For this, we use the apparent Carrington longitude of the central meridian of the image. Let us consider an example: we want to produce a synoptic map around the date of the image, called I_i. By knowing the central meridian longitude of I_i and the one of the image before, I_{i-1} and after I_{i+1}, we can determine the pixels width for the image I_i. Then we repeat the same process for the other images until we have 180° on the left side of the central meridian of I_i and 180° on the right side of the central meridian of I_i. An illustration of this construction is presented in Figure 3.21. In that way, the width of pixels will be larger if there is not observation on the previous or next day. For example, on this figure, the width of pixels for the image on July 7 is wider because there were no observations between the 7th of July and the 13th of July. Here we have shown a synoptic map plotting the entire solar surface during one full solar rotation but we can construct synoptic maps over as many solar rotations as we want, just by specifying the number of degrees on each side of the central part of the map. Synoptic maps over seven solar rotations were analysed in Chapter 4 in order to study the detection of modulations due to the solar rotation (see appendices of the paper in Section 4).

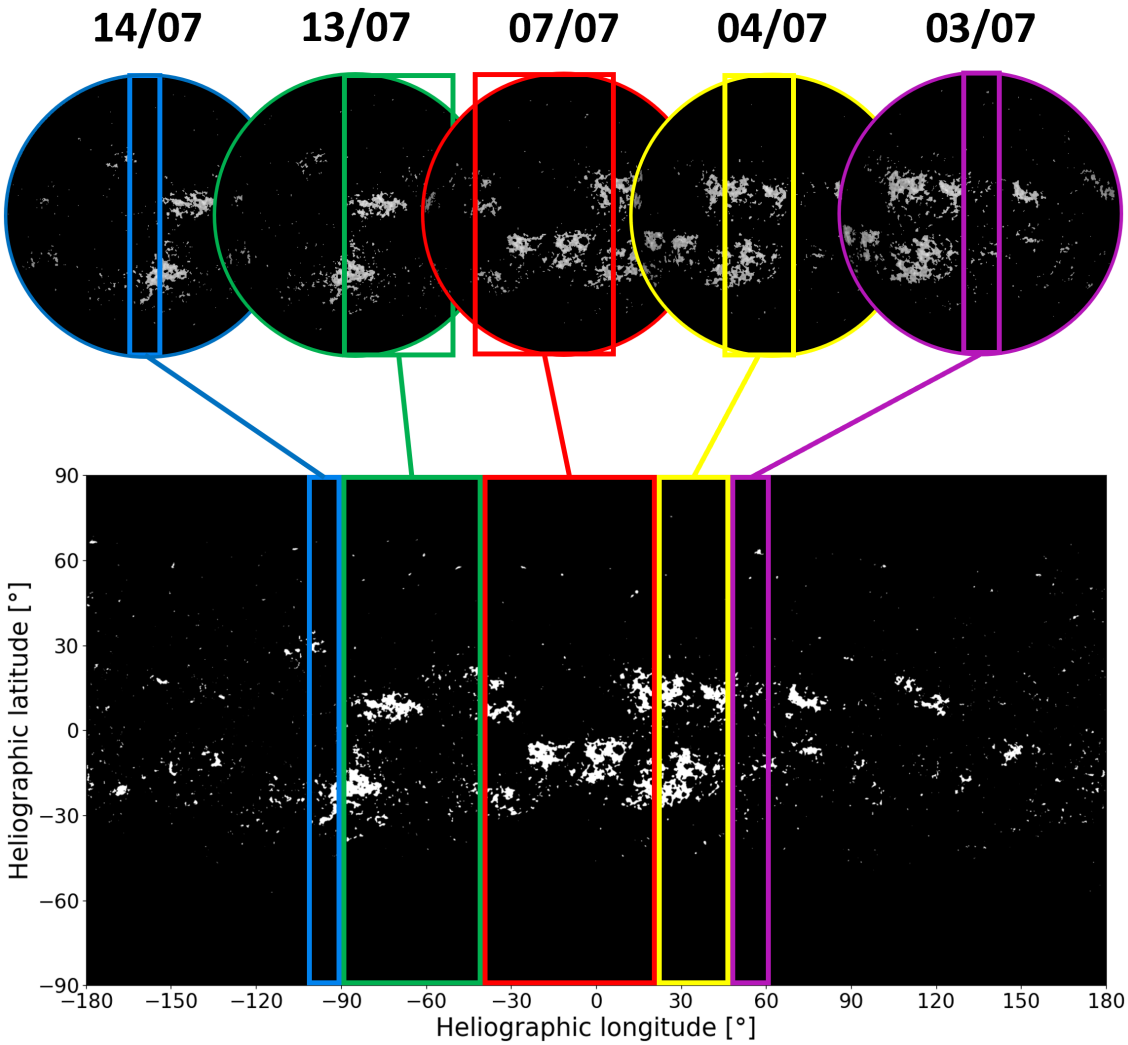

Fig. 3.21. Illustration of the determination and the assembling of the meridional slices for each image during a solar rotation. Here we show a synoptic map around the 7th of July 2014. We can clearly see that the slices width for each day depends on the previous and next days of observations.

3.3.3 Intensity variations correction

Our first attempt to construct synoptic map was using the L1 images, obtained after the processing described in Section 3.1.1. In that way, we end up with a synoptic map showing intensity variations between the segments, with sharp transitions (see Figure 3.22). As such artificial inhomogeneities and discontinuities will degrade the photometric accuracy of the subsequent steps of our analysis, we must correct the map from the center-to-limb variation (in this case, it is center-to-pole variation as we have kept only the central part of the images) but we must also normalize the intensity of the synoptic map. To do so, we have tried several ways like normalisation by the maximum value of the map or by the 50th percentile of the map. Figure 3.23 displays the results for each case. We can see that none of the maps provides a very satisfying result to remove the

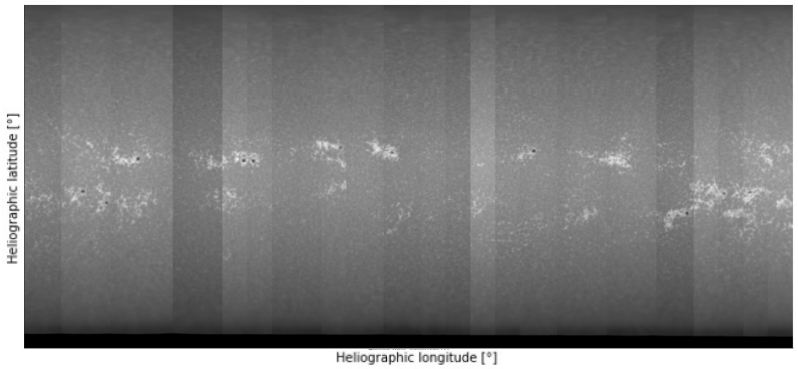

Fig. 3.22. Result of the construction of a synoptic map by using the L1 images and by assembling the slices of each image.

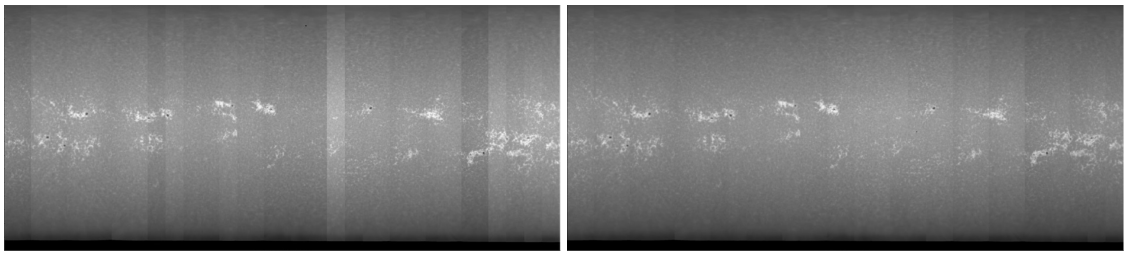

(a) Normalisation by the maximum value **(b)** Normalisation by the 50th percentile

Fig. 3.23. Same as Figure 3.22 but with normalisation of the intensity.

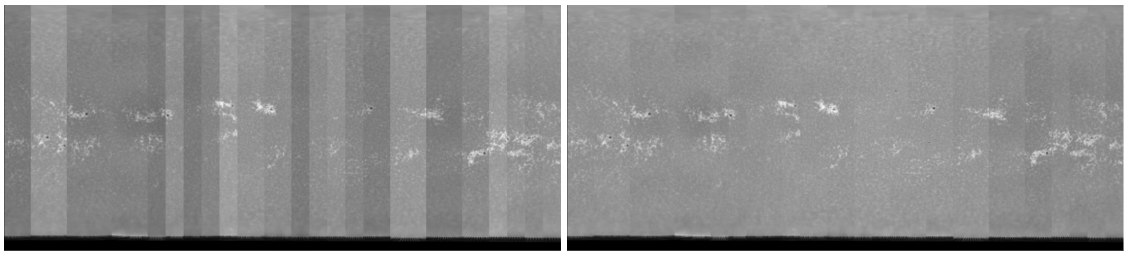

(a) Normalisation by the maximum value **(b)** Normalisation by the 50th percentile

Fig. 3.24. Same as Figure 3.23 but after correcting the CLV.

intensity variation between the slices. Junctions between them are still visible on the maps. Even after correcting the center-to-limb variation from the images, the results are not usable (see Figure 3.24). With a map without a uniform intensity across the entire map, it is impossible to run our segmentation algorithm.

Therefore, instead of creating the synoptic map with L1 images and then segmenting the brightest structures, we first have performed the segmentation on the images and then created segmented synoptic maps. So we followed the same method as explained in Section 3.1.3 for the CLV correction and in Section 3.2.1.2 for the segmentation to have segmented images before constructing the synoptic maps. Hereafter, these segmented images are referred to as solar masks.

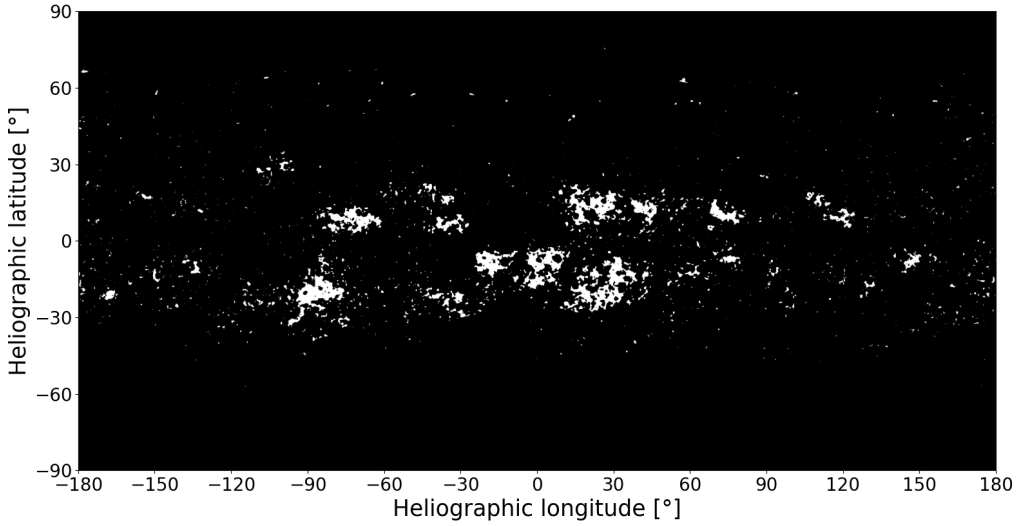

Fig. 3.25. Final result of the segmented synoptic map showing the evolution of the brightest chromospheric structures (plages and enhanced network) during a complete solar rotation around the 7th of July 2014.

We finally end up with a segmented synoptic map (see Figure 3.25) showing the evolution of the brightest chromospheric structures (plages and enhanced network) on the solar disk during a complete solar rotation.

3.3.4 Solar masks production

Based on the segmented synoptic maps obtained as in Figure 3.25, we reproduce solar masks by using an orthographic projection with various centers. For this, we use a python library, called Cartopy (Met Office 2010 - 2015), which is designed for cartographic projection and geospatial data visualization. By specifying the central latitude and longitude, we can generate masks of the Sun as if it was seen under an arbitrary inclination i. Figure 3.26 illustrates multiple examples of solar masks generated for different inclinations i from the South Pole-on view ($i = -90°$) to the North Pole-on view ($i = 90°$), based on the segmented synoptic maps. The gray areas on the maps represent the far-side of the Sun. As we can see, for a Pole-on view, the structures are distributed closer to the limbs, where they are foreshortened, which reduces their projected area. The effect of this variation will be discussed in Chapter 5.

As a consistency check, we have computed the fraction of solar disk covered by the segmented structures from the generated solar masks at an inclination $i = 0°$ (Equator-on view) and we compared this time series with the area fraction time series obtained from the L1 images (Figure 3.14). This comparison can be seen in Figure 3.27, where we plotted the monthly averaged value for each case and the comparison indicates that both time series match closely, except during a few months in 2014-2015. This good overall agreement as well as the effect of inclination on the plages and enhanced network coverage, are the topic of our second paper, described in Chapter 5.

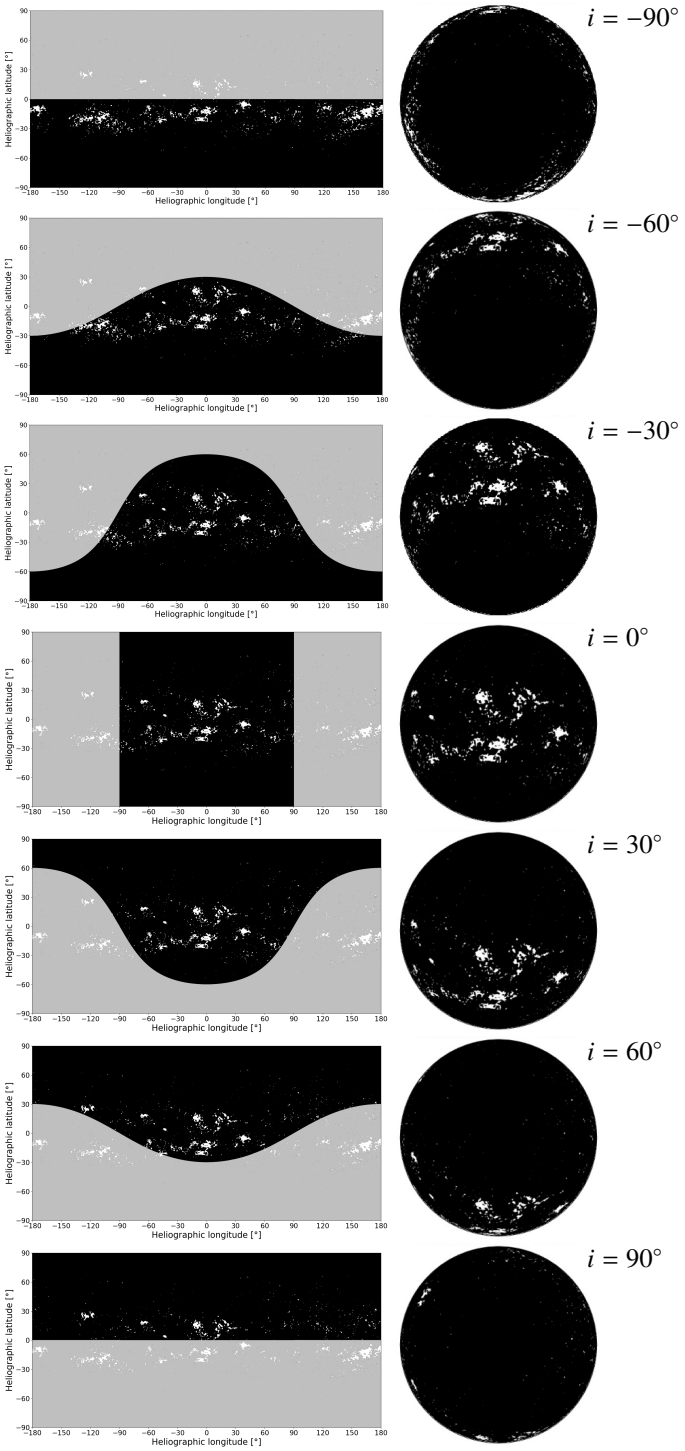

Fig. 3.26. Solar masks generation for different inclination angles i, indicated in the upper right corner of the panels and representing the number of degrees relative to the Equator-on view ($i = 0°$). Left column: Segmented synoptic maps illustrating the plages and enhanced network distribution during a complete solar rotation around the 8th of June 2014. The shaded areas (grey part) mark the far-side of the Sun. Right column: Solar masks generated. Inclinations of $i = -90°$ and $i = 90°$ correspond to the Sun's South Pole-on view and to the Sun's North Pole-on view, respectively.

Fig. 3.27. Comparison of the temporal variation of the fraction of the solar disk covered by the plages and enhanced network from L1 images (black curve) and from generated solar masks at an inclination $i = 0°$ (red curve).

Chapter 4

Comparison between direct solar observations and Sun-as-a-star observations

As explained in our motivations (Section 1.3), magnetic activity plays a crucial role in shaping our understanding of solar and stellar physics. Stars are so far from us that we cannot observe their surface details. However, we have another star, much closer, that can be used to study the magnetic structures, our star, the Sun. Although the Ca II K and H lines have been widely used to study the chromospheric activity of stars, with the S-Index, its connection to the coverage of magnetic structures is still poorly understood. The Ca II K line is also used to monitor the Sun, from which we can analyse the lower chromosphere and study the magnetic structures such as plages and network regions. Comparing both observations can provide useful information to increase our knowledge about the magnetic activity of solar-type stars.

For this analysis, we have used the full-disk solar images in the Ca II K line from the USET station (see Section 2.1) and the solar S-index data from TIGRE (see Section 2.2). Both datasets span the same time period, for approximately ten years since August 2013, so that the comparison is straightforward and doesn't need time alignment. The TIGRE dataset is smaller than that of USET, roughly half the size, due to the fact that TIGRE observes the Sun through the light reflected by the Moon. Therefore, observations depend on the lunar phases and are interrupted for several days around the New Moon, every $\sim$ 30 days. Additionally, TIGRE has experienced some instrumental issues that interrupted the operations of the telescope for several weeks, or even several months. Finally, as the telescopes are located in two distant places on Earth, it sometimes happens that one observes on a given day, but not the other. At the end, we have 790 days with observations on the same UT date that were used to perform the comparison between the plages and enhanced network area fraction from the USET images and the S-index from the TIGRE spectral measurements.

Moreover, we have used the Fourier power spectrum method to search for periodic signals in the time series. Those periodic signals are observed in the power spectrum as peaks at the corresponding frequency. For instance, two periodic modulations are well known for the Sun: the solar rotation which is ~ 27.27 days, and the solar activity cycle spanning approximately 11 years. Therefore, we expect to see peaks around the frequencies associated to those periods. We have analysed the properties of those periodic modulations and study their variations over the activity cycle.

This study was published in Astronomy & Astrophysics in mid-2024 and is available here : https://doi.org/10.1051/0004-6361/202450125.

A&A, 689, A95 (2024)
https://doi.org/10.1051/0004-6361/202450125

Astronomy & Astrophysics

Relationship between TIGRE solar S-index and USET Ca II K full disk images

G. Vanden Broeck[1,2,⋆], S. Bechet[1], F. Clette[1], G. Rauw[2], K.-P. Schröder[3], and M. Mittag[4]

[1] Department of Solar Physics and Space Weather, Royal Observatory of Belgium (ROB), Av. Circulaire 3, 1180 Uccle, Belgium
[2] University of Liège, Allée du 6 août, 19c – Bât. B5c, 4000 Liège, Sart-Tilman, Belgium
[3] Departamento de Astronomía, Universidad de Guanajuato, Apartado Postal 144, 36000 Guanajuato, Mexico
[4] Hamburger Sternwarte, Universität Hamburg, Gojenbergsweg 112, 21029 Hamburg, Germany

Received 25 March 2024 / Accepted 30 May 2024

ABSTRACT

Context. Full disk observations of the solar chromosphere in the Ca II K line represent a valuable dataset for studies of solar magnetic activity. The well known S-index is widely used to investigate the magnetic activity of stars, however, its connection to the coverage of stellar magnetic structure is still poorly understood.
Aims. We use the archives of full disk Ca II K images taken by the Royal Observatory of Belgium with the Uccle Solar Equatorial Table (USET) to derive the area fraction of the brightest chromospheric structures over the last decade. These data have allowed us to study the end of the solar cycle 24 and the beginning of the solar cycle 25. Our aim is to compare this dataset with the solar S-index from the Telescopio Internacional de Guanajuato Robotico Espectroscopico (TIGRE) lunar spectroscopy to analyze the relationship between a disk coverage index and an integrated spectrum. We also searched for periodic modulations in our two datasets to detect the solar rotation period.
Methods. We used more than 2700 days of observations since the beginning of the Ca II K observations with USET in July 2012. We performed a calibration of the images (re-centering and center-to-limb variation correction). The brightest regions of the solar surface (plages and enhanced network) were then segmented using an algorithm based on an intensity threshold. We computed the area fraction over the solar disk and compared it with the S-index from TIGRE. For the detection of periodic modulations, we applied a discrete Fourier power spectrum method to both datasets.
Results. A tight linear relationship was found between the USET area fraction and the TIGRE S-index, with an improved correlation obtained in the low-activity regime by considering the enhanced network. In both time series, we detected the modulation caused by the rotation of bright structures on the solar disk. However, this detection is constrained in the case of TIGRE due to its observation strategy.
Conclusions. We studied the correlation between the disk coverage with chromospheric structures and the variability of the S-index on an overlapping period of ten years. We concluded that the disk coverage index is a good proxy for the S-index and will be useful in future studies of the magnetic activity of solar-type stars. The USET area fraction dataset is most appropriate for evaluating the solar rotation period and will be used in future works to analyze the impact of the inclination of the stellar rotation axis on the detectability of such periodic modulations in solar-type stars.

Key words. Sun: activity – Sun: chromosphere – Sun: faculae, plages – stars: activity – stars: chromospheres – stars: solar-type

1. Introduction

Since 1960, the chromospheric activity of a large number of stars has been monitored in the Ca II K and H lines. This program was initiated in the context of the HK project at Mount Wilson (Wilson 1978) and eventually led to the creation of the Mount Wilson S-index, further denoted as S_{MWO}. Over more than three decades, hundreds of stars (including the Sun) were observed to search for stellar activity (Baliunas et al. 1998). The HK project was followed by the Lowell's monitoring, a complementary synoptic survey at the Lowell observatory with the Solar-Stellar Spectrograph (SSS; Hall et al. 2007) and the TIGRE project (Schmitt et al. 2014). Additional stellar activity surveys come from radial velocity exoplanet searches where S-indices can be derived as a by-product, such as HARPS (Lovis et al. 2011) and California Planet Search (Isaacson & Fischer 2010). Recently the arrival of large spectroscopic surveys (Zhang et al. 2022) has allowed for observations of hundreds of thousands of stars to be carried out.

The Ca II K line is also used to monitor the Sun, the only star for which we can resolve the surface in detail. The observations of the Sun's full disk in this line started in 1893 in Meudon and are still running in various sites around the world, supplying a long-term dataset (Chatzistergos et al. 2022). The images show the lower chromosphere and provide information on plages and network regions that are the manifestations of surface magnetic fields in this part of the solar atmosphere. Thus, they can be used to study the evolution of magnetic activity.

While the S-index is widely used to study the magnetic activity of late-type stars, its connection to the coverage of stellar magnetic structure is poorly understood (Shapiro et al. 2014; Meunier 2018; Dineva et al. 2022; Singh et al. 2023); in particular, the effect of the inclination of the stellar rotation axis on the S-index variability (Shapiro et al. 2014; Sowmya et al. 2021). Our goal in this article is to study the relationship between the disk coverage with chromospheric structures and the variability

⋆ Corresponding author; gregory.vandenbroeck@observatory.be

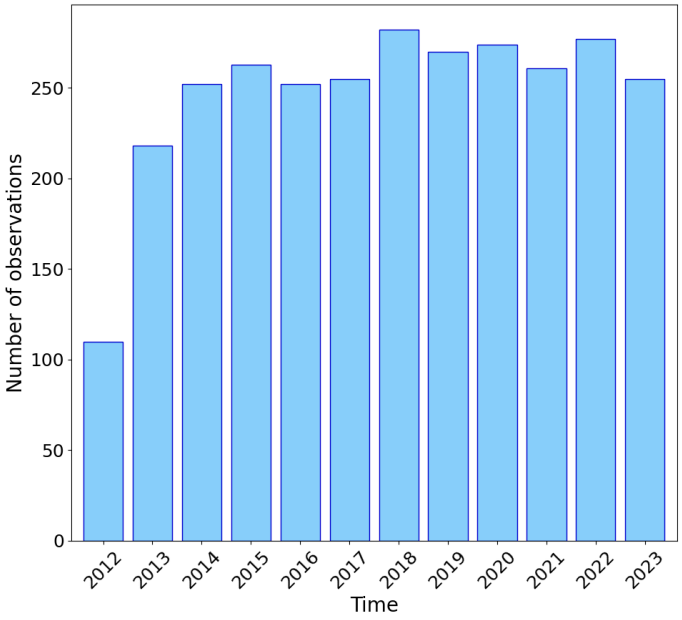

Fig. 1. Number of Ca II K images per year from the USET station.

of the solar S-index to provide a useful proxy for subsequent studies on solar-type stars.

To assist in approaching an answer to these questions, we have taken advantage of two datasets taken simultaneously over the past decade: the solar S-index from TIGRE and the Ca II K full disk images from USET. In Section 2, we present the technical specifications of those datasets. In Section 3, we describe the image processing method to construct a disk-resolved index from full disk images. In Section 4 we study the modulation produced by the bright structures on the time series. Finally, in Section 5, we study the correlation between the two indices and derive a proxy for the S-index based on Ca II K images. This proxy will be used in a subsequent paper to study the magnetic activity of solar-type stars and the effect of the inclination of the rotation axis.

2. Datasets

2.1. USET

The Uccle Solar Equatorial Table (USET) station at the Royal Observatory of Belgium (ROB), located in Uccle, south of Brussels, has been acquiring full disk solar images in the Ca II K line since July 2012 (Bechet & Clette 2002). In addition, the station carries three other solar telescopes (white-light, 656.3 H-alpha, and sunspot drawings) to simultaneously monitor the photosphere and the chromosphere. Figure 1 shows the total number of days of observations per year, with an average of 260 per year. The gaps are essentially due to bad weather.

The optical set-up consists in a refractor of 925 mm focal length and 132 mm aperture. The filter is temperature-controlled and its central wavelength is $\lambda = 3933.67$ Å, with a bandwidth of 2.7 Å. The images are acquired with a 2048×2048 CCD with a dynamic range of 12 bits. The instrumental set-up is the same since 2012, except for the introduction of an additional neutral filter on July 10, 2013. The acquisition cadence can go up to 4 frames per second in case of transient events to record, and the daily synoptic cadence is 15 minutes.

2.2. TIGRE

The Telescopio Internacional de Guanajuato Robotico Espectroscopico (TIGRE) is a 1.2 m robotic telescope located in Guanajuato, central Mexico (Schmitt et al. 2014). With its sole instrument HEROS, a spectrograph with a spectral resolution $R \sim 20.000$, TIGRE has collected more than 48.000 spectra of 1.151 different sources (González-Pérez et al. 2022). To obtain an integrated solar S-index, TIGRE observes the light reflected by the Moon. Therefore, it depends on the lunar phases and observations are interrupted for a few days around the New Moon. TIGRE has observed the Sun-as-a-star continuously since August 2013, except for a few gaps due to instrumental problems, with a total of approximately 1200 days.

3. Assessment of indices

3.1. USET disk-resolved index

The first step of the image processing consists of the automatic limb fitting, based on a combination of Canny edge detection and morphological operations (Gonzalez et al. 2009). Using the limb estimation, we detected the disk center and calculate the radius, assuming that the shape of the solar image is a circle. Finally, the disk was recentered in the middle of the image and the meta-data were filled following the SOLARNET standard (Haugan & Fredvik 2020), making level 1 of the image series. For this analysis, an automatic quality selection was performed to keep the best image recorded per day. Images with opaque clouds hiding some parts of the solar disk or strong atmospheric turbulence have been discarded. The non-radial inhomogeneity due to the presence of high-altitude veils or transparent clouds has not been corrected. This reduces the final sample to 2725 images.

The solar images showing the chromosphere present an intensity variation from the center to the limb, the so-called center-to-limb variation (CLV). This effect must be corrected to have the same level of background intensity relative to the chromospheric emissions that have been identified; otherwise, a different threshold should be applied depending on the considered region. The steps of the correction algorithm are the following.

1. We performed a polynomial fit on the order of 5 for a set of angles between 0° and 360°, with a step of 1°. For every angle, we calculate the residuals between the intensity profile along the radius and the fit and we kept the fit for the angle where the residuals are minimum. This gives a first guess of the intensity as a function of the radius without the presence of sunspots or plages.
2. We created a mask of the quiet solar disk I_{QS} based on that fit.
3. A first-guess corrected image was then obtained by $I_C = I_i/I_{QS}$ where I_i is the intensity of the initial image and I_C is the intensity of the corrected image.
4. Based on this first guess, we removed the bright plages following the segmentation method described in Chatzistergos et al. (2019) so that the next step does not use those bright structures in the computation.
5. Finally, we repeated steps 1, 2, and 3 but with step 1 (fit of the intensity profile) performed by computing the mean intensity of the whole image without considering the bright plages.

Figure 2 shows an example of the intensity variations across the solar disk before and after applying the CLV correction. On the corrected image (right image), the pixel intensity is normalized to 1 (quiet Sun regions) with minimal values at 0 (out of the solar disk). The variations show peaks upwards and downwards,

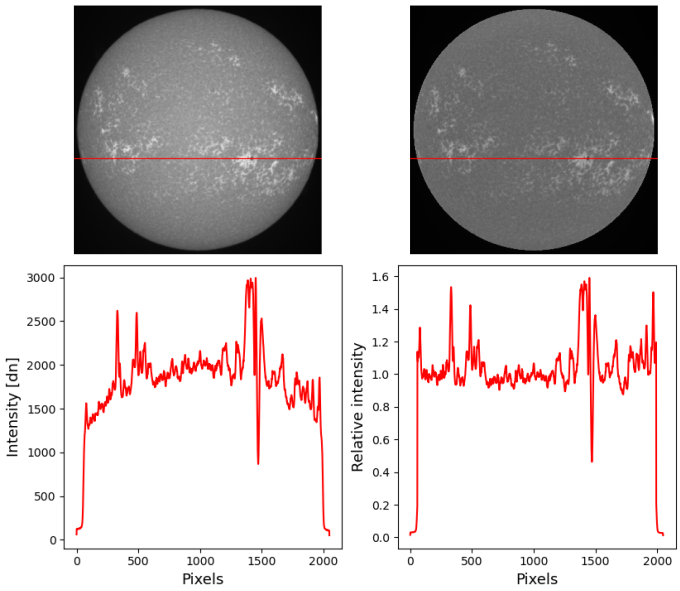

Fig. 2. Example of the results after the CLV correction. Top panels display the Ca II K images from the 16th of January 2015 before the correction (left) and after the correction (right) while bottom panels display the intensity variation on the horizontal red line, from the left to the right of each image. The intensities are expressed in term of digital number (dn) for the raw image and intensity relative to the quiet Sun regions for the corrected image.

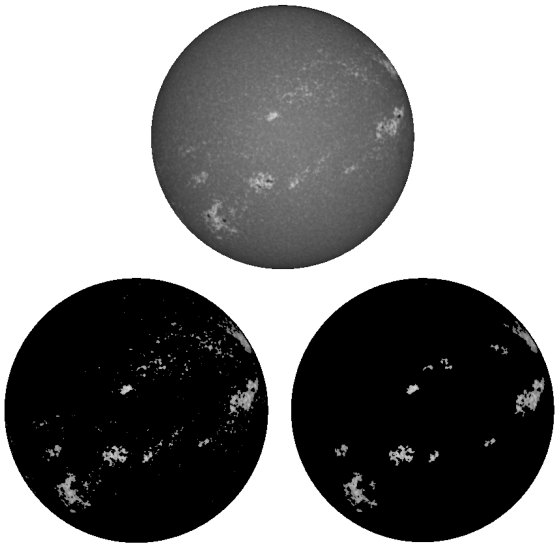

Fig. 3. Example of the results from the segmentation process. Top image represents the recentered raw image from the 29th of October 2013. Bottom images are the results of the segmentation with and without the enhanced network. Left image: plages and enhanced network. Right image shows the plages only.

which are due to the presence of plages and sunspots respectively. The small intensity variations are representative of the chromospheric network intensity.

The segmentation algorithm follows the method described in Chatzistergos et al. (2019). This method assumes a Gaussian brightness distribution of the pixels in the image, dominated by inactive areas known as the so-called quiet Sun. This distribution is enhanced on either side due to spots and bright structures. Due to their small spatial coverage, sunspots have a small contribution on the low side of the distribution. On the other hand, bright and extended structures have a more significant contribution and enhance the distribution for high intensity values. In this study, we segmented the plages (P), which are the chromospheric counterparts of the faculae. These structures have been extensively used to study the chromospheric activity. Here, in addition, we considered the enhanced chromospheric network (EN). This has been defined in Worden et al. (1998) and Singh et al. (2023) as small regions of decaying plages, dispersing into bright patches. The enhanced network is much smaller than the plages but just as bright. The segmentation of both structures is based on the same intensity threshold estimated iteratively from the intensity distribution and we distinguish the plages and the enhanced network based on an area threshold. At the center of the disk, the value of the area fraction threshold is 0.0004 and it decreases with distance from the center (taking the deprojection of the area into account). To prevent artifacts resulting from processing the last few pixels near the limb, our segmentation algorithm exclusively takes pixels within 99% of the solar disk radius into account. Figure 3 shows an example of the results of the segmentation process for the plages with the enhanced network and for the plages only. As expected, the enhanced network can be observed as bright patches that are close to the extended bright structures, but not covering the entire solar surface. The impact of the enhanced network will be discussed further in Section 5.2.

The area of plages and enhanced network, $A_{\rm PEN}$, expressed in fraction of solar disk, is the number of pixels of plages and enhanced network over the total number of solar disk pixels. Figure 4 illustrates the evolution of the monthly averaged $A_{\rm PEN}$ as a function of time, with the uncertainty increasing with the area. The error bars on $A_{\rm PEN}$ were estimated from dates where more than four images not affected by clouds were available. For such days, we computed the mean and the standard deviation of $A_{\rm PEN}$. After removing some outliers, deviating by more than 3σ, we found that the error follows a roughly linear trend with $A_{\rm PEN}$ and, thus, we adjusted a linear relation to compute the uncertainty for any value of $A_{\rm PEN}$. The plot shows a long-term modulation following the solar cycle, as illustrated in the bottom panel with the Wolf number evolution from the USET sunspot drawings. The Wolf number is based on straight counts separating groups and individual spots. It reflects the emergence of magnetic flux (Clette et al. 2016). Shorter modulations are also present and are due to the solar rotation. This is studied further in Section 4.

3.2. TIGRE S-index

The Mount Wilson S-index quantifies the chromospheric emission in the core of the Ca II H & K lines, measuring the flux in a triangular shape bandpass with a full width at half maximum (FWHM) of 1.09 Å, denoted by N_H and N_K in Eq. (1). To minimize the impact of atmospheric turbulence and varying atmospheric emissions, the measured line core fluxes are normalized relative to the flux of two bandpasses of 20 Å width in nearby continua redwards and bluewards of the H & K lines, denoted by N_R and N_V, respectively. A multiplicative factor α is introduced to standardize different instruments and calibrate them on the same S-index scale (Vaughan et al. 1978; Duncan et al. 1991), so that the $S_{\rm MWO}$ is defined as:

$$S_{\rm MWO} = \alpha \left(\frac{N_H + N_K}{N_R + N_V} \right). \quad (1)$$

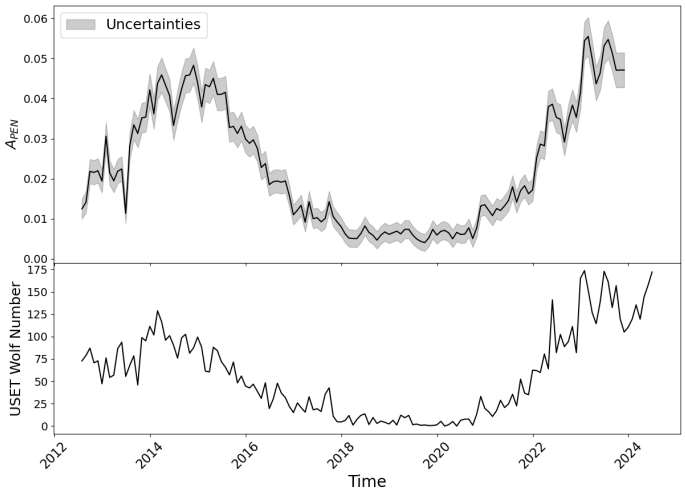

Fig. 4. Temporal evolution of monthly averaged $A_{\rm PEN}$, the area of plages, and the enhanced network, expressed as fractions of the solar disk (top). Temporal evolution of monthly averaged USET Wolf number (bottom). Uncertainties on the $A_{\rm PEN}$ depend linearly on the area.

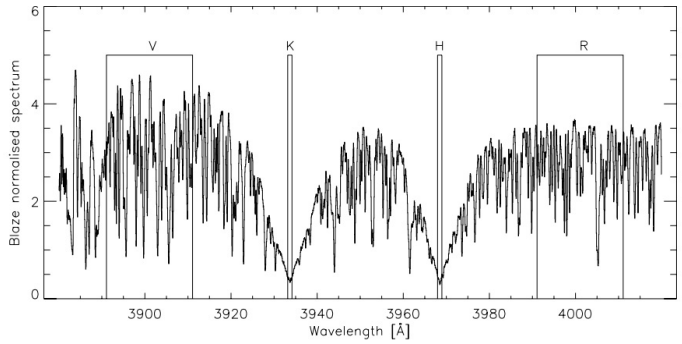

Fig. 5. Solar Ca II H & K spectrum as inferred from lunar spectra along with the TIGRE bandpasses used for the S-index calculation (Mittag et al. 2016). The bandwidth is 1 Å in the core of the lines and about 20 Å in the two nearby continua. Bandpasses in the core of the lines are rectangular.

The S-index measured by TIGRE, denoted as $S_{\rm TIGRE}$, represents the emission in the core of the Ca II H & K lines with a rectangular bandpass of 1 Å (see Figure 5), instead of a triangular bandpass as with Mt. Wilson. In order to compare the TIGRE results with the original Mt. Wilson measurements, the $S_{\rm TIGRE}$ values are converted to the Mt. Wilson system by means of regular observations of a sample of 50 stars with very well known $S_{\rm MWO}$ values (see Figure 2 of Mittag et al. 2016 for the results of this comparison). A well-defined linear transformation was found:

$$S_{\rm MWO} = (0.0360 \pm 0.0029) + (20.02 \pm 0.42)\, S_{\rm TIGRE}. \quad (2)$$

Hereafter, we use Eq. (2) to convert TIGRE measurements into the $S_{\rm MWO}$ index throughout the rest of the paper. Figure 6 shows the temporal evolution of the monthly averaged solar S-index from TIGRE for both scales: $S_{\rm TIGRE}$ (left) and $S_{\rm MWO}$ (right). The exposure time of the spectra were carefully chosen to reach a typical uncertainty of 1% in $S_{\rm TIGRE}$, including potential adjustments to compensate for bad seeing conditions or elevated extinction (Hempelmann et al. 2016). The TIGRE to Mt. Wilson S-index calibration uses the same 40 calibration stars as the Mount Wilson team (Baliunas et al. 1995); hence, this guarantees a good long-term stability. Any drifts would require a larger

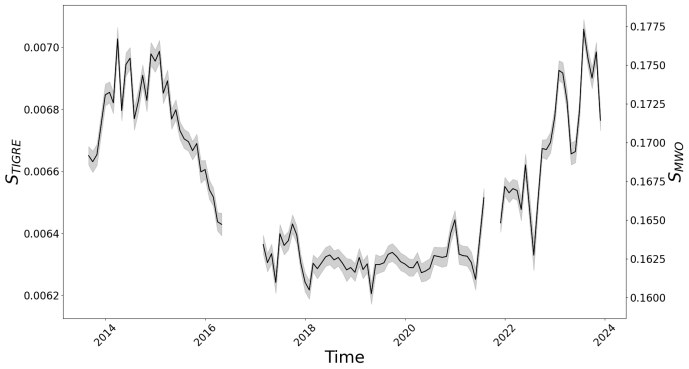

Fig. 6. Temporal evolution of the monthly averaged solar S-index from TIGRE covering almost a complete solar cycle (from August 2013 to December 2023). Left axis displays the $S_{\rm TIGRE}$ values while the right axis shows them in the Mt. Wilson scale using Eq. (2).

fraction of those calibration stars to change their activity in the same sense. However, these were selected by Olin Wilson over a long period of time as relatively invariable and the size of the calibration star sample should be sufficient to average out any individual trends. The gaps in Figure 6 refer to the two main instrumental issues that TIGRE had faced: in 2016, the observations were stopped for ∼9 months due to mirror cell refurbishment and mirror aluminization; in 2021, the uninterruptible power supply batteries were in poor conditions and prevented the observations for ∼3 months (González-Pérez et al. 2022). Nevertheless, the long-term variation due to the solar activity cycle is evident and we also observe some variations on the short-term scale. This is discussed further in the next section.

4. Solar cycle and solar rotation modulations from USET and TIGRE

4.1. USET disk-resolved index

To search for the presence of a rotational modulation in the time series of $A_{\rm PEN}$, we used the discrete Fourier power spectrum method developed by Heck et al. (1985) amended by Gosset et al. (2001). This method explicitly accounts for the irregularities that typically affect astronomical time series creating gaps due to poor weather conditions or instrumental problems. The Fourier method offers a sensitive tool to search for the presence of periodic modulations: the existence of such a periodic signal leads to a peak in the power spectrum at the corresponding frequency.

Figure 7 illustrates the power spectrum of the full time series of $A_{\rm PEN}$ for frequencies between 0 and 2 $\rm d^{-1}$, as well as a zoom on the region between 0 and 0.1 $\rm d^{-1}$. The lower panel displays the spectral window which illustrates the aliasing phenomenon that results from the sampling of the time series. Because the USET data are taken with a nearly regular sampling at the pace of one observation per mean solar day, except for the gaps due to bad weather, the spectral window contains only peaks at integer multiples of 1 $\rm d^{-1}$. For a time series containing a signal of true frequency, ν, sampled with a regular time step of 1 day, the power spectrum will not only host a peak at ν, but also at the aliasing frequencies $1 + \nu$, $1 - \nu$, and so on.

The power spectrum of the $A_{\rm PEN}$ full time series is dominated by a peak at low frequency associated with the long-term variability arising from the solar activity cycle. The highest peak is however not located exactly at the frequency of the

11-year cycle (around 0.00025 d^{-1}). This is no surprise since the USET data cover the period from July 2012 until November 2023, which is only about a single solar activity cycle (i.e., large parts of cycle 24 and the rising part of cycle 25). The second important feature in the power spectrum is a group of peak which are close, although not strictly identical, to the frequency (ν_{Car} = 0.0367 d^{-1}) associated with the Carrington synodic rotation period (27.2753 d). The highest power is recorded at a frequency of 0.0383 d^{-1} (period of 26.1342 d, close to the synodic rotation period of the Sun at the equator), although as we will see below, the exact location of the highest peak changes with epoch and the signal is actually the manifestation of a quasi-periodic rather than a genuine periodic phenomenon. These peaks reflect rotational modulation resulting from an asymmetry in the longitudinal distribution of active regions. An important point to note is that the group of peaks in the power spectrum extends over a range in frequencies that is significantly (a factor of 10) broader than the natural width expected from the total duration of the time series. This reflects the fact that the plages are spread over a range of latitudes hence are modulated by a range of rotational periods. Therefore, the detected group of peaks is a blend of a number of frequencies, thus forming a quasi-periodic feature in the power spectrum.

An important question is whether the properties of this periodic modulation may vary over the activity cycle. Such variations can be expected, for instance, as a function of the overall activity level, as well as when the degree of uniformity of the longitudinal distribution of the plages and enhanced network changes. Indeed, a strictly uniform distribution would produce no modulation at all, regardless of the overall level of activity. To address this point, we have first de-trended the time series for the long-term (solar cycle) variations. To do so, we first splitted the total data set into 12 intervals of 347 days duration each. On each of these intervals, we evaluated the mean value of A_{PEN} and adjusted the polynomial by a degree of 6 to these points. We tested lower degree polynomials, but 6 was the lowest degree that would allow us to represent the overall shape of the long-term variations well. This long-term trend is shown by the red curve in the top panel of Fig. 8 and was then subtracted from the original USET time series. We then followed the approach of Rauw & Nazé (2021) to build a time-frequency diagram, see Figure 8, by computing a Fourier transform of the data in sliding windows of 136 days duration, shifted in steps of 34 days[1].

We can distinguish three different behaviors. For each case, we illustrate the link between the detection of a modulation due to the rotation and the associated magnetic structures present on the solar disk. For this purpose, we used synoptic maps showing the evolution of segmented bright chromospheric structures for several full solar rotations (see figures in Appendices A, B, and C). They are constructed by juxtaposing the central part of consecutive deprojected segmented images. Those synoptic maps display the temporal evolution of the structures over several solar rotations (top panels) and the sum of bright pixels along vertical strips (bottom panels). These sums were evaluated in sliding windows with a width of 180° in longitude, corresponding to an entire daily image, and shifted in steps corresponding to the solar rotation over one day.

[1] We also computed a time-frequency diagram with a sliding window of 680 days. Whilst this leads to a higher resolution in frequency, it degrades the temporal resolution, smearing out the temporal variations of the power spectrum. Still, the overall behavior is fully consistent with Fig. 8.

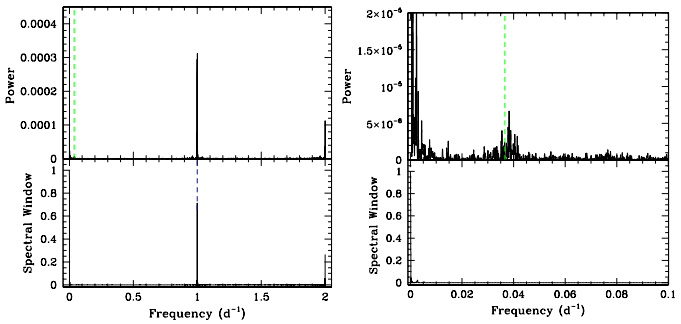

Fig. 7. Fourier power spectrum (top) and spectral window (bottom) for the A_{PEN} time series for frequencies between 0 and 2 d^{-1} (left). The green dashed line in the power spectrum panel yields ν_{Car}, while the blue dashed line in the spectral window identifies the main aliasing frequency at 1 d^{-1}. Right: Same, but zooming on the frequency range between 0 and 0.1 d^{-1}.

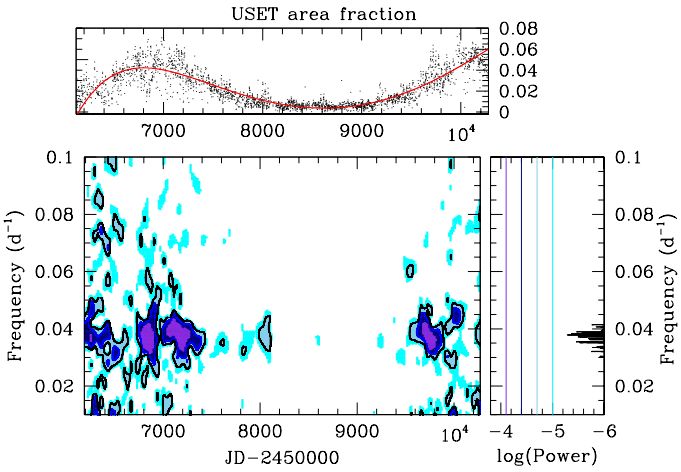

Fig. 8. Time-frequency diagram of the A_{PEN} time series. The top panel displays the observed data along with the red curve providing the fit by a polynomial to the long-term variations based on a degree of 6. The color-scale image provides the evolution of the Fourier power spectrum with the epoch on the x-axis. Violet, dark blue, light blue, and cyan colors stand for power $\geq 8 \times 10^{-5}$, $\geq 4 \times 10^{-5}$, $\geq 2 \times 10^{-5}$, and $\geq 10^{-5}$. The right vertical panel illustrates the Fourier power spectrum evaluated over the full duration of the USET time series. The colored straight lines correspond to the scale used in the time-frequency diagram.

First, the rotational modulation is most prominently seen during some time intervals near the maximum of cycle 24 and during one episode in the rising part of cycle 25. More specifically, there are three broad maxima of visibility of this modulation around JD 2456800 (2014 May 22), JD 2457200 (2015 June 26), and JD 2459730 (2022 May 30). The first of these intervals lasts about 100 days, while the second and third one last about 200 days. Figures A.1, A.2, and A.3, referring to the broad maxima in Figure 8, show a succession of episodes with compact groups of plages and episodes with less activity. This is consistent with the results obtained in Dineva et al. (2022), for the same time interval, revealing the presence of rotation pattern separated into compact groups associated with large active regions rotating on and off the disk. The asymmetry in the longitudinal distributions could be related to the fact that some longitudes seem more favorable for the emergence of magnetic flux as observed for sunspot groups under the name of active longitudes (Usoskin et al. 2007). Figures A.1, A.2 and A.3 further show that the modulation of the sum of bright pixels is not strictly periodic.

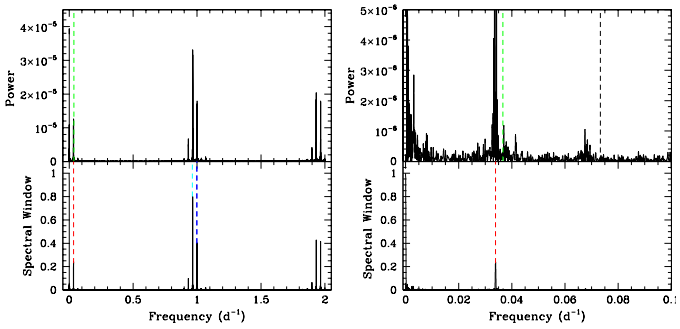

Fig. 9. Fourier power spectrum (top-left) and spectral window (bottom-left) for the TIGRE solar S-index time series for frequencies between 0 and 2 d^{-1}. The green dashed line in the power spectrum yields $\nu_{\rm Car}$, while the red, cyan and blue dashed lines in the spectral window plot identify the main aliasing frequencies which are respectively 0.0339 d^{-1}, 0.9661 d^{-1}, and 1.0000 d^{-1}. Right: Same details, but zooming on the frequency range between 0 and 0.1 d^{-1}. The dashed black line corresponds to $2\nu_{\rm Car}$.

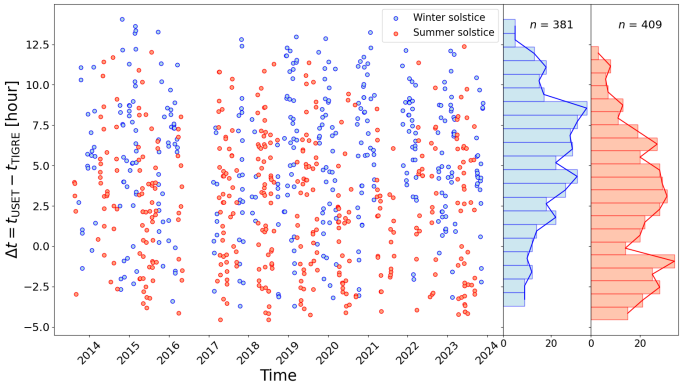

Fig. 10. Time differences between USET and TIGRE. Data points are divided in two series: one that is six months around the winter solstice (in blue) and the other six months around the summer solstice (in red). Their corresponding histograms are displayed on the right panels.

Indeed, the synoptic maps indicate that the plages extend over a range in solar latitudes. Therefore, the observed modulation consists of the combination of signals having different rotational frequencies.

Secondly, even near solar maximum there are time intervals during which there is no clear detection of rotational modulation. At those epochs, the distribution of the magnetic structures is nearly uniform in longitude as illustrated on the Figures B.1 and B.2. Finally, as expected, the signal from the solar rotation is essentially absent during solar minimum because either no plage is present, or if there is one, it lasts for less than a rotation (see Figure C.1).

4.2. TIGRE S-index

As a consistency check, we also applied our Fourier method to the time series of the TIGRE S-index values. The spectral window unveils a more complex situation than for the USET data. Indeed, the main aliasing frequencies are found at 0.9661 d^{-1}, 1.0000 d^{-1}, and 0.0339 d^{-1} (see Fig. 9). This latter aliasing frequency corresponds to one synodic month (29.53 days) and is due to the fact that TIGRE observes the Moon rather than the Sun. This also explains why the dominant aliasing frequency is found at 0.9661 d^{-1} rather than 1.0000 d^{-1}: since the Moon rises a bit later each night, the mean time interval between two consecutive observations is 1.035 days, rather than 1.000 day. Moreover, TIGRE cannot observe the Moon at phases too close to the New Moon; thus explaining the occurrence of the 0.0339 d^{-1} peak in the spectral window (red dashed line). This situation has tremendous consequences on the power spectrum. Indeed, the fact that the Carrington synodic rotation period happens to be very close to the synodic month prevents us from obtaining a clear signature of a rotational modulation in the Fourier transform of the TIGRE S-index values. On the one hand, the aliasing via the 0.0339 d^{-1} frequency replicates the low-frequency peaks which pollute the frequency domain near the Carrington frequency (see Fig. 9). On the other hand, the gaps in the time series of S-index measurements around each New Moon phase reduce the amplitude of the peaks associated with rotational modulation making them more difficult to distinguish against the overall noise level. This indicates that because of the TIGRE observing strategy, the S-index values are less sensitive to solar rotation than the USET data.

5. Comparison between USET and TIGRE

In this section, we study the correlation between $A_{\rm PEN}$ and the solar S-index derived from TIGRE observations of the Moon. First, we characterize the temporal differences between both datasets (Section 5.1) and then study quantitatively their correlation (Section 5.2).

5.1. Temporal overlap between USET and TIGRE

To compare the S-index and the area fraction, we first select overlapping data. This reduces the 2725 USET data to 790 images. Ideally the selected data should be recorded simultaneously. In practice, Brussels and Mexico are separated by seven time-zone hours but the fact that TIGRE observes the Moon and USET the Sun partially compensates the time difference.

Figure 10 shows the time differences between USET and TIGRE observations for the selected sample. Data are split in two groups based on the time of observation: six months around the winter solstice and six months around the summer solstice. We observe a seasonal effect on the time differences between USET and TIGRE: it is higher around the winter solstice than around the summer solstice. This is not surprising because in winter, the Sun rises later and sets earlier, so that in Brussels, we observe it a few hours later in the morning (observations start around 9–10 am); whereas, in Mexico, the night falls earlier so the observations are made earlier. The highest time differences correspond to situations where the USET observations in Brussels are made later in the afternoon, due to bad weather conditions in the morning for example and the TIGRE observations in Mexico are made earlier in the night. The absolute averaged time difference between USET and TIGRE is 4.13 hours and the impact of the appearance or disappearance of a structure is therefore negligible. Within this time, the Sun rotates by ~2° and the variation of the area fraction is smaller than the uncertainties. Moreover, the limb structures are geometrically compressed, so their contribution to the total area fraction, $A_{\rm PEN}$, is tiny.

5.2. Correlation between USET and TIGRE indices

The correlation between the time overlapping area fraction from USET and the solar S-index from TIGRE is shown on Figure 11. The top panel displays the area fraction of the plages without considering the enhanced network, $A_{\rm P}$, and the bottom panel represents the area fraction of the plages with the enhanced network,

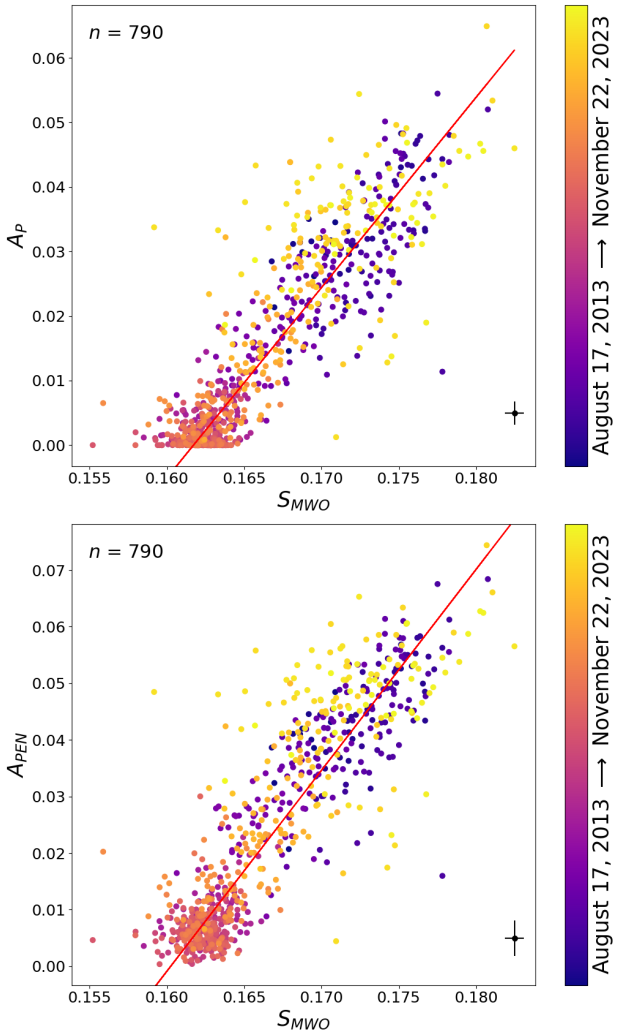

Fig. 11. Correlation between daily values of the solar S-index from TIGRE (in the Mount Wilson scale) and the USET area fraction. Top panel: plages only, A_P. Bottom panel: plages and enhanced network, A_{PEN}. The parameter n represents the number of data, and the chronological order is color-coded. The first and last date of the data are given next to the color bar. Additionally, a linear fit was performed to the data (red solid line). A mean error bar is displayed on the bottom right corner to have an idea of the uncertainties on the data.

A_{PEN}. For plages area close to zero (top panel), there are still some decaying plages (which constitute the enhanced network) present on the solar surface and that contribute to the S-index. As expected, considering the enhanced network (bottom panel) makes a better correlation at low values and it reflects better the S-index.

First, we observe that the two datasets are linearly correlated, with a high Pearson correlation coefficient of 0.88, according to this equation:

$$A_{PEN} = (3.55 \pm 0.06)\, S_{MWO} - (0.57 \pm 0.01), \quad (3)$$

where A_{PEN} is the area fraction of the chromospheric structures (plages and enhanced network) from USET, and S_{MWO} the solar S-index from TIGRE in the Mt. Wilson scale.

A second observation concerns the distribution of points around the fit. A small fraction of points (a bit more than 1%) deviates with 3σ. This corresponds to images with a lower quality and where the segmentation is less robust. Apart from these outliers, there is a dispersion which is larger than the uncertainty on the data (displayed as a mean error on the bottom right corner). Various sources can explain this dispersion. One potential source is the image quality and the fact that residual non-radial inhomogeneity is still present, affecting the segmentation. Another hypothesis is that smaller and fainter bright structures not included in our disk-resolved index have a non-negligible contribution to the S-index. These elements could be the active network representing small bipolar areas and the quiet network defining the boundaries of the supergranulation (Meunier 2018).

6. Discussion and conclusion

We studied the correlation between the presence of bright structures in the solar chromosphere, based on USET images in the Ca II K line and the variability of the solar S-index, obtained with the TIGRE telescope on an overlapping period of ten years, spanning a large portion of cycle 24 to the beginning of cycle 25.

We have constructed a disk-resolved time series from the USET images, segmenting the brightest structures which are the plages and the enhanced network. The correlation between the disk-resolved index and the S-index is well described by a linear relation, but a broad dispersion is present. Including small bright elements such as the active network and the quiet network could help to reduce the dispersion. Such a segmentation needs a more advanced processing of the image to remove the non-radial inhomogeneity produced by clouds and to compensate the turbulence, both effects being unavoidably present on images acquired by ground-based instruments.

For both time series, we have detected the modulation due to the rotation of bright structures on the disk and identified various behaviors at different phases of the solar cycle. From illustrative synoptic maps, we have shown that the detection of the modulation of the rotation is due to an asymmetry in the longitudinal distribution of the plages. This could be studied further and linked to the mechanism of active longitudes observed for sunspot groups. The detection of the rotation is intrinsically limited for TIGRE due to its observing strategy. In order to characterize the modulation on longer timescales, such as entire solar cycles, we would need long-term combined datasets. This could be done by taking advantage of existing long-term datasets in Ca II K and S-index. After a cross-calibration between the datasets, the correlation between these indices could then be studied on a longer period, covering the minimum of the solar cycle 23, stated as a low minimum (Schröder et al. 2012).

As the S-index is used to characterize the magnetic activity of Sun-like stars, a natural question arises as to whether stars seen under a different viewing angle, far from the equator, would also show the rotational modulation. We consider whether it is still possible to detect this rotational modulation for such inclinations and whether there is a specific inclination above which it is no longer possible to detect the modulation. Such a study could draw from on the present work, using the area fraction as a proxy for the S-index, and building an area fraction for different inclinations. This exploration will be the topic of a forthcoming paper.

Acknowledgements. The authors wish to thank Theodosios Chatzistergos from the Max Planck Institute for Solar Research System, in Germany, for his help and his advice on the segmentation method. Grégory Vanden Broeck was supported by a PhD grant awarded by the Royal Observatory of Belgium. The USET instruments are built and operated with the financial support of the Solar-Terrestrial Center of Excellence (STCE).

References

Baliunas, S. L., Donahue, R. A., Soon, W., & Henry, G. W. 1998, ASP Conf. Ser., 154, 153
Baliunas, S. L., Donahue, R. A., Soon, W. H., et al. 1995, ApJ, 438, 269
Bechet, S., & Clette, F. 2002, USET Images L1centered (Royal Observatory of Belgium (ROB))
Chatzistergos, T., Ermolli, I., Krivova, N. A., & Solanki, S. K. 2019, A&A, 625, A69
Chatzistergos, T., Krivova, N. A., & Ermolli, I. 2022, Front. Astron. Space Sci., 9, 336
Clette, F., Lefèvre, L., Cagnotti, M., Cortesi, S., & Bulling, A. 2016, Sol. Phys., 291, 2733
Dineva, E., Pearson, J., Ilyin, I., et al. 2022, Astron. Nachr., 343, e23996
Duncan, D. K., Vaughan, A. H., Wilson, O. C., et al. 1991, ApJS, 76, 383
Gonzalez, R. C., Woods, R. E., & Masters, B. R. 2009, Digital Image Processing, Third Edition (Prentice Hall)
González-Pérez, J. N., Mittag, M., Schmitt, J. H. M. M., et al. 2022, Front. Astron. Space Sci., 9, 912546
Gosset, E., Royer, P., Rauw, G., Manfroid, J., & Vreux, J. M. 2001, MNRAS, 327, 435
Hall, J. C., Lockwood, G. W., & Skiff, B. A. 2007, AJ, 133, 862
Haugan, S. V. H., & Fredvik, T. 2020, ArXiv e-prints [arXiv:2011.12139]
Heck, A., Manfroid, J., & Mersch, G. 1985, A&AS, 59, 63
Hempelmann, A., Mittag, M., Gonzalez-Perez, J. N., et al. 2016, A&A, 586, A14
Isaacson, H., & Fischer, D. 2010, ApJ, 725, 875
Lovis, C., Dumusque, X., Santos, N. C., et al. 2011, ArXiv e-prints [arXiv:1107.5325]
Meunier, N. 2018, A&A, 615, A87
Mittag, M., Schröder, K. P., Hempelmann, A., González-Pérez, J. N., & Schmitt, J. H. M. M. 2016, A&A, 591, A89
Rauw, G., & Nazé, Y. 2021, MNRAS, 500, 2096
Schmitt, J. H. M. M., Schröder, K. P., Rauw, G., et al. 2014, Astron. Nachr., 335, 787
Schröder, K. P., Mittag, M., Pérez Martínez, M. I., Cuntz, M., & Schmitt, J. H. M. M. 2012, A&A, 540, A130
Shapiro, A. I., Solanki, S. K., Krivova, N. A., et al. 2014, A&A, 569, A38
Singh, J., Priyal, M., Ravindra, B., Bertello, L., & Pevtsov, A. 2023, RAA, 23, 045016
Sowmya, K., Shapiro, A. I., Witzke, V., et al. 2021, ApJ, 914, 21
Usoskin, I. G., Berdyugina, S. V., Moss, D., & Sokoloff, D. D. 2007, Adv. Space Res., 40, 951
Vaughan, A. H., Preston, G. W., & Wilson, O. C. 1978, PASP, 90, 267
Wilson, O. C. 1978, ApJ, 226, 379
Worden, J. R., White, O. R., & Woods, T. N. 1998, ApJ, 496, 998
Zhang, W., Zhang, J., He, H., et al. 2022, ApJS, 263, 12

Appendix A: Examples of synoptic map for the three broad maxima in Fig 8

The top panel of each figure display the evolution during several solar rotations of the segmented bright chromospheric structures (see Section 3.1). The bottom panels show the sum of bright pixels of vertical strips (explained in Section 4.1). The "CR" number above each synoptic map refers to the Carrington rotation number.

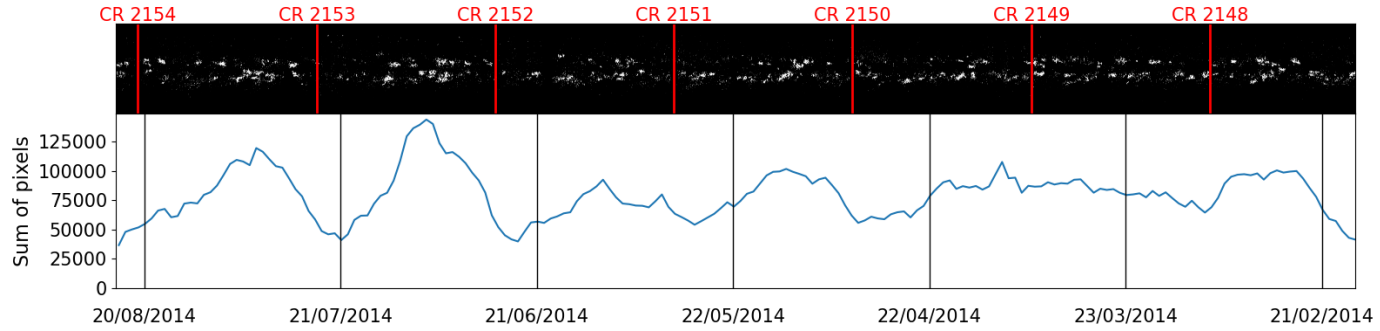

Fig. A.1. Synoptic map of the Sun centered around **May 22, 2014 (JD2456800)**

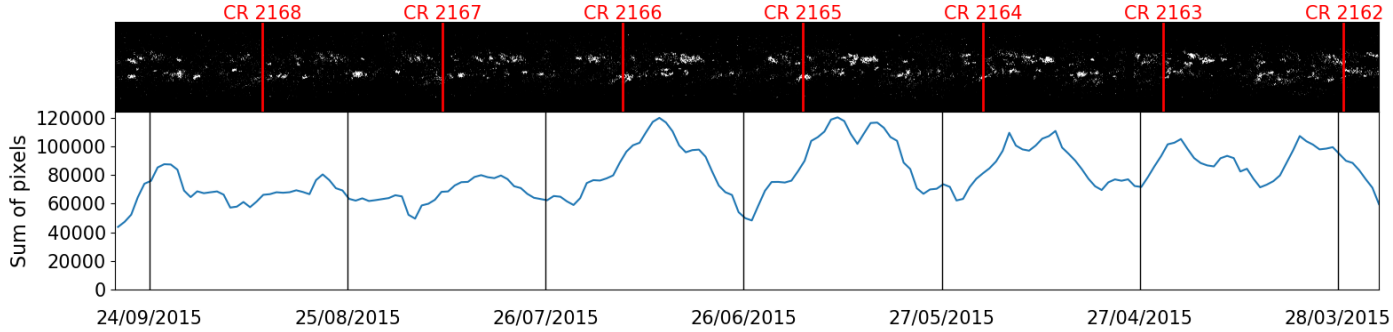

Fig. A.2. Synoptic map of the Sun centered around **June 26, 2015 (JD2457200)**

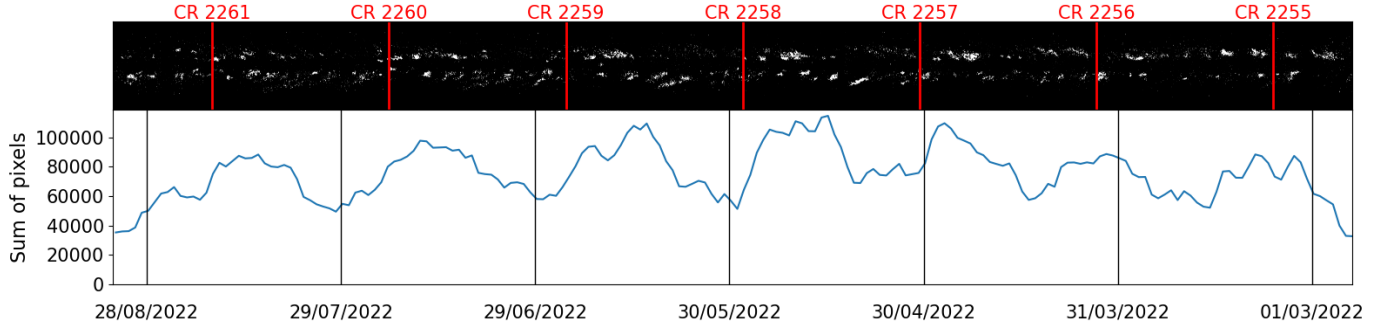

Fig. A.3. Synoptic map of the Sun centered around **May 30, 2022 (JD2459730)**

Appendix B: Examples of synoptic map for episodes lacking detection of a modulation during solar maximum

The top panel of each figure display the evolution during several solar rotations of the segmented bright chromospheric structures (see Section 3.1). The bottom panels show the sum of bright pixels of vertical strips (explained in Section 4.1). The "CR" number above each synoptic map refers to the Carrington rotation number.

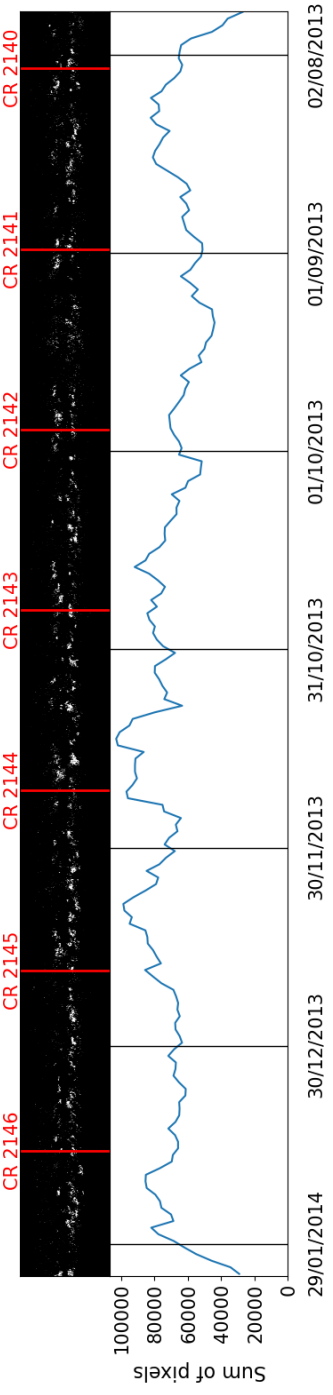

Fig. B.1. Synoptic map of the Sun centered around **October 31, 2013 (JD2456597)**

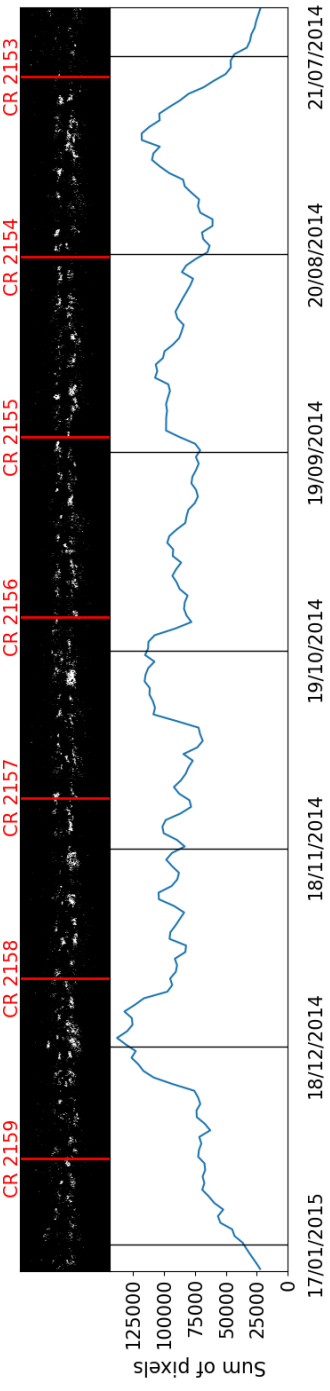

Fig. B.2. Synoptic map of the Sun centered around **October 19, 2014 (JD2456950)**

Appendix C: Example of synoptic map during the solar minimum

The top panel displays the evolution during several solar rotations of the segmented bright chromospheric structures (see Section 3.1). The bottom panel shows the sum of bright pixels of vertical strips (explained in Section 4.1). The "CR" number above each synoptic map refers to the Carrington rotation number.

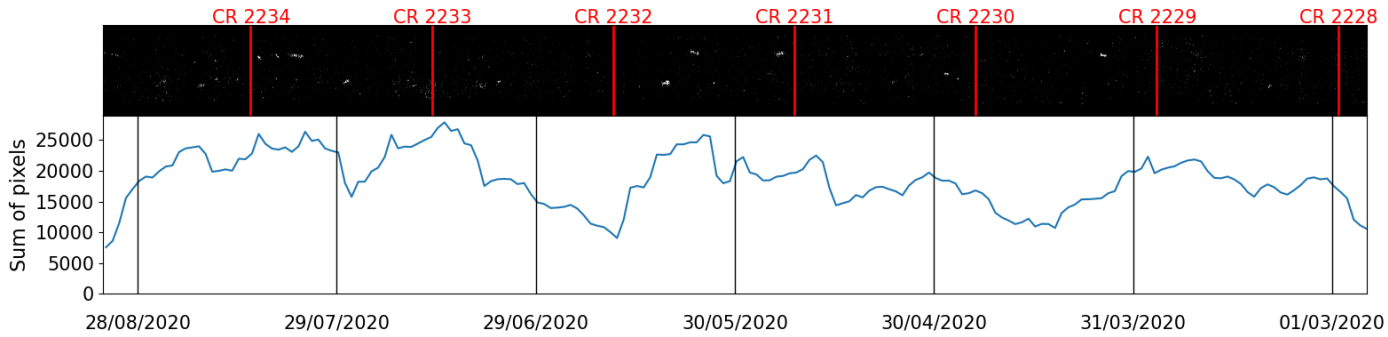

Fig. C.1. Synoptic map of the Sun centered around **May 30, 2020 (JD2459000)**

4.1 Complementary information

4.1.1 Increasing sliding windows in Fourier analysis

In Section 4.1. of Vanden Broeck et al. 2024a (paper above), we have analysed the properties of the modulation due to the solar rotation and studied their variation over the solar cycle. For this we have build a time-frequency diagram by computing a Fourier transform of the data. This analysis, illustrated in Figure 8 of the paper, has revealed that the rotational modulation is most prominently detectable near the maximum and the rising part of the cycle and essentially absent during solar minimum. We were wondering if using a larger sliding window could improve the detection of the solar rotation during the solar minimum. Therefore we have tried to build a diagram with sliding windows of 680 days, instead of 136 days, which is 5 times larger. The result is presented in Figure 4.1. We observe a spreading of amplitude peaks over time, and a narrowing in frequency. In other words, we gain better accuracy in pinpointing the peak's position, but the temporal resolution is degraded. However the overall behavior is consistent with the result obtained with smaller windows and we observe nothing significant during the solar minimum.

4.1.2 Contribution of the enhanced network

As seen in Figure 11 of Vanden Broeck et al. 2024a (paper above), at very low values (close to zero) of plages fraction coverage, A_P, there is a dispersion of the S-index. This is explained by the fact that when plages are decaying, they constitute the enhanced network and they become too small compared to plages, hence they are not segmented as plages. Indeed, while considering the EN in the segmentation process, the dispersion at very low fraction coverage disappears. Let's have a look at the fraction coverage of each structure in more details in Figure 4.2. It shows the temporal variation of the 13-month smoothed values of chromospheric structures fraction coverage: plages and enhanced network joined in red, plages only in blue and enhanced network only in green. We can notice that at the epochs of maximum solar activity, everything is normal in terms of amplitude of the variation. Plages area dominate over the enhanced network area. In that sense, the contribution of plages to the chromospheric emission is bigger than that of EN. However, EN contribution is not negligible. On the other hand, at the beginning of the solar minimum period, we note that the EN covers a larger portion of the solar disk than the plages. During this period, the contribution of the plages is not big and the EN is the main contributor to the chromospheric emission. Moreover, the variation of the enhanced network area fraction over the solar cycle is barely visible. In Section 1.2.2, we explained that some stars, called "flat activity" stars, exhibit no variation of their magnetic activity and are characterized by only a basal chromospheric flux which is comparable to the entirely inactive Sun. The origin of this basal flux, minimum level of chromospheric activity, is still under investigation. Therefore, the observations we presented above, and illustrated in Figure 4.2, suggest that the basal chromospheric flux could arise in the enhanced network.

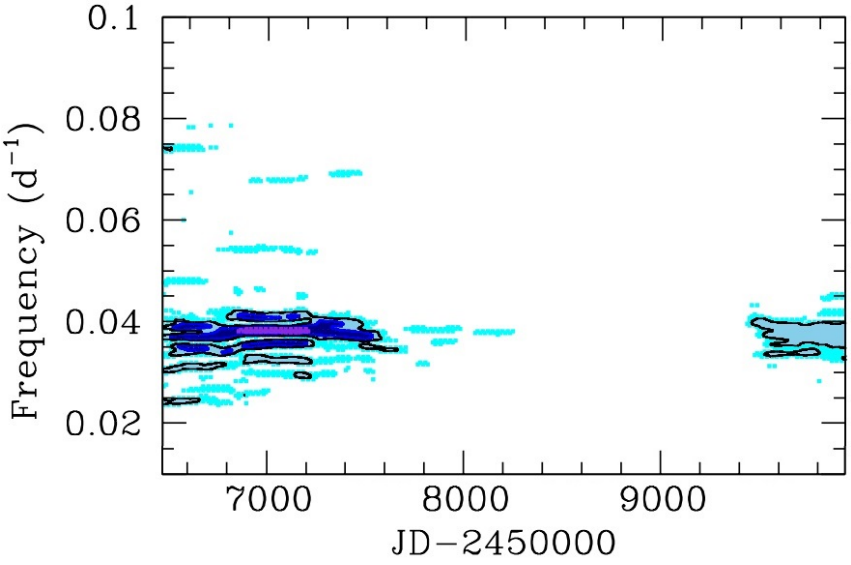

Fig. 4.1. Time-frequency diagram of A_{PEN} time series using sliding windows of 680 days. The panel provides the temporal evolution of the Fourier power spectrum. Violet, dark blue, light blue and cyan colors stand for power $\geq 8 \times 10^{-5}$, $\geq 4 \times 10^{-5}$, $\geq 2 \times 10^{-5}$, and $\geq 10^{-5}$.

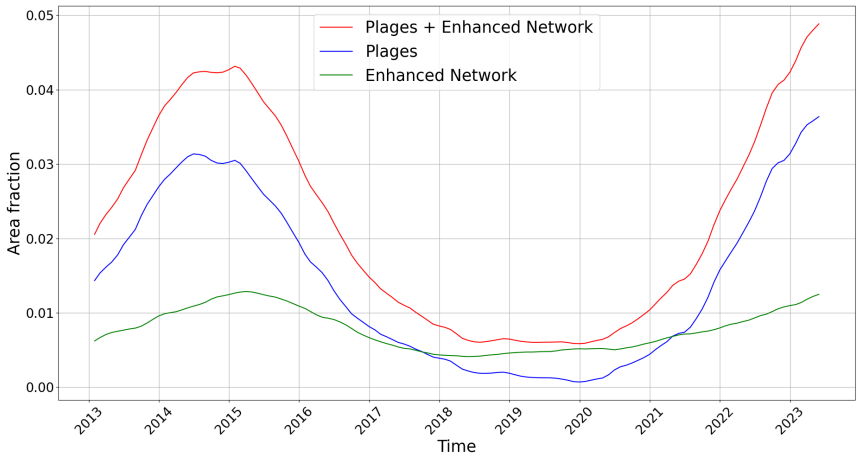

Fig. 4.2. Temporal variation of the 13-month smoothed values of the brigthest chromospheric structures fraction coverage: Plages and enhanced network joined (red), plages only (blue) and enhanced network only (green).

4.2 Perspectives

- First of all, the results we presented here were obtained based on USET Ca II K solar images. Those observations started twelve years ago, in July 2012, which spans a bit more than a solar cycle. We know that the amplitude of the cycles is not constant and varies from one to another. Consequently, our results can be broadened by studying other cycles using existing long-term datasets in Ca II K line and S-index. Some observatories provide a continuous record of observations over more than a century, for e.g. Coimbra, Kodaikanal, Meudon or

Mount Wilson, and many others over several decades. These archives are highly valuable to study the long-term solar activity and in that sense, to analyse the differences between cycles of diverse amplitudes.

- Although we have found a linear relationship between the disk-resolved index and the S-index, the dispersion around the fit is larger than the estimated uncertainties on the data. One possible explanation is the image quality and the presence of non-radial inhomogeneity affecting the segmentation process. Another potential source is the contribution of other moderately bright structures. The active network (AN) and the quiet network (QN) are part of the chromospheric network but do not correspond to regions of decaying plages, as the enhanced network. Despite their relative faintness, these structures might have a non-negligible contribution. Including those elements could help to reduce this dispersion. The segmentation of those structures can be performed using different intensity thresholds, as explained for e.g. in Worden et al. (1998); Priyal et al. (2019); Singh et al. (2021). But as they correspond to small-scale structures, the segmentation method must be improved to remove the non-radial inhomogeneities being unavoidably present on ground-based images. Finally, this dispersion can also be explained by the fact that the S-index includes the true contrast of the plages, which acts as a form of variable weighting of the area, while the USET area fraction does not include any contrast information (fixed uniform weighting).

- As illustrated in Figure 4.2, the enhanced network has a higher contribution than the plages during the solar minimum and its area fraction variation over the solar cycle is barely visible. This phenomenon may draw attention to the origin of the basal chromospheric flux observed in flat activity stars. We would therefore need more extended datasets to study the behavior of the enhanced network on a much longer timescale.

- When we want to study stars other than the Sun, we realize that they are observed at unknown inclinations. Observing the Sun yields results based on an equatorial view of the star. This perspective allows us to analyse specific data on its dynamics and the distribution of magnetic features on its surface. Consequently, the analysis are influenced by this orientation. In our work, we were wondering whether stars observed under a different viewing angle would also show the rotational modulation. For this, based on our Ca II K solar images, we must generate masks of the Sun viewed under different inclinations and compute the area fraction for those inclinations. We will have then an area fraction time series for every inclination and we will study the variation between those time series. This exploration is the topic of our second paper, described in the next Chapter.

Chapter 5

The Sun observed under different inclinations

Studying the magnetic activity in solar-type stars is essential to understand the dynamic processes that govern their atmospheres. The previous sections showed that the magnetic activity can be analysed in the chromospheric layer through observations in the Ca II K line, revealing structures like the bright plages and the enhanced network, which are regions of hotter plasma and concentrations of intense magnetic fields. We have shown in our first analysis that the area fraction of those features is a very good proxy for the S-index, which is widely used in astrophysics to study the magnetic activity of stars. Based on data obtained over the same time interval and for observations made on the same dates, a strong linear relationship was found between the indices (Vanden Broeck et al. 2024a). This correlation allows us to use the area fraction of plages and enhanced network to generalize the results obtained for the Sun to the population of solar-type stars. However, a critical factor challenging the interpretation of these observations is the inclination of the stellar rotation axis relative to the observer's line of sight. Indeed, this inclination is random and most of the time unknown. It is crucial to evaluate the effect of the viewing angle on the observed magnetic activity to compare solar variability with that observed in other Sun-like stars. This impact of the viewing angle was already investigated mainly on synthetic images of the Sun using numerical simulations (Schatten 1993; Knaack et al. 2001; Shapiro et al. 2014; Nèmec et al. 2020; Sowmya et al. 2021b,a). In our work, we have studied the influence of the inclination on the temporal modulations of the area fraction of plages and enhanced network through real solar observations with our archives of USET Ca II K images.

As the Sun is observed from a near-equatorial perspective, if we want to study the effect of the inclinations of the rotation axis, we must produce solar images as seen under different viewing angles. For this purpose, we first segment the brightest structures of the chromosphere (plages and enhanced network) using the segmentation method explained in Section 3.2.1.2. We end up with binary images, called solar masks, with pixels equal to 1 corresponding to the features and pixels equal to 0 for the rest. To reproduce solar views under different inclinations, we need to map the

entire solar surface during a complete solar rotation to reconstruct the distribution of structures over the full 360° range of solar longitudes. After projecting the solar sphere into a Cartesian representation, we apply our method, described in Section 3.3.2, to create segmented synoptic maps of the Sun allowing us to observe the distribution of plages and enhanced network during a solar rotation. Based on those maps, by specifying the central latitude and longitude of the map, we generate solar masks for any inclination angles (see Figure 3.26) that simulate how the Sun would appear if observed from those angles. Finally, we extract the area fraction of plages and enhanced network for each generated solar masks to create time series for any desired inclination. In this work, we have performed this process for inclinations $i = -90°$ (South Pole-on view) to $i = 90°$ (North Pole-on view) by steps of 10°.

Since plages are primarily distributed between the Equator and mid-latitudes, the closer we get to a Pole-on view, the less we observe the structures at the center of the disk (see Figure 3.26). Under such inclinations, the plages will be observable close to the limbs and their area will be reduced so that the variation in the area fraction will be smaller. To study the effect of the inclination, we use Fourier power spectra to search for the presence of periodic modulations, in particular the solar cycle of $\sim$ 11 years and the solar rotation of $\sim$ 27.27 days. The occurrence of a periodic signal generates a peak in the power spectrum at the associated frequency. To produce such a rotation modulation, one needs to have an inhomogeneous distribution of the active regions in longitudes, otherwise the signal will remain constant. Figures 5.1 and 5.2 illustrate an example of solar masks viewed from the Equator and from the North Pole during a complete solar rotation. Let's consider that the presence of an active region is equal to 1 and the absence of active region is equal to 0. In the perspective of the Equator-on view (Figure 5.1), there are periods when no active regions are visible at the beginning (value = 0). As the solar rotation progresses, the active region becomes visible (value = 1), and then it disappears a few days after (value = 0). This variation of 0 and 1 indicates a periodical modulation on the timescale of the rotation of the solar disk. In contrast, for the North Pole-on view (Figure 5.2), the active region is constantly visible at the limb during the entire solar rotation (value = 1). Since the active region does not disappear, except during its decay, there is no modulation in the signal. This results in a constant value of 1, indicating a lack of variation over time.

Therefore, the signal of rotational modulation becomes harder to detect as the inclination angle approaches a Pole-on view. In that sense, using the active regions fraction coverage, we can consider that a star observed from Earth, as seen from its North or South Pole, will fail to reveal its rotation period in the Fourier spectrum. We may wonder up to what inclination angle does the detection of the rotation period remain possible? Moreover, is this behavior similar for the solar cycle period? As outlined in Section 1.2.2, many observations indicate that Sun-like stars exhibit other forms of variability in their activity (periodic, non-periodic and quasi-periodic cycles). A natural question is whether this disparity in the activity cycles can be due to the inclination of the rotation axis of the star? This work tries to answer those questions.

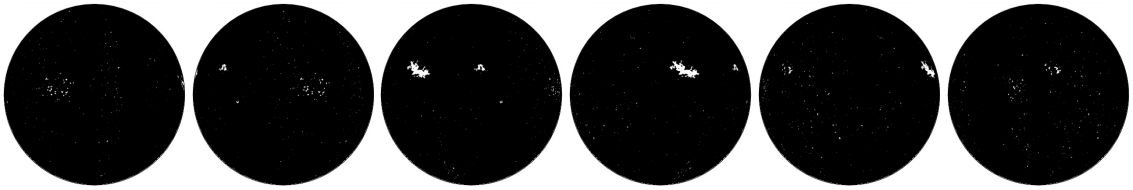

Fig. 5.1. Example of active region distribution on the solar disk during a solar rotation viewed from the Equator. The successive solar masks are separated by a few days. In the first and second masks, the active region is still not present. It appears in the third mask, then remains visible during a half rotation period and disappears between the ultimate and penultimate masks.

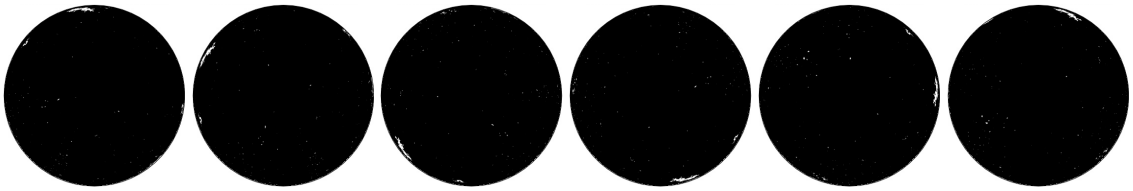

Fig. 5.2. Example of active region distribution on the solar disk during a solar rotation viewed from the North Pole. The successive solar masks are separated by a few days. The active region remains visible at the limb during the entire solar rotation cycle.

However, it is important to highlight that solar observations and stellar observations differ strongly on their sampling. While the USET Ca II K observations of the Sun benefit from a denser sampling thanks to a rather constant monitoring during the whole year, actual time series of stellar observations have usually more complicated and scarcer samplings, restricted to periods of typically six months due to restrictions on the visibility of the star. In addition, whilst USET is fully dedicated to observations of the Sun, telescopes used for the study of chromospherically active stars usually have to share the observing time between a number of targets, resulting in a lower cadence of observations than for the USET data. The impact of the sampling of the time series is therefore also analysed in our study. We retrieve more realistic scarcer samplings of the TIGRE observations of solar-like stars and we apply those types of sampling to the USET time series.

The following paper was submitted in Astronomy & Astrophysics for publication and is currently under revision. The first feedback from the reviewer has already been received, and the required corrections have been implemented. The paper is available on arXiv following this link: https://arxiv.org/abs/2410.11335

Astronomy & Astrophysics manuscript no. article
October 16, 2024

How does the solar chromospheric activity look like under different inclination angles?

G. Vanden Broeck[1,2], S. Bechet[1], G. Rauw[2], and F. Clette[3]

[1] Department of Solar Physics and Space Weather, Royal Observatory of Belgium (ROB), Av. Circulaire 3, 1180 Uccle, Belgium
email: gregory.vandenbroeck@observatory.be
[2] Space sciences, Technologies and Astrophysics Research (STAR) Institute, Université de Liège, Allée du 6 Août, 19c, Bât B5c, 4000 Liège, Belgium
[3] Institut d'Astronomie et d'Astrophysique (IAA), Université Libre de Bruxelles, CP 226, Boulevard du Triomphe, 1050 Bruxelles, Belgium

October 16, 2024

ABSTRACT

Context. Chromospheric observations in the Ca II lines are essential to study the magnetic activity of stars. The chromospheric plages, main contributors to the Ca II K emission, are distributed between mid-latitude and the Equator and never close to the Poles. Therefore, we suspect that the inclination angle of the solar rotation axis has an impact on the observable chromospheric emission. Until now, the effect of such inclination on chromospheric emission has not been extensively studied through direct solar observations.
Aims. We reproduce the solar images from any inclination in order to study the effect of the inclination axis on the solar variability by using direct observations of the Sun in the Ca II K line. In the context of the solar/stellar connection, while the Sun is observed from Earth from its near-Equator point of view and the others stars are observed most of the time under unknown inclinations, our results can improve our understanding of the magnetic activity of other solar-type stars.
Methods. More than 2700 days of observations since the beginning of the Ca II K observations with USET, in July 2012, were used in our analysis. For each observation day, we produce synoptic maps to map the entire solar surface during a full solar rotation. Then by choosing a given inclination, we generate solar-disk views, representing the segmented brightest structures of the chromosphere (plages and enhanced network), as seen under this inclination. The area fraction are extracted from the masks for each inclination and we compare the evolution of those time series to quantify the impact of the inclination angle.
Results. We find a variation of the area fraction between an Equator-on view and a Pole-on view. Our results show an important impact of the viewing angle on the detection of modulation due to the solar rotation. With the dense temporal sampling of USET data, the solar rotation is detectable up to an inclination of about $|i| = 70°$ and the solar-cycle modulation is clearly detected for all inclinations, though with a reduced amplitude in polar views. When applying a sparse temporal sampling typical for time series of solar-like stars, the rotational modulation is no longer detected, whatever the inclination, due entirely to the under-sampling. On the other hand, we find that the activity-cycle modulation remains detectable, even for Pole-on inclinations, as long as the sampling contains at least 20 observations per year and the cycle amplitude reaches at least 30% of the solar-cycle amplitude.
Conclusions. The inclination of the rotation axis of stars relative to our line of sight is most of the time unknown. Based on solar observations, we have shown that the impact of this inclination is important on the detection of the rotation period but negligible on the detection of the activity cycle period. For other stars, the time series have usually more complicated and scarcer samplings due to restricted target visibility and this leads to a decrease of the signal of the chromospheric activity cycle. However, our results suggest that the inclination is unlikely to be the primary factor contributing to the relative scarcity of well-established cycles.

Key words. Sun: activity - Sun: chromosphere - Sun: faculae, plages - stars: activity - stars: solar-type

1. Introduction

Chromospheric activity of a large number of stars is monitored in the Ca II K and H lines (Radick et al. 2018; Boro Saikia et al. 2018; Mittag et al. 2023). Over the past sixty years, significant progress has been made in the study of cool stellar chromospheres. It started in 1966 with the Mount Wilson HK project (Wilson 1978), recording chromospheric measurements of approximately 2.000 Sun-like stars. Understanding how the Sun compares to Sun-like stars in terms of variability and magnetic activity cycles can provide profound insights into the mechanisms driving stellar magnetic activity. The Mount Wilson HK project led to the creation of the Mount Wilson S-index, defined as the ratio of the total flux in the Ca II K and H line cores to the total flux in two pseudo-continuum regions located near the K and H lines. This index is widely used to study the magnetic activity of stars. In particular the stellar cycle and rotation can be calculated based on the detection of temporal modulations in the time series of the S-index (Hempelmann et al. 2016). For instance, the Mount Wilson monitoring program demonstrated that the Sun is not unique in exhibiting periodic activity cycles (Baliunas et al. 1998): such behavior is common among solar-like stars (60% of the Wilson's sample stars). However, some studies have demonstrated that most Sun-like stars (with age, mass, temperature and chromospheric activity similar to the Sun) exhibit different photometric variability on the activity cycle timescale than the Sun (Lockwood & Skiff 1990; Lockwood et al. 2007; Reinhold et al. 2020). The impact of the viewing angle on the solar irradiance variability was first proposed by Schatten (1993). Indeed, the magnetic structures are distributed

between the Equator and mid-latitudes and the position of the observer relative to the rotation axis affects their brightness contrasts. While stars are usually observed without information on their inclinations, it is crucial to quantitatively evaluate this dependence to understand how solar variability is comparable to other Sun-like stars.

The rotation periods of stars were successfully estimated from S-index time series, but no correction for the effect of inclination on the observed level of variability was applied (Vaughan et al. 1981; Noyes et al. 1984; Baliunas et al. 1985; Wright et al. 2004). More recently, Radick et al. (2018) studied the variation of the chromospheric emission of the Sun and other Sun-like stars but they also did not apply a correction for the effect of inclination. The impact of the viewing angle on the observable magnetic activity of the Sun has been mainly studied based on synthetic images of the Sun obtained with rather simplified models and numerical simulations (Schatten 1993; Knaack et al. 2001; Shapiro et al. 2014; Borgniet et al. 2015; Meunier et al. 2019, 2024; Nèmec et al. 2020; Sowmya et al. 2021). For example, Shapiro et al. (2014), Knaack et al. (2001) and Sowmya et al. (2021) analysed the influence of the inclination on solar irradiance and chromospheric activity by using physics-based model to calculate relative flux variations. Borgniet et al. (2015) and Meunier et al. (2019) presented similar studies but using times series of radial velocity, chromospheric emission and photometry to analyse the effects of activity (via spots, faculae and inhibition of convective blueshift) on exoplanet detectability. Those studies showed through simulations of different inclinations that the inclination of the stellar rotation axis has a strong impact on those time series. Here we propose to study this impact on the determination of the temporal modulations through real solar observations in the Ca II K line.

Ground-based solar observations allow to see the surface of one side of the Sun, the far-side of the Sun being not observable. However, based on images recorded during a full solar rotation, we can map the entire solar surface into a synoptic map. Then by an appropriate projection, we can generate images of the Sun for various viewing angles. Finally we can build time series for different inclinations and study the impact of inclination axis on the detection of modulations. More specifically we consider the effect on the time series of the plages and enhanced network area fraction in the Ca II K line.

Indeed it has been shown that those structures are the main cause of the modulation in the Ca II K emission and their area fraction is a good proxy for the S-index. Using Ca II K images with USET (Uccle Solar Equatorial Table) and S-index collected from TIGRE (Telescopio Internacional de Guanajuato Robotico Espectroscopico), Vanden Broeck et al. (2024) compared the area fraction of plages and enhanced network with the S-index based on data obtained over the same time interval and for observations made on the same dates. As seen in Fig. 1, they found a linear correlation between the indices, described by the following equation:

$$A_{PEN} = (3.55 \pm 0.06)\, S_{\mathrm{MWO}} - (0.57 \pm 0.01) \quad (1)$$

where A_{PEN} is the area fraction of the plages and enhanced network from USET images, and S_{MWO} the solar S-index from TIGRE in the Mt. Wilson scale. Since a well-defined linear transformation was found to convert the S-index from TIGRE to the Mount Wilson scale (Mittag et al. 2016), the area fraction of plages and enhanced network offers a reliable diagnostic of chromospheric activity. This area fraction can then be used to generalize the results obtained for the Sun to the population of Sun-like stars.

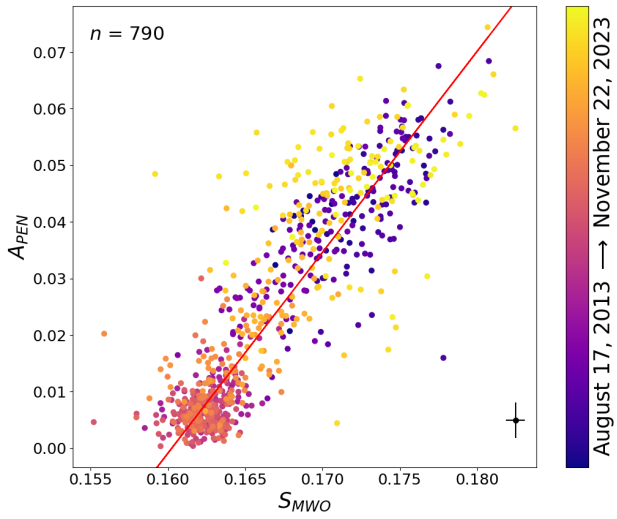

Fig. 1: Correlation between daily values of the solar S-index from TIGRE (in the Mount Wilson scale) and the USET area fraction of plages and enhanced network, A_{PEN}. The parameter n represents the number of data, and the chronological order is color-coded. The first and last date of the data are given next to the color bar. Additionally, a linear fit was performed to the data (red solid line). A mean error bar is displayed on the bottom right corner to have an idea of the uncertainties on the data. Image taken from Vanden Broeck et al. (2024).

Section 2 briefly describes the instrument and data used for our analysis. In section 3, we explain the method of data processing: the segmentation of the chromospheric structures, the creation of the synoptic maps and the production of the solar-disk views under different inclination angles. Our results about the detection of the temporal modulation for various inclinations are presented in section 4. Finally, we summarize and discuss our results in section 5.

2. Dataset

In this study we use the synoptic images acquired by the USET station (Uccle Solar Equatorial Table) from the Royal Observatory of Belgium (ROB), located in Uccle, South of Brussels (Bechet & Clette 2002). Synoptic images are appropriate for this study as the full-disk images cover the whole surface of the Sun which is needed to map the entire solar surface. In particular we consider the full-disk daily images in the Ca II K line. The dataset covers a long time period, from July 11, 2012 to November 28, 2023, thus spanning 11.38 years, which is requested to search for long temporal modulations. After performing an automatic quality selection to keep the best image recorded per day (Vanden Broeck et al. 2024), the resulting series consists of 2725 images, covering more than 70% of the analysed period.

In addition, the station carries three other solar telescopes (White-Light, 656.3 nm H-alpha and sunspot drawings) to monitor simultaneously the photosphere and the chromosphere. The averaged total number of observation days is 260 per year. The gaps are essentially due to bad weather conditions.

The optical set-up consists in a refractor of 925 mm focal length and 132 mm aperture. The filter is thermo-regulated and its central wavelength is λ = 3933.67Å, with a bandwidth of

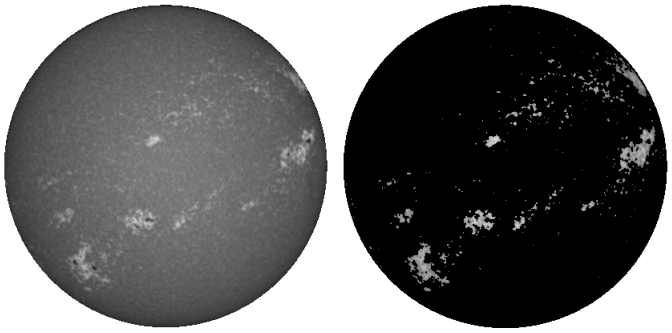

Fig. 2: Example of the segmentation process. Left: recentered raw image from the 29th of October 2013. Right image: result of the segmentation.

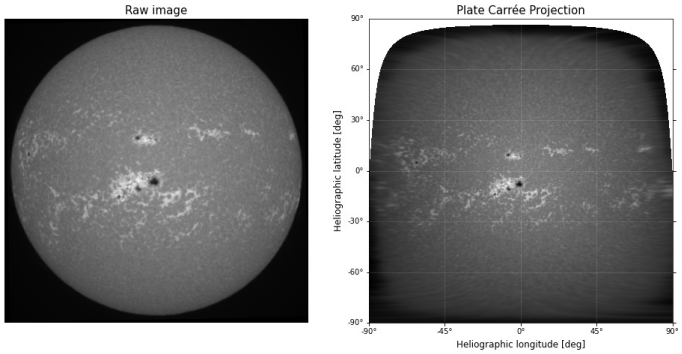

Fig. 3: Example of a CAR projection. Left: Raw solar image. Right: The corresponding image after the projection.

2.7Å. The images are acquired with a 2048 × 2048 CCD with a dynamic range of 12 bits. The instrumental set-up is the same since 2012, except for the introduction of an additional neutral filter on July 10, 2013. The acquisition cadence can go up to 4 frames per second in case of transient events to record, and the daily synoptic cadence is 15 minutes.

3. Data processing

After correcting the raw USET Ca II K images for instrumental and atmospheric effects, we segment the brightest chromospheric features to generate binary masks. Then, using successive daily disk masks, we assemble synoptic maps covering each a full Carrington rotation, thus mapping the whole solar surface. We can then apply a spherical projection to those synthetic maps to create solar-disk views reproducing the projected area of bright chromospheric structures as seen under different inclinations of the rotation axis relative to the line of sight. Finally, by summing those apparent areas over the full disk for each date, we create a time series of the total area fraction spanning the duration of the USET dataset.

In the next sections, we define the inclination as the angle between the solar Equator and the observer's line of sight. The Equator-on view refers to an inclination $i = 0°$ while the Poles-on view correspond to an inclinations $i = 90°$ for the North Pole-on view and $i = -90°$ for the South Pole-on view.

3.1. Chromospheric structures segmentation

The solar chromosphere exhibits various structures that differ in size and brightness. In this study, we have segmented the brightest structures, namely the plages, which are the chromospheric counterparts of the faculae, and the enhanced network, considered as small regions of decaying plages (Singh et al. 2023). More details on this segmentation method can be found in Vanden Broeck et al. (2024) and an example of this process is shown in Fig. 2.

3.2. Synoptic segmented map construction

To map the entire solar surface, a projection is needed to convert spherical coordinates (latitude and longitude) into a flat representation. For this, we use the Plate Carrée (CAR) projection where the meridians and the parallels are equally spaced, forming a grid of squares from East to West and from North to South. With this projection, it is particularly easy to associate the heliographic coordinates of a structure on the Sun to its position in pixels on the map (Calabretta & Greisen 2002). Fig. 3 shows an example of the CAR projection of a solar image. The white part of the image is due to the fact that the rotation axis of the Sun is tilted with respect to the ecliptic. This tilt goes from −7.25° to 7.25°. Therefore, except when this inclination is equal to 0°, there is always a small hidden area around either the North or the South Pole. Those parts of the images are filled with zero values.

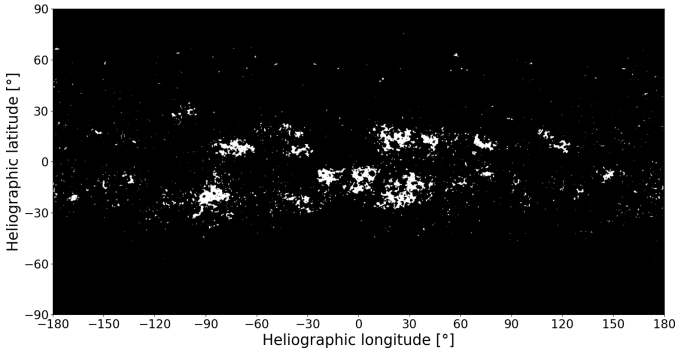

Fig. 4: Example of a segmented synoptic map build around the 7th of July 2014 illustrating the distribution of the plages and enhanced network during a full solar rotation. The x-axis represents the number of degrees of longitudes from the Carrington longitude on 7th of July 2014 (center of the image).

A synoptic map is made of consecutive strips from successive solar images, spanning a whole solar rotation. In each image, the strip is centered on the central meridian and its pixel size corresponds to a time interval depending on the observing time of the previous and the following available images. This process is applied for each day of the dataset. Finally, by doing a calculation for the boundary conditions to build a map of 180° before and 180° after a given day, we get a synoptic map representing the entire surface of the Sun around this given date (see Fig. 4).

3.3. Reconstructed solar-disk views for different inclinations

For each observed date in the original USET series, using the corresponding whole-Sun segmented synoptic map, we create solar-disk views at different inclinations by using an orthographic projection with various centers. In particular we specify the central latitude and longitude in the orthographic function from the Cartopy library, designed for cartographic projection and geospatial data visualization (Met Office 2010 - 2015). The generation of solar-disk views is illustrated in Fig. 5 for inclina-

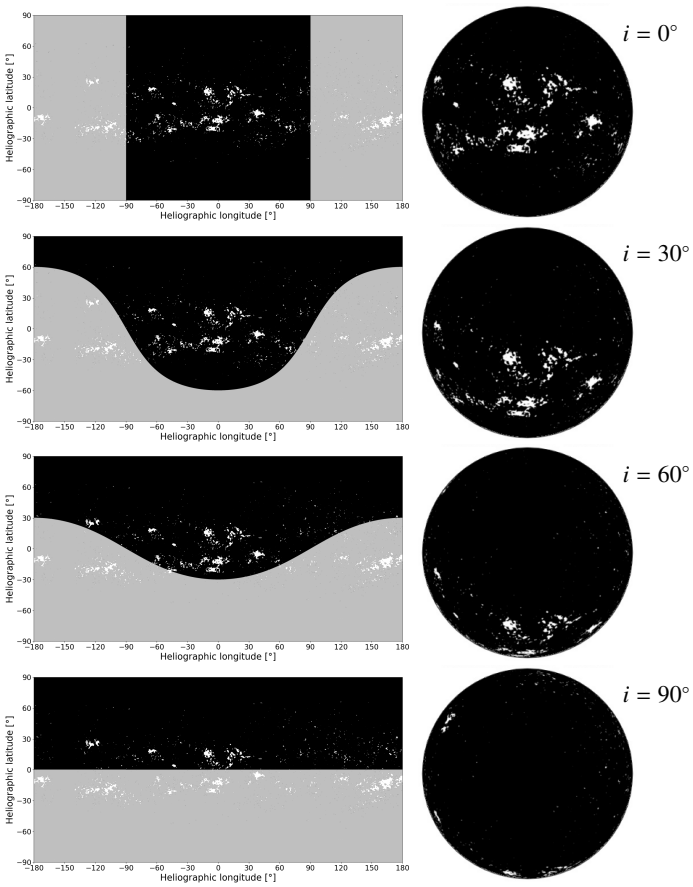

Fig. 5: Generation of solar-disk views for different inclination angles, indicated in the upper right corner of the panels and representing the number of degrees relative to the Equator-on view (inclination of 0°). Left: Synoptic map illustrating the distribution of the entire solar surface around the 8th of June 2014. The shaded areas (grey part) mark the far-side of the Sun. Right: The corresponding solar-disk. Inclination of 90° corresponds to the Sun's North Pole-on view.

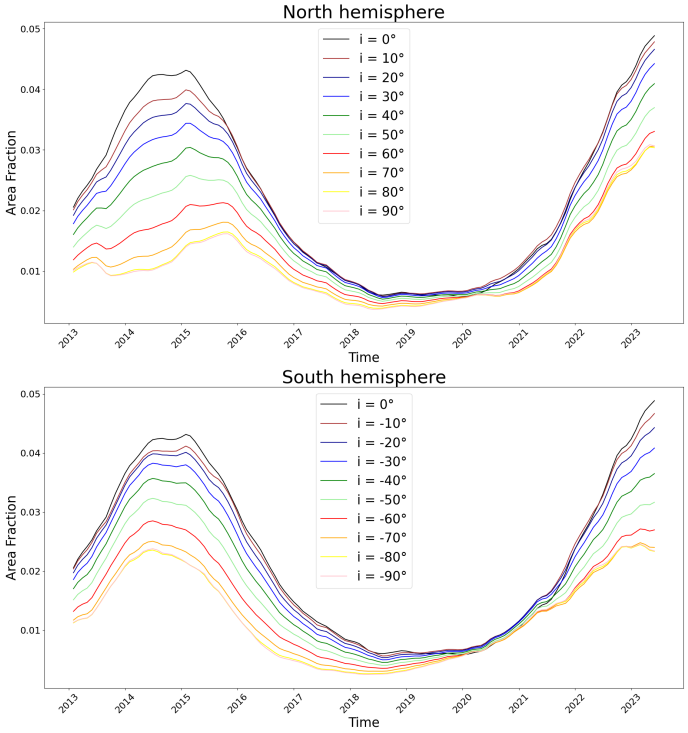

Fig. 6: Evolution of plages and enhanced network area fraction for different inclinations. Top panel: Inclinations from the Equator-on view ($i = 0°$ of latitude) to the North Pole-on view ($i = 90°$ of latitude). Bottom panel: Inclinations from the Equator-on view to the South Pole-on view ($i = -90°$ of latitude). The data are the monthly averaged data smoothed with a 13-months sliding window. The colors stand for different inclinations.

tions i of 0°, 30°, 60° and 90° (from the Equator-on view to the North Pole-on view). Appendix A provides the generated solar-disk views for all the inclinations from the North Pole-on view to the South Pole-on view. The gray areas on the synoptic maps in Fig. 5 represent the far-side of the Sun. The chromospheric plages are distributed up to 50° of latitude relative to the Equator (Devi et al. 2021). Therefore, as we move to a Pole-on observation, those structures will be distributed closer to the limbs which makes them appear smaller.

3.4. Temporal evolution of the area fraction for different inclinations

Based on those generated solar-disk views (Fig. A.1), we build temporal series for each inclination by extracting the area fraction of the plages and enhanced network, called A_{PEN} following the method described in Vanden Broeck et al. (2024). For the whole USET dataset, we derive the area fraction for various inclinations from the Equator-on view ($i = 0°$ of latitude) to the Pole-on view ($i = 90°$ and $i = -90°$) as represented in Fig. 6. The plotted data are the monthly averaged data smoothed with a 13-months sliding window. There is an obvious lower peak-to-peak amplitude in the modulation of the area fraction when we move away from the Equator-on point of view, in both hemispheres. At the minimum of the solar cycle, the variation of A_{PEN} between the Equator-on view and the Poles-on view is not significant. However, at the maximum, this variation is of 63% between the Equator-on and North Pole-on views, and 45% between the Equator-on and the South Pole-on views. This is related to the apparent projected area of magnetic structures that are reduced by the foreshortening as observed from the Poles. Despite the large change in amplitude at solar cycle maximum, the modulation associated with the solar cycle remains observable for both the North and South Pole-on views. In the next section, we will analyse quantitatively the impact of this variation on the detection of the temporal modulations.

In addition, we observe that the curves for the two hemispheres peak at different times. Top panel of Fig. 7 shows the A_{PEN} time series for the polar view for each hemisphere. For the Southern hemisphere (red curve), the solar maximum is clearly visible around mid-2014 while for the Northern hemisphere, the solar maximum happens later, at the end of 2015. It is well known that the solar activity presents significant asymmetries. It has been studied in detail in a variety of observations and activity indices, such as sunspot groups and areas, sunspot numbers, but also on plages and flare occurrence (El-Borie et al. 2021; Veronig et al. 2021). The panels in Fig. 7 indeed show that, when separating the solar hemispheres, our time series of plages and enhanced network area fraction follow the same long-term evolution as the photospheric Sunspot Number, with the same variations of the North-South asymmetry. In section 4, we will see

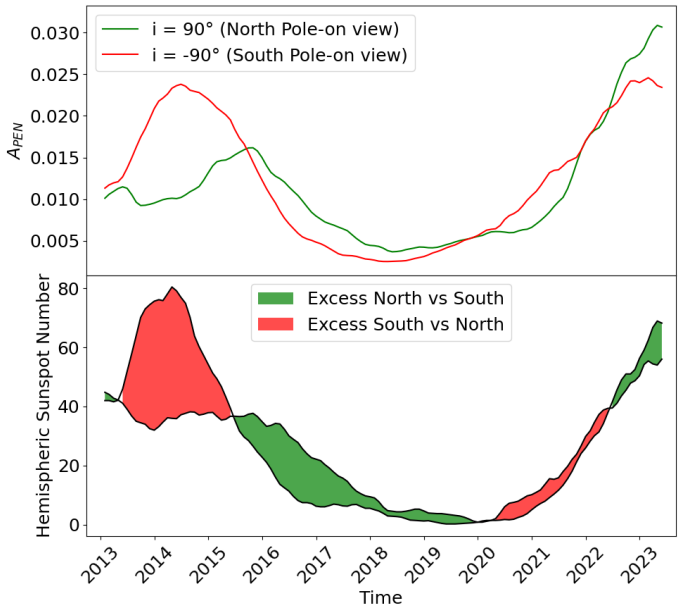

Fig. 7: Top panel: Comparison between the area fraction of plages and enhanced network, A_{PEN}, seen from the Northern hemisphere (green) and from the Southern hemisphere (red). The curves are the monthly averaged data smoothed with a 13-month sliding window. Bottom panel: International Sunspot Number, hemispheric 13-month smoothed number. Green parts represent an excess of activity in the Northern hemisphere while red parts represent an excess in the Southern hemisphere. Credit: SILSO (Royal Observatory of Belgium).

that a corresponding asymmetry is naturally also found in the effects of inclination on our solar reconstructions.

4. Detection of temporal modulations out of the ecliptic

In this section we analyse the time series of A_{PEN} for various inclinations more quantitatively. In particular we use Fourier power spectra to look for the presence of periodic modulations on the solar cycle and solar rotation timescale. The discrete Fourier power spectrum method of Heck et al. (1985) and Gosset et al. (2001) was applied to each of the time series extracted for the 19 values of inclinations from $i = -90°$ to $i = +90°$ in steps of 10°. This Fourier methodology explicitly accounts for the uneven temporal sampling of astronomical time series such as those analysed here. To assess the significance level of the peaks in the power spectrum, we used a bootstrapping method where the times of observations were kept fixed and the measured area fractions were redistributed randomly among the times of observations. For each reshuffled time series we computed a power spectrum and determined the highest value of the power. The reshuffling process was repeated a thousand times for each inclination. The distribution of the highest peaks in the power spectra was used to determine the threshold corresponding to a 99% significance level, that is, 1% of the power spectra of the reshuffled time series have a higher power than this threshold.

Fig. 8 illustrates the Fourier power spectrum for an inclination of $i = 0°$. The Fourier power spectra for the other inclinations are provided in appendix B. As one can see, the strongest peak in the power spectrum occurs at low frequencies and is due to the long-term variations resulting from the 11-year solar cycle. Secondly, there are a group of peaks close to the Carrington rotation frequency ν_{Car}, indicated by the dashed green line, associated with the solar rotation.

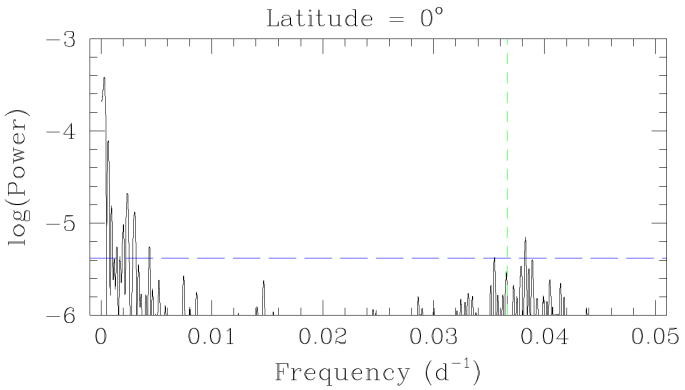

Fig. 8: Fourier power spectrum of the fractional area of the plages and enhanced network in the case of an inclination $i = 0°$ (Equator-on view). The panel illustrates the power spectrum over the frequency range between 0 and 0.05 d^{-1}. The green dashed line yields ν_{Car}, the frequency associated with the Carrington rotation period. The long-dashed blue horizontal line yields the 99% significance level.

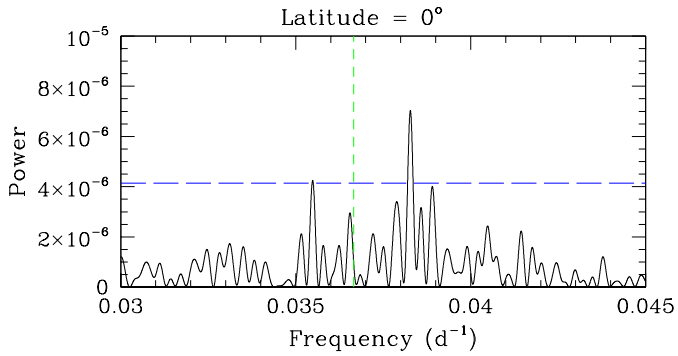

Fig. 9: Fourier power spectrum zoomed on the rotation frequency in the case of a view with an inclination $i = 0°$ (Equator-on view). The panel illustrates the power spectrum over the frequency range between 0.03 and 0.045 d^{-1}. The green dashed line yields ν_{Car}, while the long-dashed blue horizontal line yields the 99% significance level.

4.1. Effect on the detection of the solar rotation

In order to study the solar rotation detection, we consider a zoom close the Carrington frequency ν_{Car} as illustrated in Fig. 9 for the view in the Equator plane. The other inclinations are shown in the appendix C by steps of 10°. First of all, for every inclination but essentially in the Northern hemisphere (positive inclinations), multiple peaks are detected close to ν_{Car}, the highest power being recorded at a frequency of 0.0383 d^{-1} (period of 26.1342 d), near the frequency of the equatorial synodic rotation period.

The highly complex structure of the peaks around the rotational frequency reflects the finite lifetime of the modulations which were most prominently seen during three distinct episodes of our USET time series (see Vanden Broeck et al. 2024). This finite lifetime leads to a beating between the actual rotational

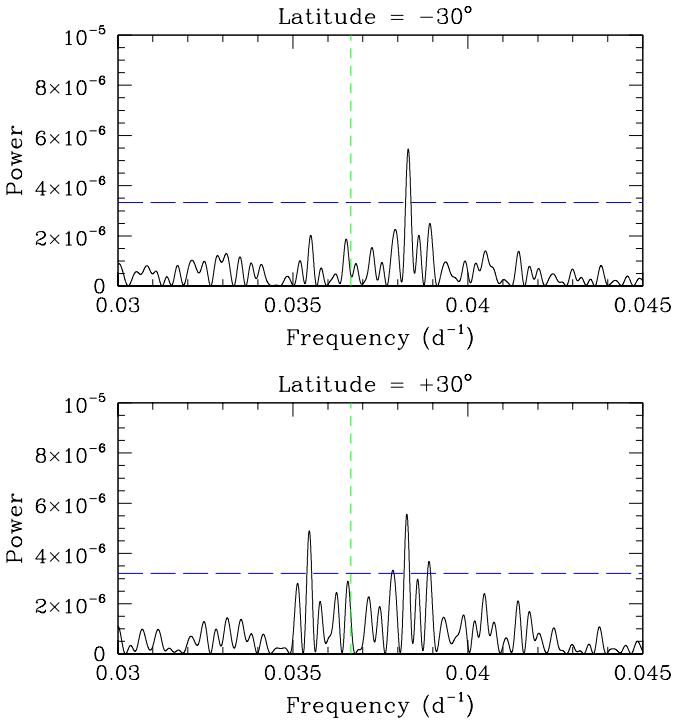

Fig. 10: Fourier power spectrum zoomed on the rotation frequency in the case of a view with an inclination $i = -30°$ (top) and $i = 30°$ (bottom). The panel illustrates the power spectrum over the frequency range between 0.03 and 0.045 d^{-1}. The green dashed line yields ν_{Car}, while the long-dashed blue horizontal line yields the 99% significance level.

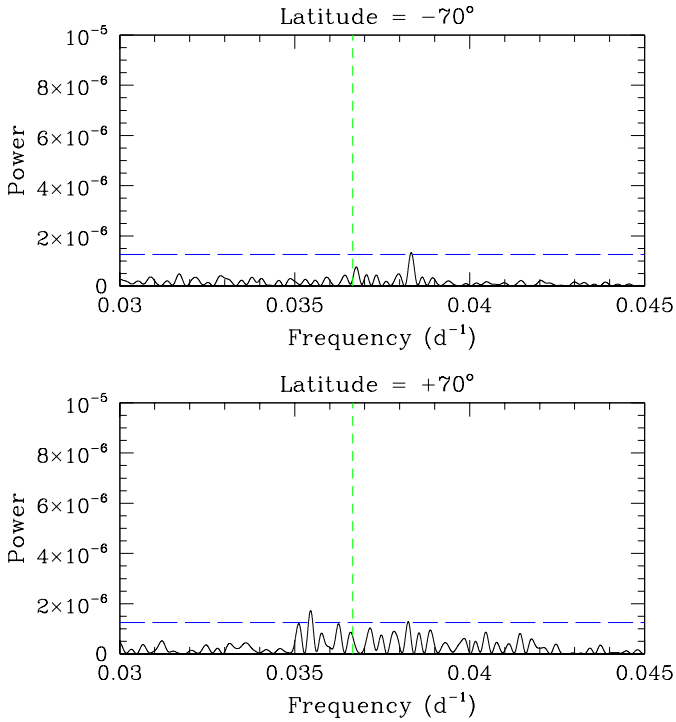

Fig. 11: Fourier power spectrum zoomed on the rotation frequency in the case of a view with an inclination $i = -70°$ (top) and $i = 70°$ (bottom). The panel illustrates the power spectrum over the frequency range between 0.03 and 0.045 d^{-1}. The green dashed line yields ν_{Car}, while the long-dashed blue horizontal line yields the 99% significance level.

period and the characteristic times corresponding to the separation between consecutive episodes over which the rotational modulation is observed. In addition, shifts in phase between the modulations at these different epochs play a role in the relative strengths of the various subpeaks of the structure.

Finally, Spörer's law which corresponds to the variation of heliographic latitudes of the active regions formation during the solar cycle also affects the shape of the Fourier power spectrum around the rotational frequency. Indeed, because of the differential rotation, structures are rotating faster close to the Equator. Hence the detection of the modulation will be spread over a range of frequencies.

The rotational modulation arises from asymmetries in the longitudinal distribution of plages as explained in Vanden Broeck et al. (2024). Therefore, the frequency of the rotational modulation is set by the latitude at which such asymmetries appear, provided that their visibility changes with the rotation phase. For an inclination $i > 0°$ (respectively $i < 0°$), it is the regions between about 0° and $-90° + i$ (resp. 0° and $90° + i$) for which the visibility changes most during the rotational cycle. As a result, for inclinations far away from an Equator-on view, the most relevant frequency can be associated with active regions at latitudes in the other hemisphere as they undergo a substantial modulation of their visibility.

For inclinations between −20° and +20° (see Fig. C.1), the power spectra remain essentially identical. From $|i| \geq 30°$ on, the amplitudes of the rotational modulation decrease as the absolute value of the inclination increases as illustrated in Fig. 10 for a view with an inclination of 30°. We note a difference in behaviour between the Northern and the Southern inclinations: the group of peaks remain more important while moving towards the North Pole-on view ($i = +90°$). In the Southern hemisphere (negative inclinations) only one peak remains important. This behaviour suggests that asymmetries in the longitudinal distribution of plages were stronger and thus more detectable in the Southern hemisphere.

Finally, as observed in Fig. 11, for $|i| \geq 70°$, the rotational modulation is no longer remarkable in the power spectrum and would certainly be missed in noisy and less densely sampled time series of other stars. Moreover, we observe a difference between both hemispheres. While the power spectrum for the Southern hemisphere (inclination $i = -70°$) presents one clearly visible peak, the power spectrum for the Northern hemisphere (inclination $i = 70°$) displays several peaks with the same power. An explanation of this behavior is the asymmetry of the distribution of active regions between both hemispheres, as observed in Fig. 7. The distribution is not symmetric relative to the Equator, so that the visibility of the active regions will be affected depending on the viewing angle. Indeed, for an inclination $i = +70°$, magnetic structures in the Northern hemisphere down to a latitude of +20° will be visible over the entire rotation cycle, although with a changing aspect angle (sometimes closer to limb, sometimes closer to the centre of the disk). Therefore, these structures will not result in a strong rotational variation. Rotational modulation instead arises from active regions located at more Southern latitudes. In our example, it is the negative latitudes, down to −20°, that will have the strongest impact. In our time series, the Southern hemisphere hosts more active regions than the Northern hemisphere during the solar maximum (see Fig. 7). Together with the finite lifetime of these active re-

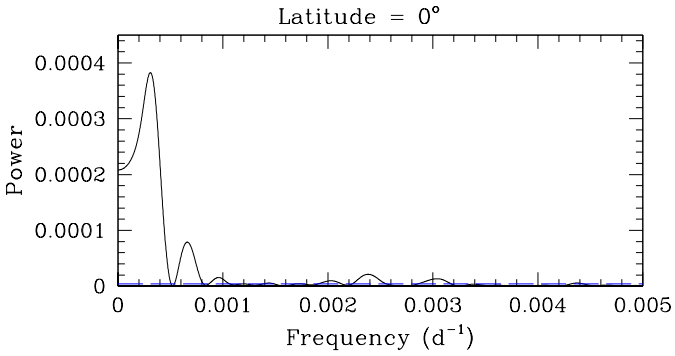

Fig. 12: Fourier power spectrum zoomed at very low frequencies in the case of a view with an inclination $i = 0°$ (Equator-on view). The panel illustrates the power spectrum over the frequency range below 0.005 d^{-1}. The long-dashed blue horizontal line yields the 99% significance level.

gions, the North/South asymmetry leads to the presence of multiple peaks in the power spectrum near the Carrington rotation frequency for $i = +70°$.

4.2. Effect on the detection of the solar cycle

To study the effect on the solar cycle timescale, we consider the power spectrum zoomed at very low frequencies. Fig. 12 illustrates this power spectrum for the view from the Equator ($i = 0°$). We can clearly see the peak of detection of the solar cycle modulation located at the frequency of ± 0.00025 d^{-1} corresponding to a period of ∼ 10.95 years, analogous to the typical 11-years solar cycle.

Fig. 13 illustrates the Fourier power spectrum over the same frequency range for the Pole-on views ($i = -90°$ and $i = 90°$) and Fig. D.1 in appendix D for all inclinations by steps of 10°. The reduction of the power when the absolute value of the inclination increases is somewhat stronger for positive inclinations, but in both cases (positive or negative inclinations) the long-term modulation remains visible up to $|i| = 90°$, although with a significantly reduced power compared to an Equator-on view.

4.3. Effect of the sampling

The USET Ca II K observations of the Sun benefit from a denser sampling than observations of other solar-like stars. Indeed, whilst the Sun can be observed during the whole year, the visibility of most stars is restricted to periods of typically six months. Moreover, whilst USET is dedicated to observations of the Sun, telescopes used for the study of chromospherically active stars usually have to share the observing time between a number of targets, resulting in a lower cadence of observations than for the USET data. This situation could bias the discussion of the detectability of the cyclic modulation as a function of inclination.

To account for this effect, we consider the sample of solar-like stars of Hempelmann et al. (2016) which are monitored with the TIGRE telescope to search for rotational modulations and activity cycles in their S-index. We extracted the actual sampling of the TIGRE observations of these stars over the time interval from 2013 until the end of 2023 from the TIGRE data archive. The number of observations ranges from less than 50 for the least-frequently observed star to over 400 for the most-

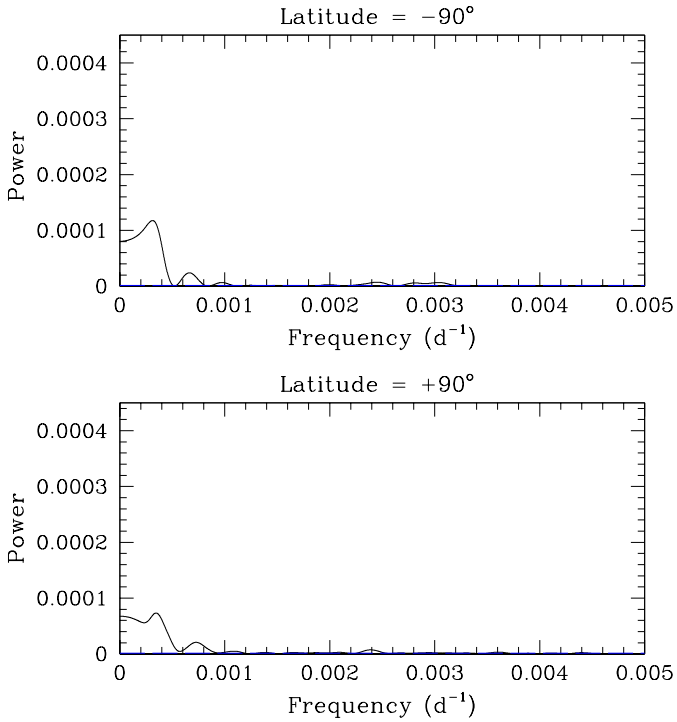

Fig. 13: Fourier power spectrum zoomed at very low frequencies for the Pole-on views with an inclination $i = -90°$ (top) and $i = 90°$ (bottom).. The panel illustrates the power spectrum over the frequency range below 0.005 d^{-1}. The long-dashed blue horizontal line yields the 99% significance level.

intensively observed targets. The mean and median number of observations for an individual star are both around 200 spread over this 10 years period. Fig. 14 illustrates the spectral windows computed for a subset of these time series. The spectral windows are dominated by the 1 d^{-1} alias. As one could expect, the spectral windows are cleaner when the number of data points increases. However, the most important difference compared to the time series of solar observations concerns the occurrence of a yearly alias at 0.00274 d^{-1} which can be seen by zooming on the spectral windows (bottom panel of Fig. 14). This latter feature stems from the above-discussed visibility constraints and can clearly be expected to impact the detectability of the long-term cycles. However, it should be emphasized that, due to its short duration, our time series is less favorable for the study of the long-duration cycle than some stellar time series. Indeed our dataset only covers a single cycle. Consequently, the width of the peak in the Fourier power spectrum leads to a significant uncertainty on the actual period of the activity cycle. For other stars, even with a relatively sparse sampling, typically more than one activity cycle has been observed, allowing therefore a more accurate determination of the frequency associated with the long cycle.

We have then sampled the time series of the USET plages and enhanced network areas for different inclinations according to the sampling of the TIGRE observations of solar-like stars. Hereafter, we focus our discussion on the sampling corresponding to a number of 206 observations spread over ten years. Figure 15 illustrates the Fourier power spectrum for an Equator-on inclination for frequencies below 0.05 d^{-1} as well as around $\nu_{\rm Car}$. Whilst the long-term cycle still provides the highest peak in the power spectrum, we note the presence of a strong yearly

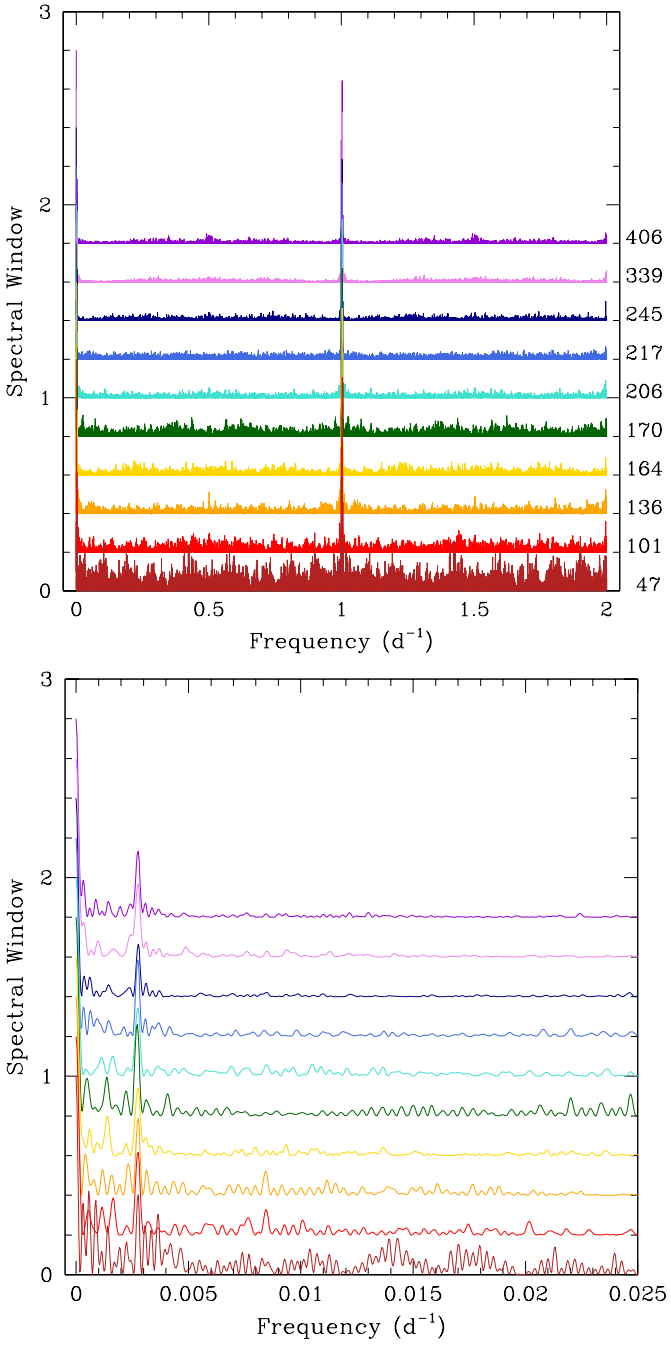

Fig. 14: Spectral window of actual time series of TIGRE observations of solar-like stars. The top panel illustrates the spectral window up to 2 d^{-1}, whilst the bottom panel yields a zoom on the low-frequency domain, illustrating the appearance of a yearly alias. The numbers on the right of the top panel indicate the number of observations collected over the interval between 2013 and 2023. The least frequently observed star was observed less than 50 times while the most-intensively observed one has over 400 observations.

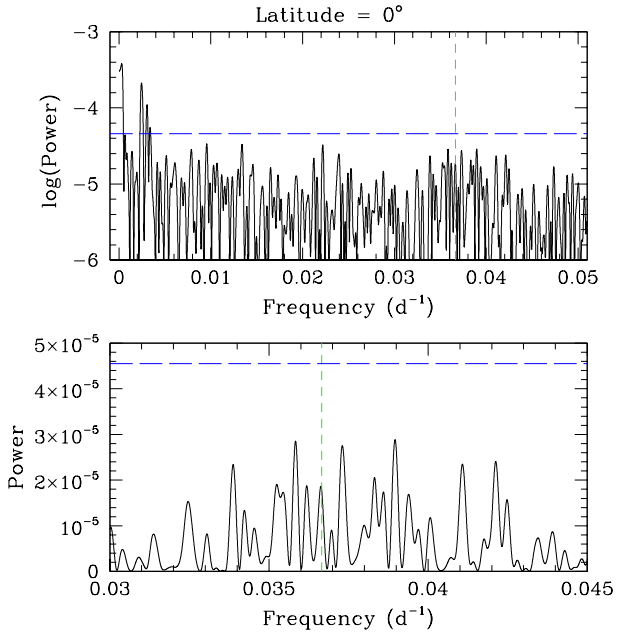

Fig. 15: Fourier power spectrum of the resampled USET time series assuming 206 observations spread over ten years for an Equator-on view. The top panel illustrates the logarithm of the power spectrum for frequencies below 0.05 d^{-1}. The bottom panel provides a zoom on the power around $\nu_{\rm Car}$ (given by the short-dashed green vertical line). The long-dashed blue horizontal line yields the 99% significance level.

alias. With the sampling assumed here, the strongest peak remains the one associated with the long-term cycle. The situation is much worse as far as the detection of the rotational frequency is concerned. The sampling no longer allows an unambiguous identification of the dominant frequency that was found in the actual USET data. Indeed, there are now at least three peaks of equal strength around $\nu_{\rm Car}$, although all of them have a power well below the 99% significance level. But what is even worse is that there are a number of peaks at very different frequencies (e.g., near 0.009, 0.013 or 0.022 d^{-1}) which have a power that is equal or higher than that of the peaks near the actual rotation frequency. In a real stellar time series, one would thus not be able to identify the right frequency among those peaks. The situation remains essentially the same for other inclination angles (Fig. E.1 in appendix E). We thus conclude that a sampling of about 200 observations spread over ten years would not allow a clear detection of the rotational modulation. This is not surprising given the fact that the visibility of the rotational modulation in the Sun's plages and enhanced network area varies significantly with time as shown in Vanden Broeck et al. (2024). A patchy sampling can thus easily miss those episodes where the rotational modulation would be well detected. For the long-term cycle, we observe that the peak associated with the true frequency remains the dominant one.

As a next step, we have resampled the USET plages and enhanced network area time series for inclinations of +30° and −30° according to the observing cadence of ten representative stars of the TIGRE sample of Hempelmann et al. (2016). We used those stars for which the spectral windows of their time series are displayed in Fig. 14. The results of this exercise are illustrated in Fig. 16 for the sampling used for three stars with 405, 206 and 47 observations over ten years.

Although the long-term cycle is detected in all cases, one can clearly see that the contrast of the peak with respect to the 99% significance level strongly decreases when the sampling gets sparser, as expected. The ratio between the power of the highest peak and the 99% significance level decreases from 14

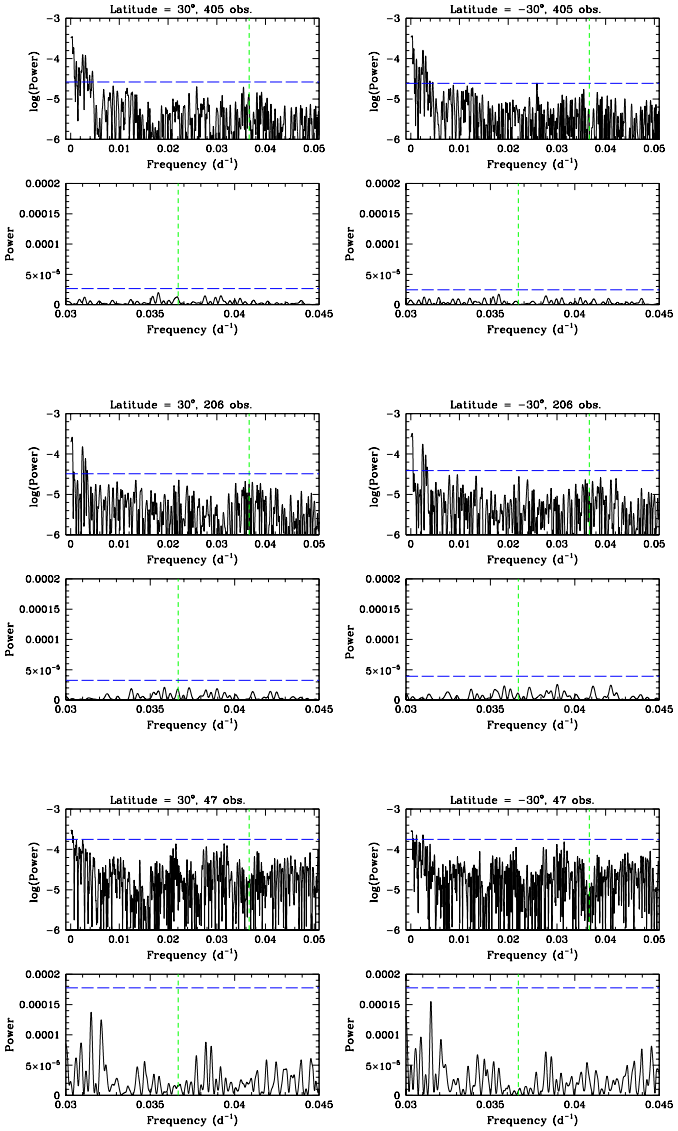

Fig. 16: Fourier power spectrum of the resampled USET time series for a decreasing observing cadence (from top to bottom) and for inclination angles of +30° (left column) and −30° (right column row). For each case, top panel illustrates the logarithm of the power spectrum for frequencies below 0.05 d^{-1} and the bottom panel provides a zoom on the power around ν_{Car} (given by the short-dashed green vertical line). The long-dashed blue horizontal line yields the 99% significance level.

for the densest sampling to 8 for the intermediate case and 1.6 for the sparsest case. Hence, we conclude that a long-term cycle with an amplitude identical to that of the Sun would remain detectable with a sampling of ∼ 20 observations per year, provided that the data cover a sufficiently long time interval. As expected, the significance level decreases when the number of observations decreases, becoming marginal for the sparsest sampling (a handful of observations per year). Conversely, as we already concluded hereabove, in all cases, the observing strategy fails to detect the rotational modulation.

Finally, to assess the impact of the amplitude of the cyclic variations on their detectability with a typical sampling of solar-like stars, we performed another set of simulations. We first adjusted the long-term cycle variations for each set of simulated

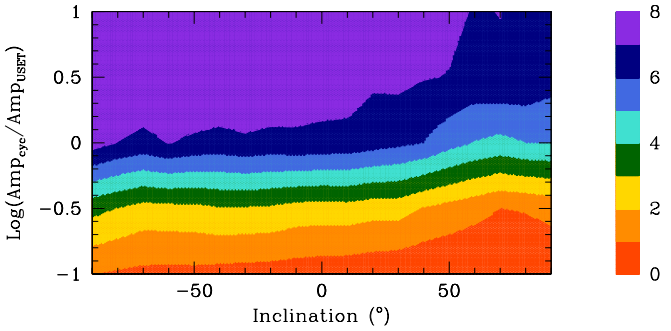

Fig. 17: Detectability of the long-term cycle as a function of the inclination and the scaled amplitude of the long-term cycle. The colour-scale to the right indicates the ratio between the power of the peak associated with the long-term cycle in the Fourier power spectrum and the 99% significance level.

out-of-ecliptic USET data (i.e., for each value of the inclination) by a polynomial of degree six as we had done for the actual USET observations in Vanden Broeck et al. (2024). Subtracting this polynomial from the simulated time series yields a proxy of the shorter term variations. We then scaled the amplitude of the adjusted long-term cycle by a factor between 0.1 and 10.0 (in logarithmic steps of $\log \mathrm{Amp_{cyc}}/\mathrm{Amp_{USET}} = -0.5$. These scaled long-term variations were then added back to the shorter term variations to simulate situations of solar-like stars with different ratios between the amplitudes of the short and long-term variations. These simulated time series were then resampled with our reference observing cadence assuming 206 observations spread over ten years. For each resampled synthetic time series, we performed a Fourier analysis and determined the 99% significance level via our re-shuffling method. Fig. 17 illustrates the results of this exercise. The colours indicate the ratio between the power of the strongest peak in the Fourier spectrum that is associated with the long-term cycle and the 99% significance level. As one could expect, the detectability of the long-term cycle becomes marginal (ratio below 1, red colour in Fig. 17) when the amplitude of the cycle is scaled down by a factor 0.1. We note that the visibility of the peak displays some variations with the inclination. At higher (positive) inclinations, the detectability is lower whatever the value of the scaling parameter. This results from the North-South asymmetry that we have found in the USET data. Overall, we find that with the sampling adopted here, the peak due to the long-term cycle is detected at a level at least 3 times above the 99% significance level provided that the amplitude of the cyclic variations remains at a level of at least 33% of the amplitude seen in the USET data. For lower values, the detections become uncertain also because the highest peaks in the Fourier spectra are no longer necessarily associated with the frequency of the long-term cycle.

5. Discussions and conclusions

Based on full-disk images of the solar chromosphere in the Ca II K line from the USET station, we have mapped the solar surface with synoptic maps. We have segmented the brightest structures and produced a time series of their area fraction. Then we have used an appropriate projection to represent the solar surface as it would be seen under various viewing angles. We have computed the area fraction for different inclinations and its variation goes up to 63% between the Equator-on view and the Poles-on view during the maximum of the solar cycle.

As the plages and enhanced network area fraction is a good proxy for the S-index (Vanden Broeck et al. 2024), this study can be used to make a connection between the Sun and the other Sun-like stars. In particular it could be used to better understand the detection of temporal modulation for the other stars that are not necessarily viewed from the Equator plane. To reach this goal, we have analysed the impact of the viewing angle on the area fraction time series by using Fourier power spectrum.

Our results show an important impact of the viewing angle on the detection of modulation due to the solar rotation. If the observations use the same (dense) sampling as the USET data, the rotation is detectable up to an inclination of $|i| = 70°$. For higher values the rotation is not visible anymore in the signal and would be missed. This behaviour could be explained by the fact that from a Pole-on view, an asymmetry in the plages distribution will be either permanently visible or not visible at all during a full solar rotation cycle.

On the long term, the chromospheric activity cycles of Sun-like stars should remain detectable even for stars seen under a near Pole-on viewing angle. Positive and negative inclinations give different results due to the asymmetry of the solar activity in the Northern and Southern hemispheres, as already seen for other magnetic structures.

For other stars, the actual detectability will also depend on the sampling of the time series and on the quality of the data. Indeed, our USET time series benefits from a long continuous time series with a dense sampling. Actual time series of stellar S-indices have usually more complicated and scarcer samplings including months-long gaps due to restricted target visibility. We have analysed the effect of the sampling on the detection of the periodic modulations by extracting the actual sampling of TIGRE observations of Sun-like stars over a period of ten years. The least frequently observed star was observed less than 50 times while the most-intensively observed one has over 400 observations. We demonstrated that a more realistic sampling leads to the vanishing of the rotational modulation detection. However, the modulation due to the activity cycle remains visible at nearly all inclinations if the sampling contains at least 20 observations per year and as long as the amplitude of the cyclic variation is at least 30% of the solar cycle amplitude. This conclusion is made on the assumption of a typical solar activity case (i.e. of $\sim$ 11 years). In the case of stars with a much shorter or much longer cycle than the solar cycle, the period of the activity cycle will be very difficult to determine because of the sparsity of the sampling. Indeed, for significantly longer cycles, we would need a much longer homogeneous dataset, which is hard to collect for stellar observations. For shorter cycles (of a few months, e.g., Mittag et al. 2019), the sparse sampling assumed here would clearly fail to correctly identify the exact cycle duration. An extension of our present study would benefit from a dataset covering a longer time-span, as the impact of the inclination axis might vary with the solar cycle amplitude (Sowmya et al. 2021).

Acknowledgements. The authors wish to thank Sowmya Krishnamurthy from the Max Planck Institute for Solar Research System, in Germany, for the very productive discussions that enabled them to carry out the work on the orthographic projection. Grégory Vanden Broeck was supported by a PhD grant awarded by the Royal Observatory of Belgium. The USET instruments are built and operated with the financial support of the Solar-Terrestrial Center of Excellence (STCE).

References

Baliunas, S. L., Donahue, R. A., Soon, W., & Henry, G. W. 1998, in Astronomical Society of the Pacific Conference Series, Vol. 154, Cool Stars, Stellar Systems, and the Sun, ed. R. A. Donahue & J. A. Bookbinder, 153
Baliunas, S. L., Horne, J. H., Porter, A., et al. 1985, ApJ, 294, 310
Bechet, S. & Clette, F. 2002, USET images L1centered, https://doi.org/10.24414/nc7j-b391, published by Royal Observatory of Belgium (ROB)
Borgniet, S., Meunier, N., & Lagrange, A. M. 2015, A&A, 581, A133
Boro Saikia, S., Marvin, C. J., Jeffers, S. V., et al. 2018, A&A, 616, A108
Calabretta, M. R. & Greisen, E. W. 2002, A&A, 395, 1077
Devi, P., Singh, J., Chandra, R., Priyal, M., & Joshi, R. 2021, Sol. Phys., 296, 49
El-Borie, M., El-Taher, A., Thabet, A., Ibrahim, S., & Bishara, A. 2021, Chinese Journal of Physics, 72, 1
Gosset, E., Royer, P., Rauw, G., Manfroid, J., & Vreux, J. M. 2001, MNRAS, 327, 435
Heck, A., Manfroid, J., & Mersch, G. 1985, A&AS, 59, 63
Hempelmann, A., Mittag, M., Gonzalez-Perez, J. N., et al. 2016, A&A, 586, A14
Knaack, R., Fligge, M., Solanki, S. K., & Unruh, Y. C. 2001, A&A, 376, 1080
Lockwood, G. W. & Skiff, B. A. 1990, in NASA Conference Publication, Vol. 3086, NASA Conference Publication, 8–15
Lockwood, G. W., Skiff, B. A., Henry, G. W., et al. 2007, ApJS, 171, 260
Met Office. 2010 - 2015, Cartopy: a cartographic python library with a Matplotlib interface, Exeter, Devon
Meunier, N., Lagrange, A. M., Boulet, T., & Borgniet, S. 2019, A&A, 627, A56
Meunier, N., Lagrange, A. M., Dumusque, X., & Sulis, S. 2024, A&A, 687, A303
Mittag, M., Schmitt, J. H. M. M., Hempelmann, A., & Schröder, K. P. 2019, A&A, 621, A136
Mittag, M., Schmitt, J. H. M. M., & Schröder, K. P. 2023, A&A, 674, A116
Mittag, M., Schröder, K. P., Hempelmann, A., González-Pérez, J. N., & Schmitt, J. H. M. M. 2016, A&A, 591, A89
Nèmec, N. E., Shapiro, A. I., Krivova, N. A., et al. 2020, A&A, 636, A43
Noyes, R. W., Hartmann, L. W., Baliunas, S. L., Duncan, D. K., & Vaughan, A. H. 1984, ApJ, 279, 763
Radick, R. R., Lockwood, G. W., Henry, G. W., Hall, J. C., & Pevtsov, A. A. 2018, ApJ, 855, 75
Reinhold, T., Shapiro, A. I., Solanki, S. K., et al. 2020, Science, 368, 518
Schatten, K. H. 1993, J. Geophys. Res., 98, 18907
Shapiro, A. I., Solanki, S. K., Krivova, N. A., et al. 2014, A&A, 569, A38
Singh, J., Priyal, M., Ravindra, B., Bertello, L., & Pevtsov, A. 2023, Research in Astronomy and Astrophysics, 23, 045016
Sowmya, K., Shapiro, A. I., Witzke, V., et al. 2021, ApJ, 914, 21
Vanden Broeck, G., Bechet, S., Clette, F., et al. 2024, A&A
Vaughan, A. H., Baliunas, S. L., Middelkoop, F., et al. 1981, ApJ, 250, 276
Veronig, A. M., Jain, S., Podladchikova, T., Pötzi, W., & Clette, F. 2021, A&A, 652, A56
Wilson, O. C. 1978, ApJ, 226, 379
Wright, J. T., Marcy, G. W., Butler, R. P., & Vogt, S. S. 2004, ApJS, 152, 261

Appendix A: Generation of solar-disk views for different inclinations.

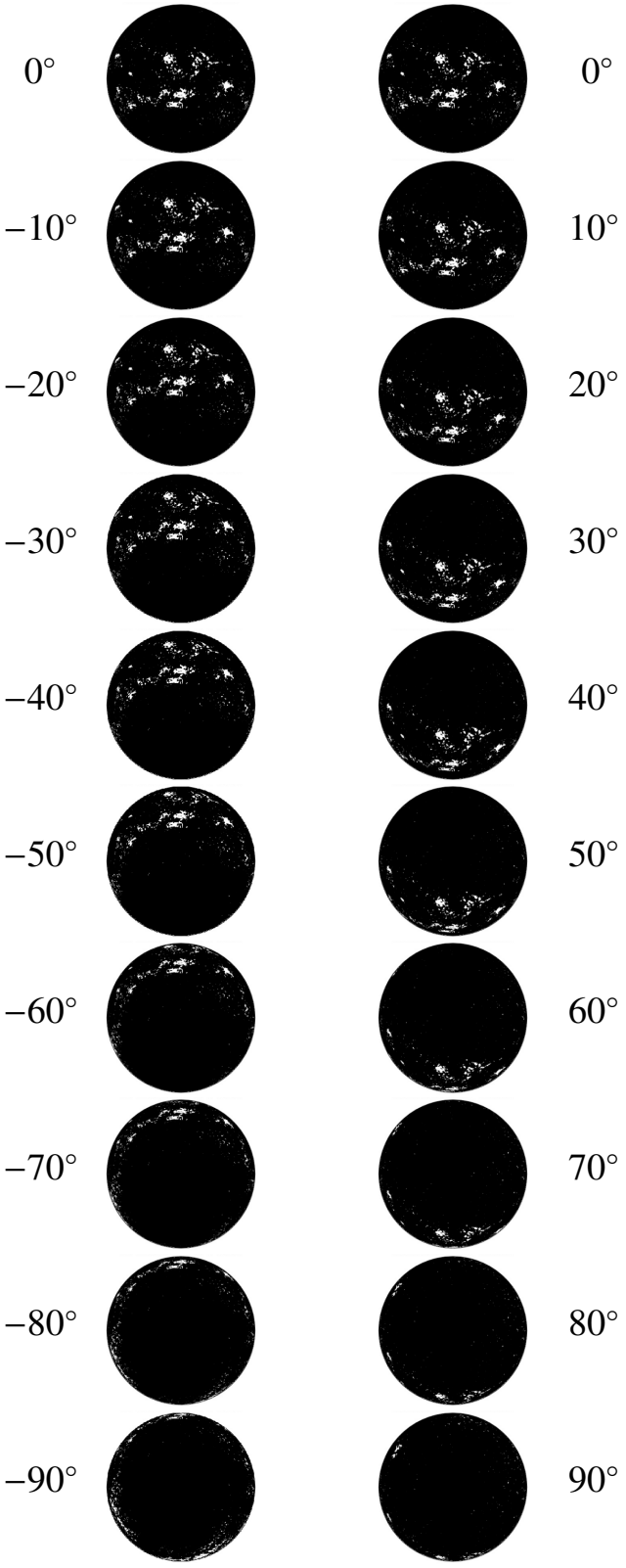

Fig. A.1: Distribution of the segmented structures with the generated solar-disk views on 1st of August 2014 for inclinations from 0° of latitude to 90° and −90° of latitude by steps of 10°. Inclination angles are specified next to each image and represent the number of degree relative to the Equator-on view (i = 0°). Top images illustrate the view from the Equator and it goes to the South Pole view (left) and to the North Pole view (right).

Appendix B: Fourier power spectra for different inclinations

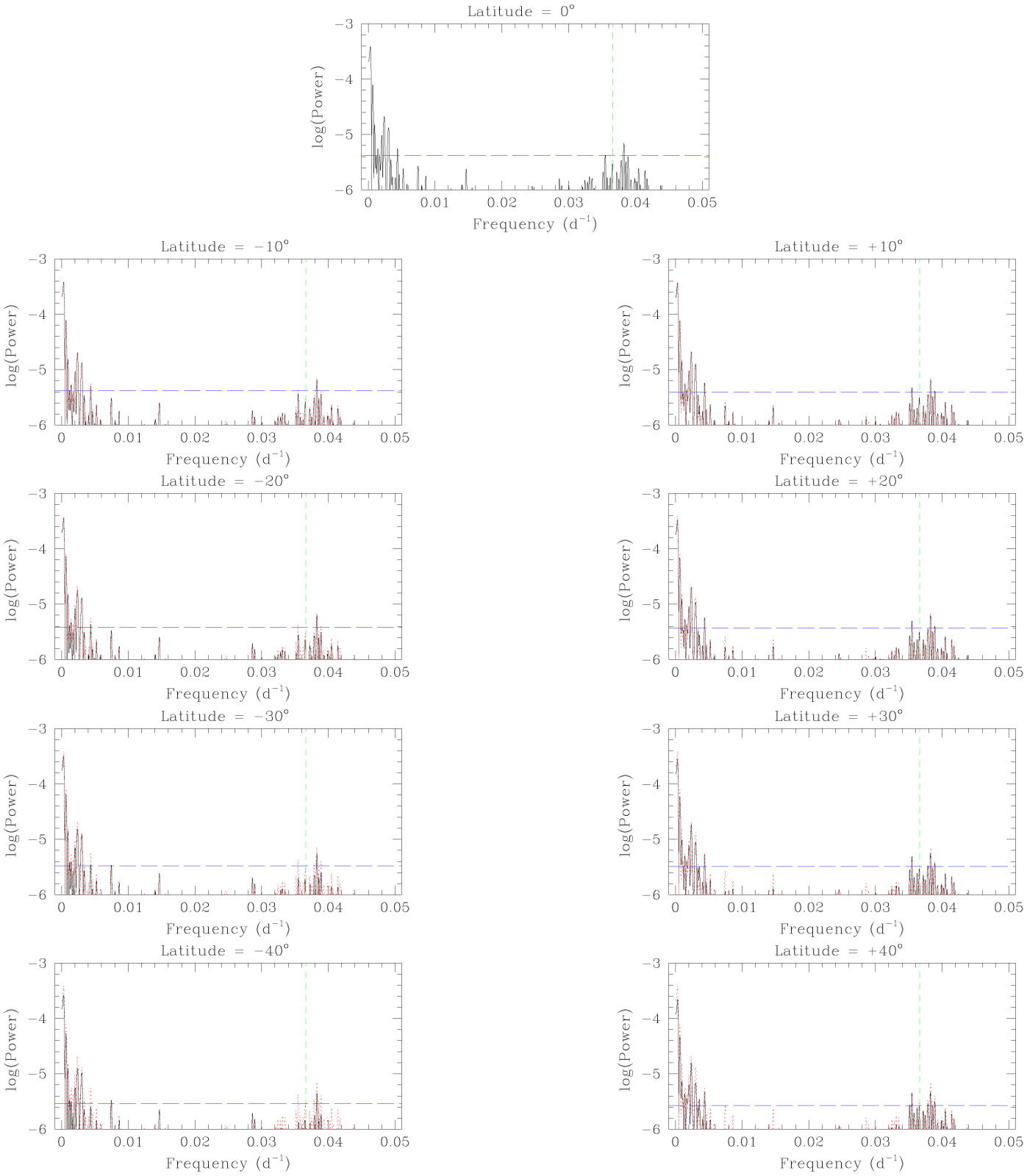

Fig. B.1: Fourier power spectra for different inclination angles and for frequencies below 0.05 d^{-1}. Inclination angles are specified at the top of the plots and represent the number of degrees relative to the Equator-on (i = 0°). Left panels: inclinations to the South Pole view ; Right panels: inclinations to the North Pole view. In each panel, the actual power spectrum for that inclination is shown in black, whereas the red dotted curve replicates the power spectrum for i = 0°. The green dashed line yields $\nu_{\rm Car}$ while the long-dashed blue horizontal line yields the 99% significance level.

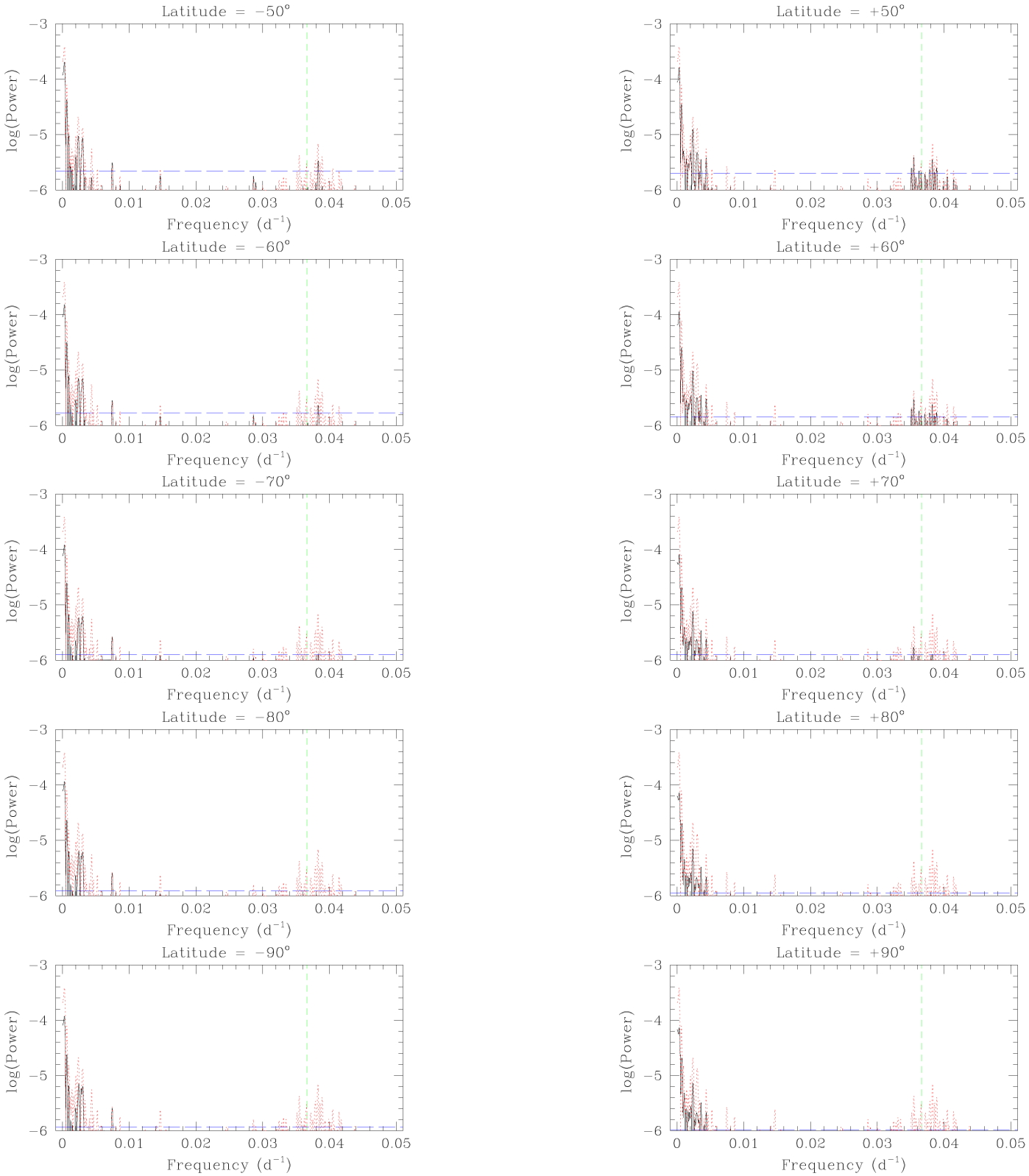

Fig. B.1: Continued

Appendix C: Fourier power spectra for different inclinations (near the solar rotation frequency)

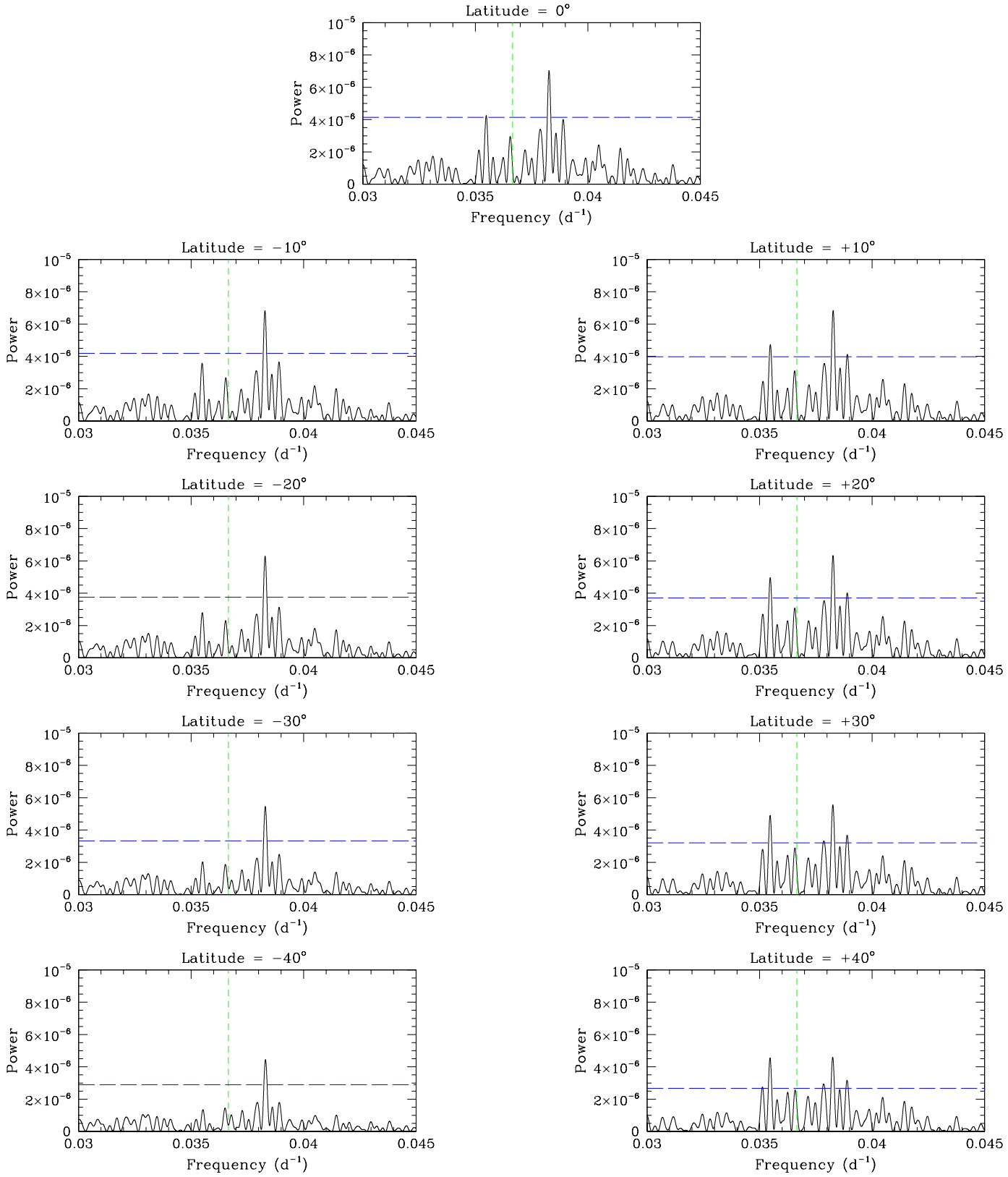

Fig. C.1: Evolution of the Fourier power spectrum near the rotation frequency of the Sun with inclinations specified at the top of the plot representing the number of degrees relative to the Equator-on ($i = 0°$). Left panels: inclinations to the South Pole view ; Right panels: inclinations to the North Pole view. The green dashed line yields $\nu_{\rm Car}$, while the long-dashed blue horizontal line yields the 99% significance level.

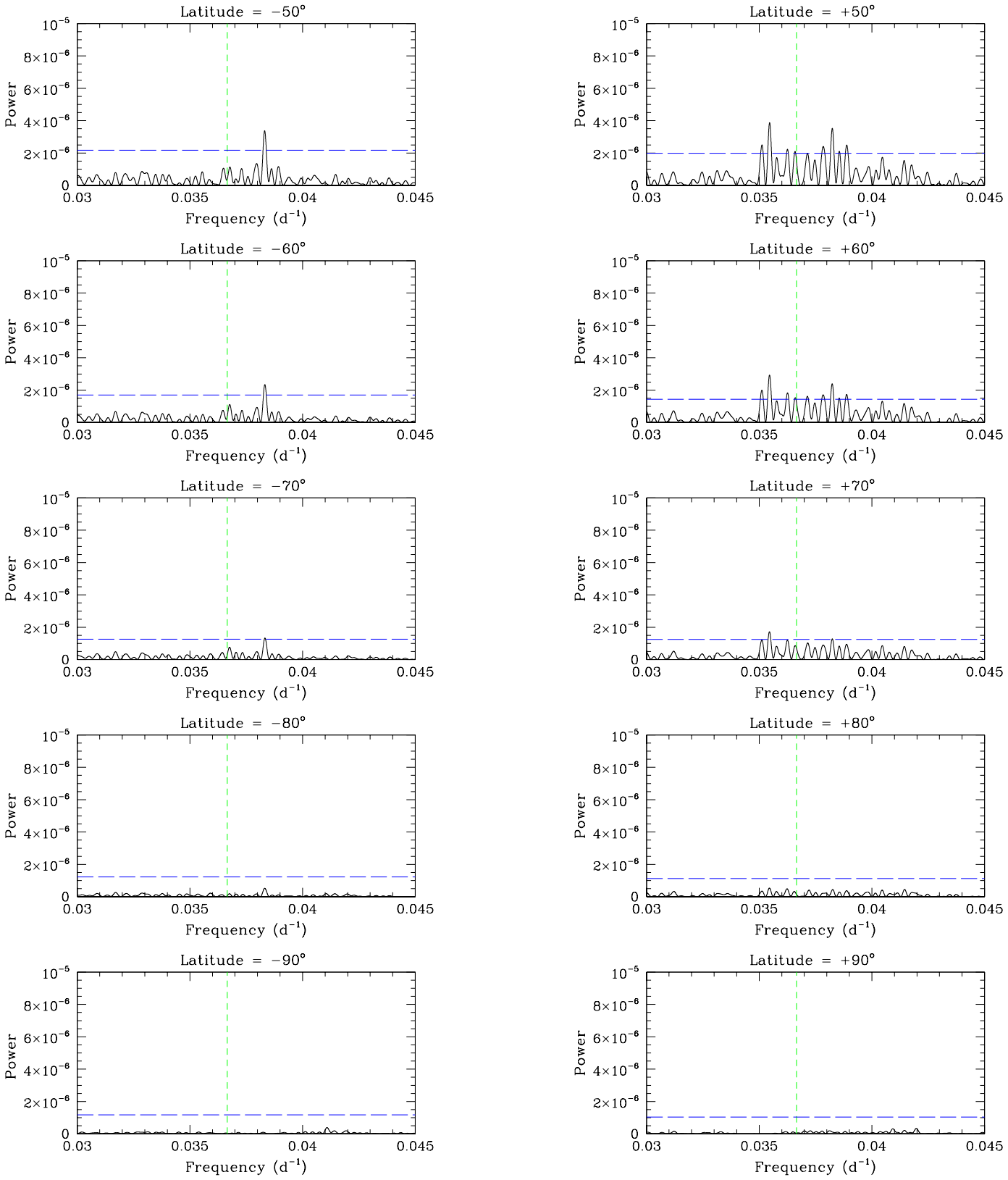

Fig. C.1: Continued

Appendix D: Fourier power spectra for different inclinations (near the solar activity cycle frequency)

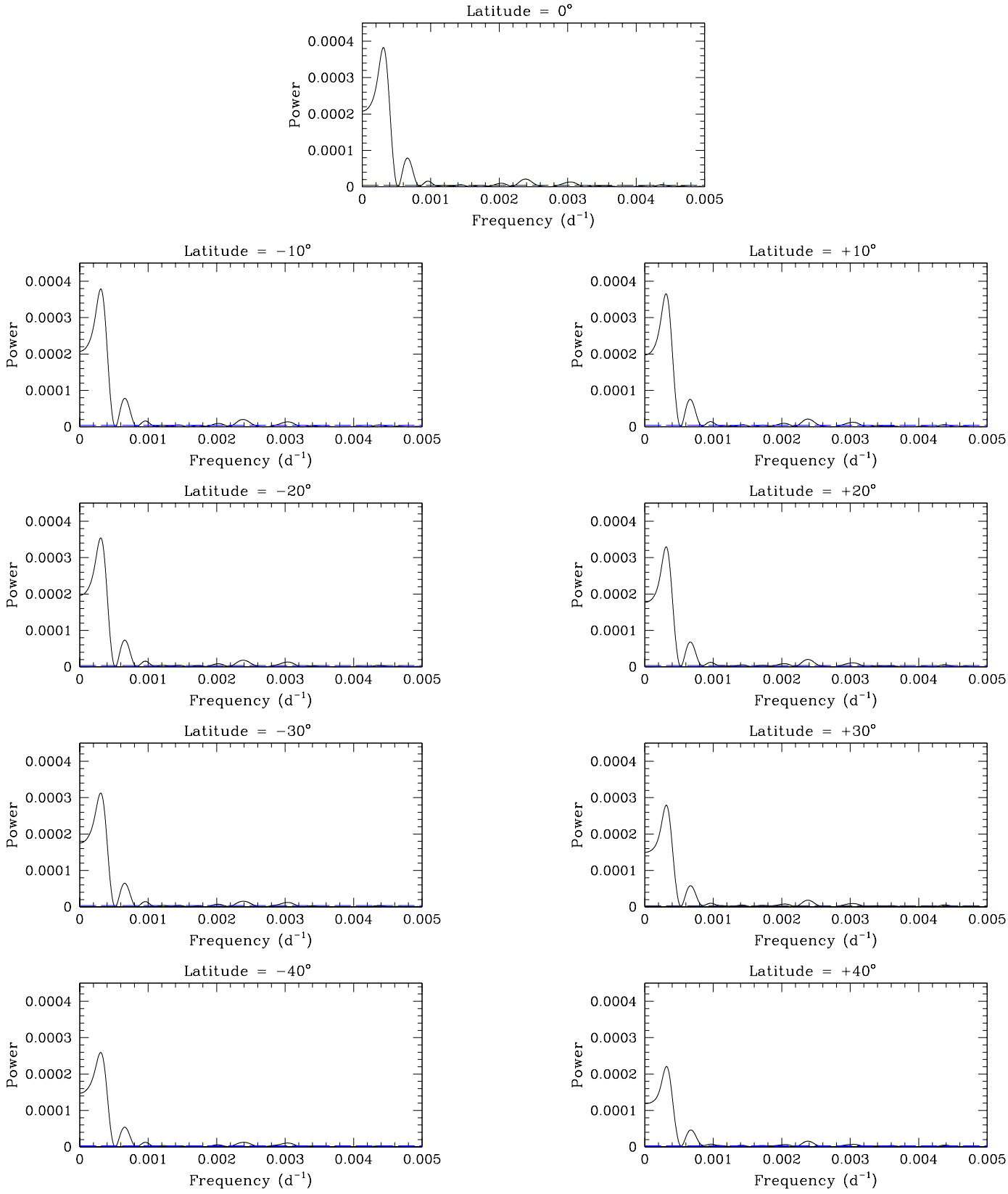

Fig. D.1: Evolution of the Fourier power spectrum near the frequency of solar activity cycle with inclinations specified at the top of the plot representing the number of degrees relative to the Equator-on ($i = 0°$). Left panels: inclinations to the South Pole view ; Right panels: inclinations to the North Pole view.

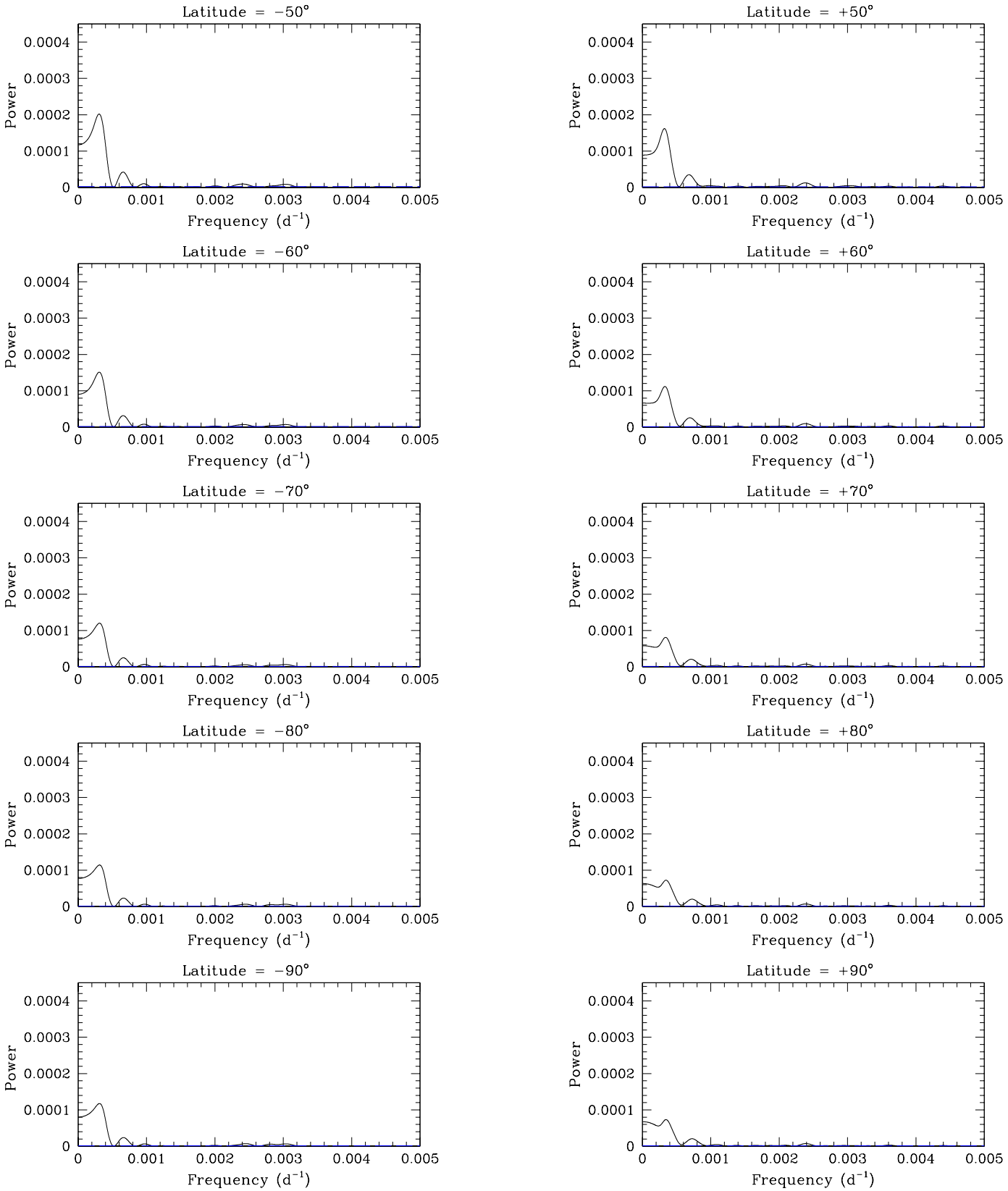

Fig. D.1: Continued

Appendix E: Fourier power spectrum of the resampled USET time series assuming 206 observations spread over ten years for different viewing angles

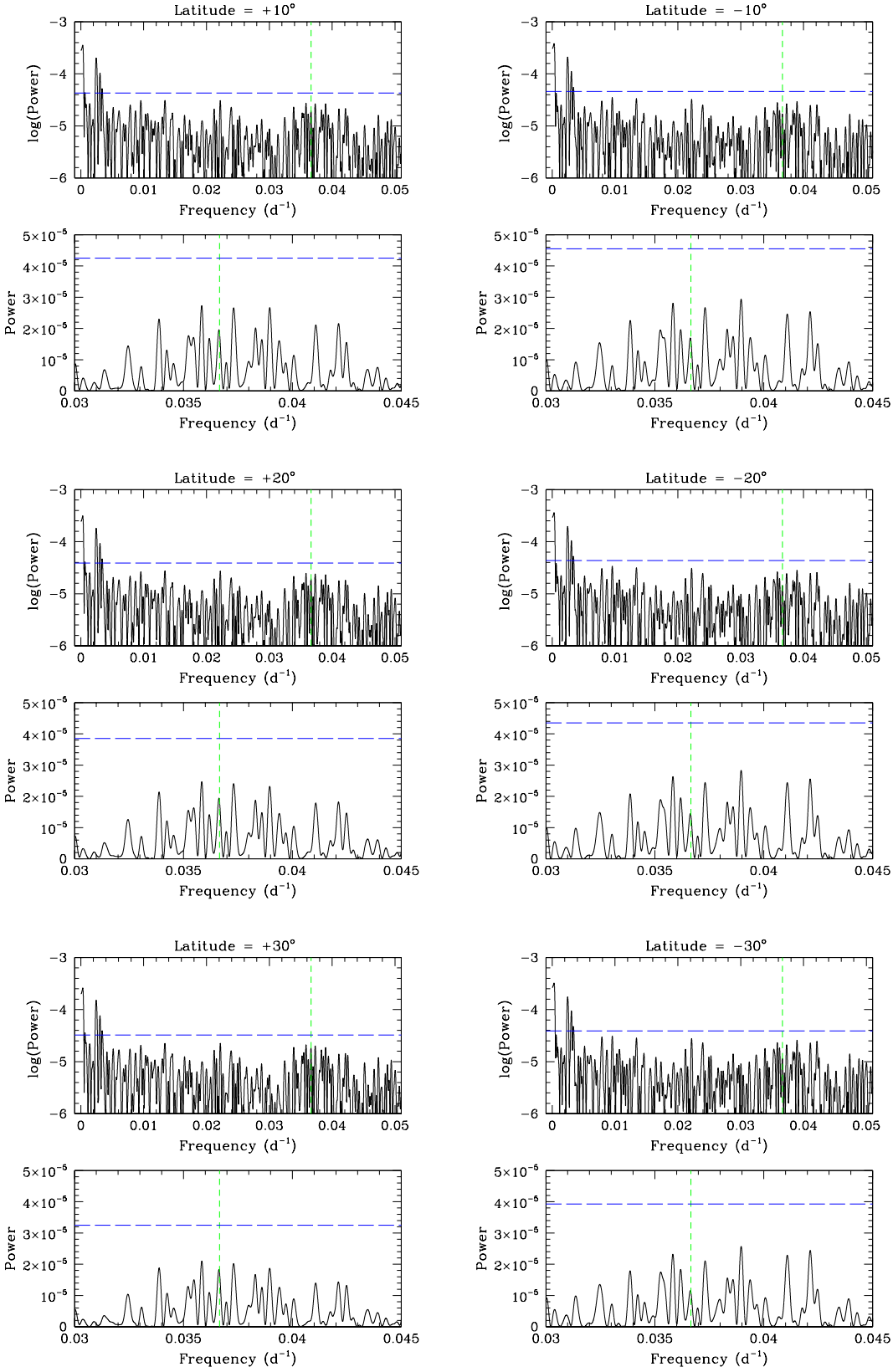

Fig. E.1: The top panels illustrate the logarithm of the power spectrum for frequencies below 0.05 d^{-1}. The bottom panels provide a zoom on the power around $\nu_{\rm Car}$ (given by the short-dashed green vertical line. The long-dashed blue horizontal line yields the 99% significance level.

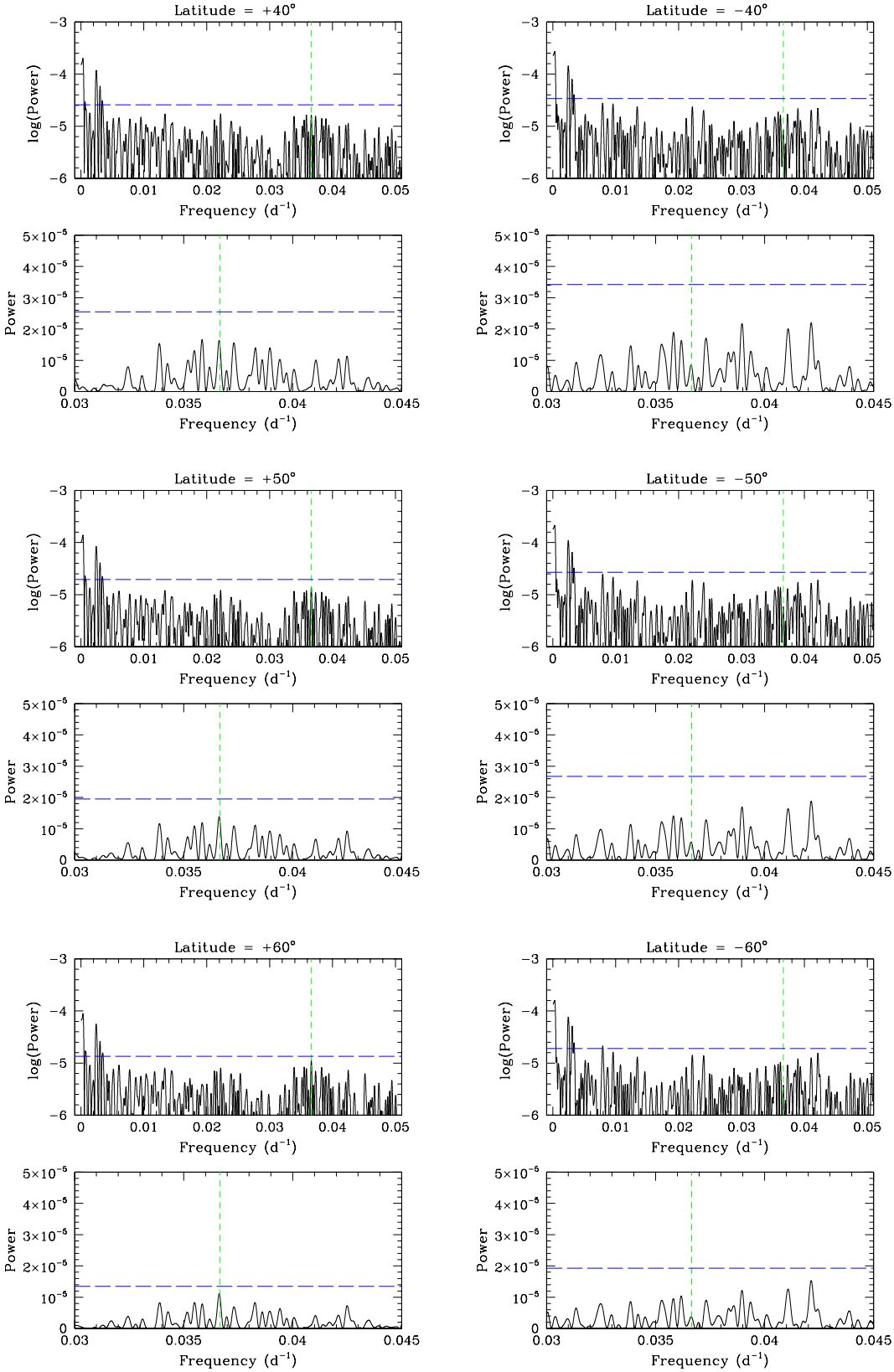

Fig. E.1: Continued.

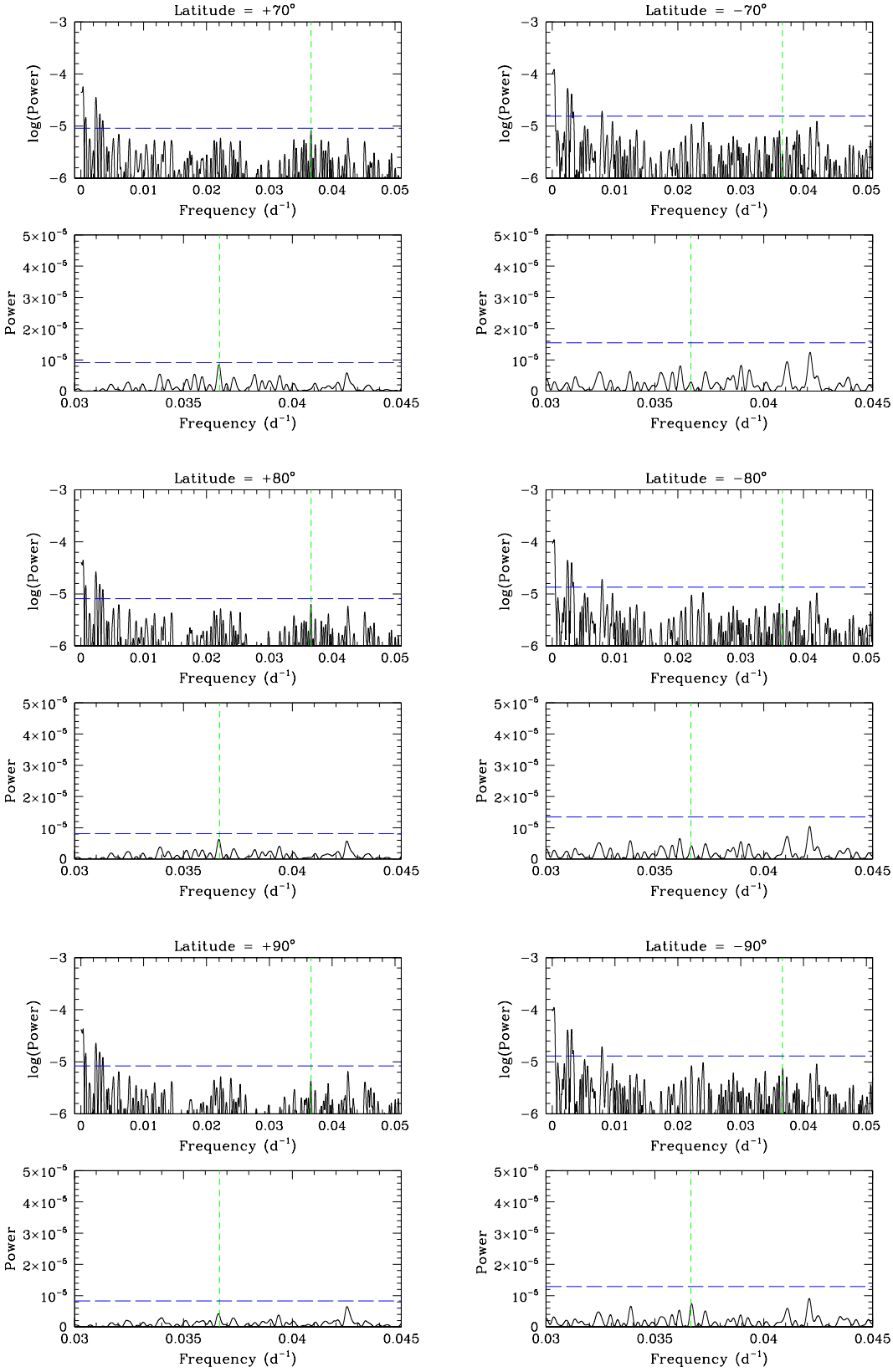

Fig. E.1: Continued.

5.1 Complementary information

5.1.1 North-South asymmetry

Based on direct solar observations from the USET station, we have simulated the distribution of plages and enhanced network as seen under various inclinations from a South Pole-on view to a North Pole-on view. We have then created area fraction time series for every inclination simulated and as expected, a significant variation was observed between an equatorial view and a polar view. Figure 6 in the above paper displays an obvious lower peak-to-peak amplitude in the variation of the area fraction when we move away from the Equator-on point of view, in both hemispheres. To quantify this observation, we have calculated the difference of area fraction, ΔA, between the maximum value $A_{\max}$ and the minimum value $A_{\min}$. Figure 5.3 illustrates the effect of the inclination on this cycle amplitude. The area fraction difference calculated with a polar view is almost reduced by a factor 3, compared to the Equator-on perspective. However, despite this large change in amplitude, the modulation associated with the solar cycle remains visible for both Pole-on views. Larger differences are naturally found close to an Equator-on view, as the active regions are distributed near the Equator in both hemispheres, but the largest one lies in the South hemisphere, under an inclination $i = 10°$. Another interesting observation from this figure is the discrepancy between the South Pole inclinations (negative values) and the North Pole inclinations (positive values). Indeed, as we move away from the equatorial view, ΔA decreases more rapidly with North Pole inclinations. Those interpretations illustrate the North-South asymmetry of active regions distribution, as seen in Figure 7 of the paper above.

5.1.2 Long-duration dataset

Our results showed that the detection of the solar cycle period is possible for every inclination from the South Pole-on view to the North Pole-on view, with obviously the highest signal power for an equatorial point of view. We can see in the figures of appendix D of the article above that the peak is located at a frequency corresponding approximately to the activity cycle period of $\sim$ 11 years. However, the width of the peak is quite large leading to a rather large uncertainty on the frequency associated with the solar cycle. This is mainly due to the limited duration of the USET Ca II K dataset covering only one solar cycle. Conducting the same study with a dataset over a longer duration, covering multiple solar cycles, would reduce the width of the peak and thus increase the precision in detecting the period of the activity cycle.

5.2 Perspectives

- All the conclusions in this study are made on the assumption of a typical solar activity case, i.e. a cycle duration of $\sim$ 11 years. As said previously, using a longer dataset will allow to determine more precisely the long-term cycle period. For observations of solar-like

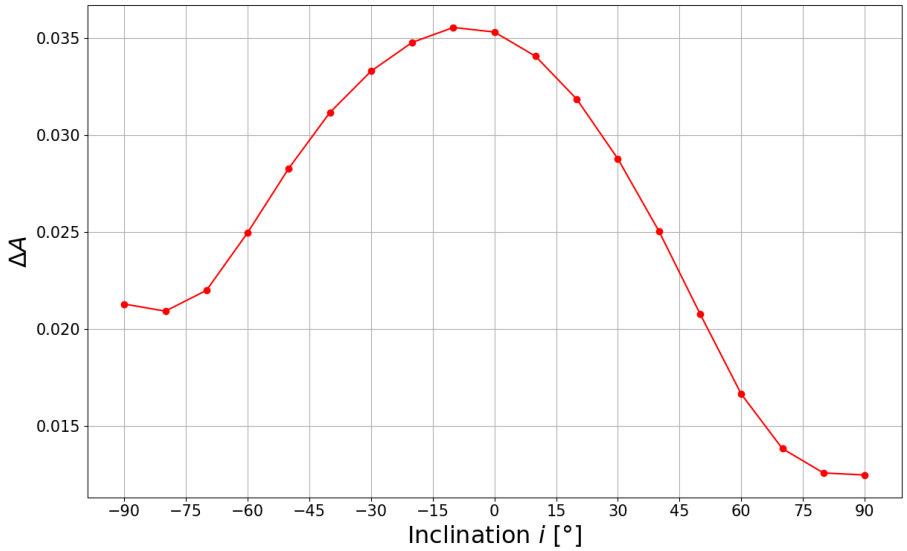

Fig. 5.3. Effect of the inclination on the cycle amplitude, for the period between end of 2012 and end of 2023. The cycle amplitude is denoted as ΔA which is defined as the difference between $A_{\max}$, the maximum area fraction (at the solar maximum), and $A_{\min}$, the minimum area fraction (at the solar minimum).

stars, the sparsity of the sample could still hinder the determination of the activity cycle duration, especially for very long cycles which require observations over many years that are usually difficult to gather. For the Sun, having a longer dataset would be beneficial for another aspect. We based our work on USET dataset which is covering the period between the ascending phase of the cycle 24 and the ascending phase of the cycle 25. Hence our results are derived from the amplitude of the cycle 24, the most recently completed solar cycle, which seems to be one of the weaker cycles. It is well-known that the amplitude is not identical for every cycle, as seen in Figure 1.7. As the impact of the inclination axis might vary with the solar cycle amplitude (Sowmya et al. 2021b), an extension of this work can be proposed to analyse the modulation of the activity cycle period by considering longer dataset.

- In cool stars with a convective envelope, stellar rotation and differential rotation are crucial processes for generating magnetic fields, which are responsible for many observable activity phenomena (Rüdiger 1989; Rüdiger & Hollerbach 2004). The rotation period of a star is closely linked to its age, offering a valuable tool for estimating stellar ages (Meibom et al. 2015). However, measuring stellar rotation presents challenges. Photometric methods, measuring the stellar flux variations caused by the presence of starspots, is a common approach to determine the rotation period of a star. Using this method, McQuillan et al. (2014) measured and published rotation periods of more than 30 000 main-sequence stars. The rotation period was also successfully determined using the S-index, chromospheric emission in the

Ca II K and H lines (Stimets & Giles 1980; Vaughan et al. 1981; Baliunas et al. 1985; Wright et al. 2004; Hempelmann et al. 2016), mainly caused by the chromospheric plages. However, the difficulty to measure the rotation period is increasing for less active stars. Stellar activity decreases with age, and stars rotate more slowly. Therefore, to detect a modulation, we need more observations. Our study has shown that the observations sampling has a significant effect on the detection of the periodic modulations, mainly the detection of the rotation period. Stellar observations are usually very limited in number, typically around 20 observations per year, which makes the detection of the rotation difficult or even impossible. This work underscores the importance of sampling in stellar monitoring programs. The way stars are observed depends primarily on their characteristics and on what aspects of the stars are being studied. In the case of determining the rotation period, for example, short observation sampling is sufficient for a young, fast-rotating star. However, for an older star with a slower rotation, several months of observations are likely required. In that sense, a possible improvement in stellar observation programs could be proposed as one of the contributions of this work.

Chapter 6

Conclusions and perspectives

6.1 Thesis summary

Even though the Sun is the closest star to our planet, it remains a sphere full of mysteries. The last decades have allowed scientists to increase our knowledge about many phenomena related to its magnetic activity. However, there is still a long way to go to uncover all the secrets of the interior, as well as those of the atmosphere of our precious star. Nevertheless, every small step, no matter how tiny, contributes to improve our understanding. This work aimed to provide new insights into the observations of magnetic activity of the Sun and other stars, particularly those that share similar characteristics with the Sun.

In Chapter 1, we gave a brief overview of the basic information about the Sun, its interior, its atmosphere, its magnetic activity, and its place among other stars. All the information provided in this Chapter is essential for a comprehensive understanding of the concepts and findings that were explored in our work.

Chapter 2 described the type of solar observations we used in our study. We mainly exploited the archives of solar images in the Ca II K line from the USET station, located in Brussels, Belgium. Those observations give valuable information about the solar chromosphere, and its magnetic structures, like the bright extended plages, the chromospheric network, or the sunspots. In order to create a link with the stellar activity, we took advantage of spectral measurements collected with the TIGRE telescope, located in Guanajuato, Mexico, which quantify the chromospheric emission in the core of the Ca II K and H lines. This index, called S-index, is widely used in astrophysics to monitor the chromospheric activity of stars. In addition to other stars, TIGRE also observes the Sun through the light reflected by the Moon.

The entire data processing was explained in Chapter 3. Starting from the raw USET images, we explained every step performed to extract the meaningful information: the fraction of the solar disk covered by the brightest chromospheric structures. We first performed a calibration of the data to use the highest quality images, by removing images affected by poor weather conditions (clouds, light diffusion, atmospheric turbulence) or from unintentional manipulations (cropped

images). Then the center-to-limb variation observed on the solar images was corrected to obtain an intensity-homogenized image. The correction of this optical effect was crucial for the segmentation of the structures. This segmentation was achieved by applying an intensity threshold based on a computation to determine the background intensity. Then we extracted the fraction of those structures over the solar disk obtaining a quantitative estimate of the chromospheric activity of the Sun. A time series of area fraction was created and was subsequently used for the analysis of our work. Another part of our study was to analyse the dependence of the observed chromospheric activity on the inclination of the rotation axis. For this, based on our Ca II K solar images, we built segmented synoptic maps to plot the entire solar surface during a complete solar rotation. Those segmented maps were used to generate solar masks viewed under any inclination from the South Pole-on view to the North Pole-on view. We finally derived time series of area fraction for various inclinations and this allowed us to highlight the importance of the inclination of the rotation axis of a star.

Chapters 4 and 5 outlined the analysis and the interpretation of the results obtained from the processed data. We presented our two papers with some complementary information in both chapters. The first article, in Chapter 4, dealt with the relationship between USET images and TIGRE observations. We compared a disk-resolved index, with area fraction of chromospheric structures, to an integrated spectrum index, with flux measurements. A linear relationship was found between both indices with a better correlation at low values when we take into account the plages and the enhanced network in the segmentation process of the solar Ca II K images. Moreover we studied the periodic modulations in both datasets to detect the solar rotation and the solar cycle periods. A Fourier power spectrum method was applied to the time series and for USET data, the rotational modulation was most prominently seen near the maximum and the rising part of the cycle and was essentially absent during the solar minimum. For TIGRE data, due to its observing strategy, the detection was intrinsically limited. However, the solar cycle was well detected, even though the analysed datasets span a bit less than the 11-year cycle. Our second paper, in Chapter 5, described the effect of the inclination of the rotation axis on the chromospheric activity. As the magnetic structures are not distributed uniformly in latitudes, observing the Sun from a different point of view affects the analysis of the magnetic features. With the reproduction of solar masks viewed under various inclinations, we could evaluate the impact of the inclination on the area fraction of the chromospheric active regions. We also used the Fourier power spectrum to investigate whether stars observed under a different viewing angle would also show the periodic modulations. While the solar cycle is detectable even under a near Pole-on view, the modulation due to the solar rotation remains visible up to an inclination of $|i| = 70°$, if the observations use the same (dense) sampling as the USET data. However, once we account for a more realistic sampling (including periods of low or zero visibility, as well as gaps due to poor weather and technical issues), the rotational modulation is no longer detected above the 99% significance level. The cyclic modulation remains visible at nearly all inclinations as long as the cyclic variation has

an amplitude compared to the faster variations that is at least 30% of the solar cycle amplitude and provided that at least about 200 observations are collected over a 10-year duration.

6.2 Thesis outlook

This research project has explored the magnetic activity of the Sun in the chromosphere and its connection with other Sun-like stars, contributing to a deeper understanding of the mechanisms driving the magnetic activity of the stars.

In the previous section, we have summarized the main conclusions of our work. However, our findings open the door to many other studies. Several aspects remain unexplored or can be improved.

First of all, thanks to the segmentation method, an important achievement of this work is the creation of a catalog of plages, detailing their number, their position, their area, and other relevant parameters. Our segmentation algorithm is installed on the ROB server and will be used for further research. Another PhD student already used our algorithm for his work to reconstruct synthetic images of the chromosphere based on images of the photosphere, using machine learning techniques.

A limitation of our USET Ca II K dataset is that it only contains data since July 2012, which is just slightly more than the duration of one solar cycle. Knowing that the amplitude of solar cycles is not constant, using data from other observatories spanning several decades would provide further insights into the variability based on the cycle's amplitude.

The results presented about the comparison between the disk-resolved index (with USET) and the S-index (with TIGRE) showed that the relationship between the two indices is linear. However, a dispersion is observed on the graph that is larger than the uncertainties. One hypothesis is the contribution of other slightly bright structures: the AN (active network) and QN (quiet network). An improved method of segmentation can be achieved by first removing the non-radial inhomogeneities and then adding those faint bright structures into the segmentation. This approach could enhance our understanding of the contribution of each chromospheric structure.

Magnetic structures appear visually different from one layer of the solar atmosphere to another, but they are somehow connected. An example is the photospheric faculae and the chromospheric plages. Both are bright extended regions associated with the concentrations of strong magnetic fields. However, faculae do not correspond exactly to plages because there is an expansion factor between the areas of faculae and plages. This factor is an indicator of the connection between the photosphere and the chromosphere. Using machine learning techniques, scientists are working on generating simulated Ca II K images from white-light images to obtain information about the chromospheric activity in the past. Therefore, the connection between faculae and plages need to be understood, particularly this expansion factor. It would be very interesting to analyse how this factor evolves with the type of active region (old or new), the solar cycle, etc...

Global warming has greatly impacted scientific research over the past few decades. While we constantly hear about the impact of anthropogenic activity, many studies have shown that solar activity does have an impact on the Earth's climate. Long well-known periods of solar minimum, during which the Sun's activity was very low, have historically been associated with climatic cold periods on Earth. Studying these near-zero activity episodes in more detail through chromospheric activity would help to improve climate models and possibly predict future long-duration episodes of low activity and their impact on Earth's climate.

Given the limitations of stellar observations, the manner and cadence at which observations are conducted are crucial. As we noticed with the solar-type stars observations using the TIGRE telescope, the samples are very limited compared to solar observations from USET, for example. On average, a solar-type star is observed 20 times per year with TIGRE. This has a significant impact on the detection of periodic modulations due to rotation or activity cycles. However, based on our concrete results, a possible improvement in stellar observation programs could be proposed as one of the contributions of this work. For instance, young stars are rotating faster and have a higher magnetic activity. Hence, for those stars, more intensive observing campaings are needed but over a short duration. For older stars, with a slower rotation and a lower level of activity, longer campaigns are required, but not necessarily with a very dense sampling.

List of publications

Articles in Internationally Reviewed Academic Journals

- *"Relationship between TIGRE solar S-index and USET Ca* II *K full disk images"* – Published as First Author on May 2024 in Astronomy & Astrophysics
  https://doi.org/10.1051/0004-6361/202450125
  G. Vanden Broeck, S. Bechet, F. Clette, G. Rauw, K.-P. Schröder, and M. Mittag

- *"How does the solar chromospheric activity look like under different inclination angles?"* – In the submission process as First Author in Astronomy & Astrophysics
  https://arxiv.org/abs/2410.11335
  G. Vanden Broeck, S. Bechet, G. Rauw, and F. Clette

Conferences

- "Study of the magnetic structures in full-disk solar Ca II K images and sun-like stars connection" as a poster at the Cool Stars, Stellar Systems and the Sun Conference, held in Toulouse, France, in July 2022.

- "Study of the magnetic structures in full-disk solar Ca II K images and sun-like stars connection" as a poster at the Space Climate Symposium, held in Krakow, Poland, in September 2022.

- "Comparison of the magnetic structures in full-disk solar Ca II K images and Sun-as-a-star S-Index" as a talk at the 28th General Assembly of the International Union of Geodesy and Geophysics, held in Berlin, Germany, in June 2023.

- "Effect of the inclination angle of solar rotation axis on Ca II K structures using direct solar observations" as a talk at the Triennial Earth-Sun Summit, held in Dallas, United States of America, in April 2024.

- "Effect of the inclination angle of the solar rotation axis on disk-resolved indices from full-disk solar images in the Ca II K line" as a e-poster at the 32nd International Astronomical Union General Assembly, held in Cape Town, South Africa, in August 2024 (Vanden Broeck & Bechet 2024).

Bibliography

Baglin, A., Auvergne, M., Boisnard, L., et al. 2006, in 36th COSPAR Scientific Assembly, Vol. 36, 3749

Baliunas, S. L., Donahue, R. A., Soon, W., & Henry, G. W. 1998, in Astronomical Society of the Pacific Conference Series, Vol. 154, Cool Stars, Stellar Systems, and the Sun, ed. R. A. Donahue & J. A. Bookbinder, 153

Baliunas, S. L., Donahue, R. A., Soon, W. H., et al. 1995, The Astrophysical Journal, 438, 269

Baliunas, S. L., Horne, J. H., Porter, A., et al. 1985, The Astrophysical Journal, 294, 310

Basri, G., Walkowicz, L. M., & Reiners, A. 2013, The Astrophysical Journal, 769, 37

Basu, S. & Antia, H. M. 2001, Monthly Notices of the Royal Astronomical Society, 324, 498

Bechet, S. & Clette, F. 2002, USET images L1centered, https://doi.org/10.24414/nc7j-b391, published by Royal Observatory of Belgium (ROB)

Becker, U. 1954, Zeitschrift für Astrophysik, 34, 129

Bertello, L., Pevtsov, A., Tlatov, A., & Singh, J. 2016, Solar Physics, 291, 2967

Bhattacharya, S., Teague, E. T. H., Fay, S., et al. 2021, Solar Physics, 296, 118

Bordé, P., Rouan, D., & Léger, A. 2003, Astronomy & Astrophysics, 405, 1137

Borgniet, S., Meunier, N., & Lagrange, A. M. 2015, Astronomy & Astrophysics, 581, A133

Boro Saikia, S., Marvin, C. J., Jeffers, S. V., et al. 2018, Astronomy & Astrophysics, 616, A108

Borrero, J. M. & Ichimoto, K. 2011, Living Reviews in Solar Physics, 8, 4

Borucki, W. J., Koch, D., Basri, G., et al. 2010, Science, 327, 977

Brants, J. J. & Zwaan, C. 1982, Solar Physics, 80, 251

Brune, R. & Woehl, H. 1982, Solar Physics, 75, 75

Calabretta, M. R. & Greisen, E. W. 2002, Astronomy & Astrophysics, 395, 1077

Cameron, R. H., Dikpati, M., & Brandenburg, A. 2017, Space Science Reviews, 210, 367

Cameron, R. H., Jiang, J., Schüssler, M., & Gizon, L. 2014, Journal of Geophysical Research (Space Physics), 119, 680

Chapman, G. A., Cookson, A. M., & Dobias, J. J. 1997, The Astrophysical Journal, 482, 541

Chapman, G. A., Dobias, J. J., & Arias, T. 2011, The Astrophysical Journal, 728, 150

Charbonneau, P., Christensen-Dalsgaard, J., Henning, R., et al. 1999, The Astrophysical Journal, 527, 445

Chatterjee, S., Banerjee, D., & Ravindra, B. 2016, The Astrophysical Journal, 827, 87

Chatterjee, S., Mandal, S., & Banerjee, D. 2017, The Astrophysical Journal, 841, 70

Chatzistergos, T. 2017, PhD thesis, Dissertation, Göttingen, Georg-August Universität

Chatzistergos, T., Ermolli, I., Krivova, N. A., et al. 2022, Astronomy & Astrophysics, 667, A167

Chatzistergos, T., Ermolli, I., Krivova, N. A., & Solanki, S. K. 2019, Astronomy & Astrophysics, 625, A69

Chatzistergos, T., Ermolli, I., Krivova, N. A., et al. 2020, Astronomy & Astrophysics, 639, A88

Choudhuri, A. R. 2015, Nature's third cycle: A story of sunspots (Oxford University Press)

Clette, F. 2021, Journal of Space Weather and Space Climate, 11, 2

Clette, F. 2022, Le Soleil et nous: Tout comprendre sur Notre Etoile, de son coeur en fusion jusqu'à la terre et son Climat (Favre)

Clette, F. & Lefèvre, L. 2016, Solar Physics, 291, 2629

da Silva Santos, J. M., de la Cruz Rodríguez, J., Leenaarts, J., et al. 2020, Astronomy & Astrophysics, 634, A56

Dalal, S., Haywood, R., Mortier, A., Chaplin, W., & Meunier, N. 2023, Monthly Notices of the Royal Astronomical Society, 525

De Rosa, M. L. & Toomre, J. 2004, The Astrophysical Journal, 616, 1242

Del Moro, D., Berrilli, F., Duvall, T. L., J., & Kosovichev, A. G. 2004, Solar Physics, 221, 23

Dudok de Wit, T. 2016, Earth's climate response to a changing sun: A review of the current understanding by the European Research Group tosca (EDP Sciences)

Duncan, D. K., Vaughan, A. H., Wilson, O. C., et al. 1991, The Astrophysical Journal Supplement Series, 76, 383

Eff-Darwich, A., Korzennik, S. G., & Jiménez-Reyes, S. J. 2002, The Astrophysical Journal, 573, 857

Eggleton, P. 2006, Evolutionary Processes in Binary and Multiple Stars, Cambridge Astrophysics (Cambridge University Press)

Elliott, J. R. & Gough, D. O. 1999, The Astrophysical Journal, 516, 475

Ermolli, I., Chatzistergos, T., Krivova, N. A., & Solanki, S. K. 2018, Proceedings of the International Astronomical Union, 13, 115–120

Ermolli, I., Criscuoli, S., Centrone, M., Giorgi, F., & Penza, V. 2007, Astronomy & Astrophysics, 465, 305

Ermolli, I., Fofi, M., Bernacchia, C., et al. 1998, Solar Physics, 177, 1

Ermolli, I., Solanki, S. K., Tlatov, A. G., et al. 2009, The Astrophysical Journal, 698, 1000

Fontenla, J. M., Curdt, W., Haberreiter, M., Harder, J., & Tian, H. 2009, The Astrophysical Journal, 707, 482

Foukal, P. 1996, Geophysical Research Letters, 23, 2169

Foukal, P. V. 2004, Solar Astrophysics, 2nd, Revised Edition (Wiley-VCH)

Garcia, A., Sobotka, M., Klvaňa, M., & Bumba, V. 2011, Contributions of the Astronomical Observatory Skalnate Pleso, 41, 69

Gonzalez, R. C., Woods, R. E., & Masters, B. R. 2009, Digital Image Processing, Third Edition (Prentice Hall)

Gray, L. J., Beer, J., Geller, M., et al. 2010, Reviews of Geophysics, 48

Guerrero, G., Smolarkiewicz, P. K., de Gouveia Dal Pino, E. M., Kosovichev, A. G., & Mansour, N. N. 2016, The Astrophysical Journal, 819, 104

Hagenaar, H. J., Schrijver, C. J., & Title, A. M. 1997, The Astrophysical Journal, 481, 988

Hart, A. B. 1954, Monthly Notices of the Royal Astronomical Society, 114, 17

Hasan, S. S., Mallik, D. C. V., Bagare, S. P., & Rajaguru, S. P. 2010, in Astrophysics and Space Science Proceedings, Vol. 19, Magnetic Coupling between the Interior and Atmosphere of the Sun, ed. S. S. Hasan & R. J. Rutten, 12–36

Hathaway, D. 2010, Living Reviews in Solar Physics, 7

Hathaway, D. H., Beck, J. G., Han, S., & Raymond, J. 2002, Solar Physics, 205, 25

Haugan, S. V. H. & Fredvik, T. 2020, arXiv e-prints, arXiv:2011.12139

Hempelmann, A., Mittag, M., Gonzalez-Perez, J. N., et al. 2016, Astronomy & Astrophysics, 586, A14

Hirzberger, J., Gizon, L., Solanki, S. K., & Duvall, T. L. 2008, Solar Physics, 251, 417

Hughes, D., Rosner, R., & Weiss, N. 2007, The Solar Tachocline, by Edited by D. W. Hughes, R. Rosner, N. O. Weiss, Cambridge, UK: Cambridge University Press, 2007

Jeffries, R. D., Evans, P. A., Pye, J. P., & Briggs, K. R. 2006, Monthly Notices of the Royal Astronomical Society, 367, 781

Jenkins, J. L. 2009, The Sun and how to observe it (Springer New York)

Judge, P. G. & Peter, H. 1998, Space Science Reviews, 85, 187

Kiess, C., Rezaei, R., & Schmidt, W. 2014, Astronomy & Astrophysics, 565, A52

Kitchatinov, L. L. 2014, Geomagnetism and Aeronomy, 54, 867

Knaack, R., Fligge, M., Solanki, S. K., & Unruh, Y. C. 2001, Astronomy & Astrophysics, 376, 1080

Kopp, G. & Rabin, D. 1992, Solar Physics, 141, 253

Kuhn, J. R. & Foukal, P. V. 1993, in Bulletin of the American Astronomical Society, Vol. 25, 1184

Kuriyan, P. P., Muralidharan, V., & Sampath, S. 1982, Indian Journal of Radio and Space Physics, 11, 229

Lean, J. & Rind, D. 1998, Journal of Climate, 11, 3069

Lefebvre, S., Ulrich, R. K., Webster, L. S., et al. 2005, Memorie della Società Astronomica Italiana, 76, 862

Leighton, R. B., Noyes, R. W., & Simon, G. W. 1962, The Astrophysical Journal, 135, 474

Liu, S.-Y. 1974, The Astrophysical Journal, 189, 359

Lockwood, G. W. & Skiff, B. A. 1990, in NASA Conference Publication, Vol. 3086, NASA Conference Publication, 8–15

Lockwood, G. W., Skiff, B. A., Henry, G. W., et al. 2007, The Astrophysical Journal Supplement Series, 171, 260

Lockwood, M., Harrison, R. G., Woollings, T., & Solanki, S. K. 2010, Environmental Research Letters, 5, 024001

Lourenço, A., Carvalho, S., Barata, T., et al. 2019, Open Astronomy, 28, 165

Malherbe, J.-M. 2023, Journal for the History of Astronomy, 54, 274

Malherbe, J. M. & Dalmasse, K. 2019, Solar Physics, 294, 52

Mandal, S., Chatterjee, S., & Banerjee, D. 2017, The Astrophysical Journal, 835, 158

McQuillan, A., Mazeh, T., & Aigrain, S. 2014, The Astrophysical Journal Supplement Series, 211, 24

Meibom, S., Barnes, S. A., Platais, I., et al. 2015, Nature, 517, 589

Met Office. 2010 - 2015, Cartopy: a cartographic python library with a Matplotlib interface, Exeter, Devon

Meunier, N., Lagrange, A. M., Boulet, T., & Borgniet, S. 2019, Astronomy & Astrophysics, 627, A56

Mitalas, R. & Sills, K. R. 1992, The Astrophysical Journal, 401, 759

Mittag, M., Schmitt, J. H. M. M., & Schröder, K. P. 2013, Astronomy & Astrophysics, 549, A117

Mittag, M., Schröder, K. P., Hempelmann, A., González-Pérez, J. N., & Schmitt, J. H. M. M. 2016, Astronomy & Astrophysics, 591, A89

Molnar, M. E., Reardon, K. P., Chai, Y., et al. 2019, The Astrophysical Journal, 881, 99

Morita, S., Shibata, K., UeNo, S., et al. 2010, Publications of the Astronomical Society of Japan, 62, 901

Morosin, R., de la Cruz Rodríguez, J., Díaz Baso, C. J., & Leenaarts, J. 2022, Astronomy & Astrophysics, 664, A8

Nèmec, N. E., Shapiro, A. I., Krivova, N. A., et al. 2020, Astronomy & Astrophysics, 636, A43

Nesme-Ribes, E., Meunier, N., & Collin, B. 1996, Astronomy & Astrophysics, 308, 213

Ni, L., Lukin, V. S., Murphy, N. A., & Lin, J. 2018, Physics of Plasmas, 25, 042903

Noraz, Q., Brun, A. S., Strugarek, A., & Depambour, G. 2022, Astronomy & Astrophysics, 658, A144

Noyes, R. W., Hartmann, L. W., Baliunas, S. L., Duncan, D. K., & Vaughan, A. H. 1984a, The Astrophysical Journal, 279, 763

Noyes, R. W., Weiss, N. O., & Vaughan, A. H. 1984b, The Astrophysical Journal, 287, 769

Osterbrock, D. E. 1961, The Astrophysical Journal, 134, 347

Owens, M. J., Lockwood, M., Hawkins, E., et al. 2017, Journal of Space Weather and Space Climate, 7, A33

Pallavicini, R., Golub, L., Rosner, R., et al. 1981, The Astrophysical Journal, 248, 279

Priest, E. 2023, Advances in Space Research, 71, 1856, recent progress in the physics of the Sun and heliosphere

Priyal, M., Singh, J., Belur, R., & Rathina, S. K. 2017, Solar Physics, 292, 85

Priyal, M., Singh, J., Ravindra, B., Priya, T. G., & Amareswari, K. 2014, Solar Physics, 289, 137

Priyal, M., Singh, J., Ravindra, B., & Shekar B, C. 2019, Solar Physics, 294, 131

Radick, R. R., Lockwood, G. W., Henry, G. W., Hall, J. C., & Pevtsov, A. A. 2018, The Astrophysical Journal, 855, 75

Radick, R. R., Lockwood, G. W., Skiff, B. A., & Baliunas, S. L. 1998, The Astrophysical Journal Supplement Series, 118, 239

Rast, M. P. 2003, The Astrophysical Journal, 597, 1200

Reinhold, T., Shapiro, A. I., Solanki, S. K., et al. 2020, Science, 368, 518

Rezaei, R., Beck, C., & Schmidt, W. 2012, Astronomy & Astrophysics, 541, A60

Ricker, G. R., Winn, J. N., Vanderspek, R., et al. 2014, in Society of Photo-Optical Instrumentation Engineers (SPIE) Conference Series, Vol. 9143, Space Telescopes and Instrumentation 2014: Optical, Infrared, and Millimeter Wave, ed. J. Oschmann, Jacobus M., M. Clampin, G. G. Fazio, & H. A. MacEwen

Rieutord, M., Roudier, T., Rincon, F., et al. 2010, Astronomy & Astrophysics, 512, A4

Robrade, J., Schmitt, J. H. M. M., & Favata, F. 2012, Astronomy & Astrophysics, 543, A84

Rüdiger, G. 1989, Differential Rotation and Stellar Convection: Sun and Solar-type Stars, Fluid mechanics of astrophysics and geophysics (Gordon and Breach Science Publishers)

Rüdiger, G. & Hollerbach, R. 2004, The Magnetic Universe: Geophysical and Astrophysical Dynamo Theory (Wiley)

Sánchez-Bajo, F., Vaquero, J. M., & Rubio Montero, M. P. 2002, European Journal of Physics, 23, 323

Schatten, K. H. 1993, Journal of Geophysical Research, 98, 18907

Schmitt, J. H. M. M., Schröder, K. P., Rauw, G., et al. 2014, Astronomische Nachrichten, 335, 787

Schmutz, W. K. 2021, Journal of Space Weather and Space Climate, 11, 40

Schrijver, C. J. & Zwaan, C. 2000, Solar and Stellar Magnetic Activity, Cambridge Astrophysics (Cambridge University Press)

Schröder, K. P., Mittag, M., Hempelmann, A., González-Pérez, J. N., & Schmitt, J. H. M. M. 2013, Astronomy & Astrophysics, 554, A50

Schröder, K. P., Mittag, M., Pérez Martínez, M. I., Cuntz, M., & Schmitt, J. H. M. M. 2012, Astronomy & Astrophysics, 540, A130

Schröder, K. P. & Schmitt, J. H. M. M. 2013, in Astronomical Society of the Pacific Conference Series, Vol. 472, New Quests in Stellar Astrophysics III: A Panchromatic View of Solar-Like Stars, With and Without Planets, ed. M. Chavez, E. Bertone, O. Vega, & V. De la Luz, 225

Shapiro, A. I., Solanki, S. K., Krivova, N. A., et al. 2014, Astronomy & Astrophysics, 569, A38

Simon, G. W. & Leighton, R. B. 1964, The Astrophysical Journal, 140, 1120

Singh, J., Belur, R., Raju, S., et al. 2012, Research in Astronomy and Astrophysics, 12, 201

Singh, J., Priyal, M., & Ravindra, B. 2021, The Astrophysical Journal, 908, 210

Singh, J., Priyal, M., Ravindra, B., Bertello, L., & Pevtsov, A. 2023, Research in Astronomy and Astrophysics, 23, 045016

Skumanich, A. 1972, The Astrophysical Journal, 171, 565

Skumanich, A., Lean, J. L., Livingston, W. C., & White, O. R. 1984, The Astrophysical Journal, 282, 776

Skumanich, A., Smythe, C., & Frazier, E. N. 1975, The Astrophysical Journal, 200, 747

Solanki, S. K. 2003, The Astronomy and Astrophysics Review, 11, 153

Solanki, S. K., Krivova, N. A., & Haigh, J. D. 2013, Annual Rev. Astron. Astrophys, 51, 311

Soler, R., Terradas, J., Oliver, R., & Ballester, J. L. 2019, The Astrophysical Journal, 871, 3

Sowmya, K., Nèmec, N. E., Shapiro, A. I., et al. 2021a, The Astrophysical Journal, 919, 94

Sowmya, K., Shapiro, A. I., Rouppe van der Voort, L. H. M., Krivova, N. A., & Solanki, S. K. 2023, The Astrophysical Journal Letters, 956, L10

Sowmya, K., Shapiro, A. I., Witzke, V., et al. 2021b, The Astrophysical Journal, 914, 21

Steinegger, M., Brandt, P. N., & Haupt, H. F. 1996, Astronomy & Astrophysics, 310, 635

Stimets, R. W. & Giles, R. H. 1980, The Astrophysical Journal Letters, 242, L37

Stix, M. 2004, The Sun: An Introduction (Springer)

Strugarek, A., Belucz, B., Brun, A. S., Dikpati, M., & Guerrero, G. 2023, Space Science Reviews, 219, 87

Tapping, K. F. & Morton, D. C. 2013, in Journal of Physics Conference Series, Vol. 440, Journal of Physics Conference Series (IOP), 012039

Tlatov, A. G., Pevtsov, A. A., & Singh, J. 2009, Solar Physics, 255, 239

Tlatova, K. A., Vasil'eva, V. V., & Tlatov, A. G. 2019, Astronomical and Astrophysical Transactions, 31, 109

Vanden Broeck, G. & Bechet, S. 2024, in IAU General Assembly, 927

Vanden Broeck, G., Bechet, S., Clette, F., et al. 2024a, Astronomy & Astrophysics, 689, A95

Vanden Broeck, G., Bechet, S., Rauw, G., & Clette, F. 2024b, arXiv e-prints, arXiv:2410.11335

Vaughan, A. H., Baliunas, S. L., Middelkoop, F., et al. 1981, The Astrophysical Journal, 250, 276

Vaughan, A. H. & Preston, G. W. 1980, Publications of the Astronomical Society of the Pacific, 92, 385

Vaughan, A. H., Preston, G. W., & Wilson, O. C. 1978, Publications of the Astronomical Society of the Pacific, 90, 267

Vernazza, J. E., Avrett, E. H., & Loeser, R. 1981, The Astrophysical Journal Supplement Series, 45, 635

Waldmeier, M. 1955, Ergebnisse und Probleme der Sonnenforschung. (Lpz Akademische Verlagsgesellschaft Becker & Erler)

Wilson, O. C. 1968, The Astrophysical Journal, 153, 221

Worden, J. R., White, O. R., & Woods, T. N. 1998, The Astrophysical Journal, 496, 998

Wright, J. T., Marcy, G. W., Butler, R. P., & Vogt, S. S. 2004, The Astrophysical Journal Supplement Series, 152, 261

Zwaan, C. 1978, Solar Physics, 60, 213